Tactile Measurement with a GelSight Sensor

by

Wenzhen Yuan

Submitted to the Department of Mechanical Engineering
in partial fulfillment of the requirements for the degree of

Master of Science in Mechanical Engineering

at the

MASSACHUSETTS INSTITUTE OF TECHNOLOGY

September 2014

Signature redacted

Author ....
Department of Mechanical Engineering
August 12, 2014

Signature redacted

Certified by ....
Edward H. Adelson
John and Dorothy Wilson Professor
Thesis Supervisor

Signature redacted

Certified by ....
Mandayam A. Srinivasan
Senior Research Scientist
Thesis Supervisor

Signature redacted

Accepted by ....
David E. Hardt
Chairman, Department Committee on Graduate Theses

Tactile Measurement with a GelSight Sensor

by

Wenzhen Yuan

Submitted to the Department of Mechanical Engineering
on August 12, 2014, in partial fulfillment of the
requirements for the degree of
Master of Science in Mechanical Engineering

Abstract

This thesis introduces a method of measuring contact force with GelSight. GelSight is an optical-based tactile sensor that uses a piece of coated elastomer as the contact medium. A camera records the distortion of the elastomer during contact. This sensor can obtain a high-resolution view of the contact surface geometry, which is a breakthrough for artificial tactile sensors. In this thesis, I will introduce my work on trying to measure the contact force with GelSight. This work is based on adding markers to the elastomer surface and using them to track the planar deformation field of the elastomer surface. I derive a quantitative relationship between the surface's planar deformation field and the external contact force. I describe the development of a finite element model of the elastomer as well as the experiments on a bench-top and a portable GelSight devices. The experiments show that the contact force and the deformation field are closely related, and indicate that the method is effective in inferring the contact state under realistic conditions.

Thesis Supervisor: Edward H. Adelson
Title: John and Dorothy Wilson Professor

Thesis Supervisor: Mandayam A. Srinivasan
Title: Senior Research Scientist

Contents

List of Figures

Chapter 1

Introduction

1.1 Motivation

As the most dexterous part of the human body, the hand is mainly occupied by three kinds of jobs: exploring the surroundings, restraining objects, and manipulating objects[7]. In each job, the interaction between the human hand and the external environment plays a vital role, and the tactile sensing system is especially essential for obtaining the information about the surrounding environment and guiding hand movements.

It is amazing how powerful the human tactile system is, and how much it can perceive. Figure 1-1 shows some examples of the use of the human tactile system: even without the help of vision, our tactile system can learn about the materials and geometry of the objects, can grasp an object safely and estimate its weight, and can perform simple manipulations such as flipping a switch or controlling the position of an object in the hand.

Artificial tactile sensors are used by robots to assist their manipulation of objects. Figure 1-2 shows some example capabilities of a robot hand with pressure sensor arrays mounted on its fingertips: it can grasp a delicate object with proper force, or do a fine in-hand manipulation like rotating a straw, or interact with a human. With the help of tactile sensors, a robot hand can do a better job in grasping and in-hand manipulation: with the feedback of the squeezing force when grasping delicate

(a) Feeling the material of the cloth.

(b) Feeling the shape of the object.

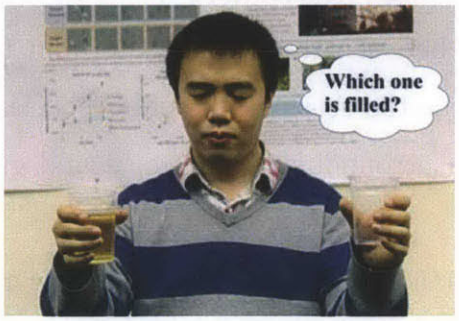

(c) Holding cups, and estimating the weight of them.

(d) Manipulating a switch.

Figure 1-1: Examples of the human tactile system perceiving the surroundings and assisting manipulation.

(a) Assist grasping

(b) Assist in-hand manipulation

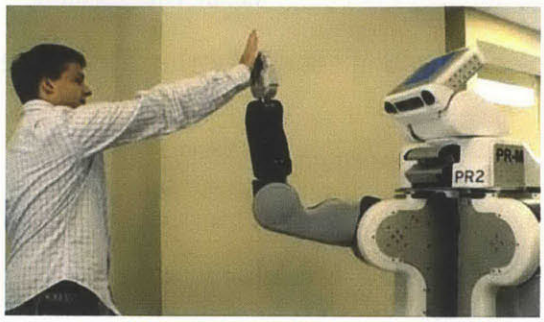

(c) Interacting with human

Figure 1-2: Examples of a tactile system used by a robot.[2]

objects, the hand is able to control the grasp force, so that it is neither so large as to harm the object nor too small as to fail to grasp the object. In the example shown in Figure 1-2(b), the tactile sensors tell how the straw is contacting with the robot hand, and this helps the robot better manipulate the stick.

However, compared to the human tactile system, that of robots is considerately less capable. Regardless of the sensing area, artificial tactile systems are single-functional and much less flexible, and artificial tactile systems can hardly do any exploration. A major reason is the low spatial resolution and confined functions of artificial tactile sensors. Most tactile sensors perceives only contact force or pressure. The human tactile system, however, can detect more varied types of stimulation, like forces and torques on different axes, pressure distributions, vibrations, and so on. The high spatial resolution of the pressure distribution detection for the human tactile system can tell not only the contact area and the forces, but also the local geometry of the contact surface. In other words, human can feel the textures on an object's surface, which helps to recognize the material. Additionally, the human tactile system is able

(a) View of the surface of human skin. (b) View of the texture of a fabric. (c) View of the small printed letters on a 20-dollar bill.

Figure 1-3: Examples of GelSight views of the contact surface texture.[17]

to feel the tangential force and slippage condition of the contact surface, which is hard for nearly all artificial tactile sensors. Nevertheless, that information is essential in assisting grasp and estimating the friction condition of a material's surface.

As an attempt to improve the situation, a new kind of tactile sensor called GelSight was proposed in [18]. GelSight is an optical tactile sensor, which uses a piece of elastomer as the sensing medium and a camera to capture the deformation of the elastomer when contacting a surface. Then it uses photometric stereo to reconstruct the 3D structure of the surface out of the image of the distorted elastomer. Different from most existing tactile sensors, which sense contact force, GelSight senses surface geometry. The sensor is able to detect the fine textures of the contact surface, and is of even higher spatial resolution than the human tactile system. Figure 1-3 shows some examples of GelSight's view of some surface textures. So in this sense, GelSight is a breakthrough for artificial tactile sensors in that it achieved a high resolution view of the touching surface's fine structure, thus making it possible for an artificial tactile sensor to do some environment exploration work and material recognition. Additionally, the softness and deformability of the sensor make it compatible for most robotic tasks.

Nevertheless, a problem of the GelSight sensor is that it does not detect the force distribution, while the human tactile system can measure both the surface geometry and the contact force distribution. By combining the two, the tactile sensor would be able to get far more information about the contact surface. One typical example is shear force and slip detection. This is very important for making a good grasp for both

human and robots. The most common grasp failure for robot grasp is that the object would slip from the hand because the gripping force is not large enough. A tactile sensor that can feel whether the object is slipping from the hand, or whether slippage is going to happen, are in high demand, so that it can decide whether a larger normal force is required to ensure the grasp. Unfortunately, hardly any artificial tactile sensors can detect slip, and very few of them can measure shear force. GelSight augmented with force measurement would be able to detect the slip, and estimate the likeliness of a potential slip by measuring the shear force and combining it with the contact surface movement.

Another potential improvement of GelSight with force measurement lies in material recognition. For humans, it is natural and efficient to recognize a material's properties simply by touch; we are able to feel the material's roughness and surface textures, and other mechanical properties such as softness, friction and heat conductivity which are all important properties to distinguish a material. With the help of GelSight's ability to view the contact surface's geometry, a machine or a robot can learn the texture and roughness of the material, but it would be able to measure the softness and friction only when it is able to detect the contact force. Thus if GelSight were able to measure the contact force, its ability for recognizing materials and estimating material properties would be largely expended.

Other potential benefits of a GelSight sensor to measure contact force include detecting indirect contact situations, for example, when using a tool. If GelSight was able to measure contact force, when holding a tool with a GelSight sensor, we would be able to know from the contact force distribution whether the tool is in contact with some rigid surface, and even the contact force and direction. This would be helpful when using a screwdriver to fasten a screw, or spooning food, or inserting a cable into a socket.

In conclusion, it would be very useful to enable GelSight to measure contact forces. In this project, I proposed a method to infer the force on the contact surface from the deformation of the elastomer medium. As an elastic material, the elastomer deforms predictably according to the contact force and the boundary conditions.

The previous work on GelSight mainly records the elastomer's distortion in the axial direction, which can be used to infer the contact surface's geometry. In this project, I add markers to the elastomer's surface and track the displacement of the markers, which indicates the planar deformation of the elastomer surface. Then I use that deformation information to infer the three-axis contact force.

In this thesis, I firstly look into the theoretical model of the elastomer when it contacts a rigid surface, then conduct indenting experiments and analyze the modes of the displacement field. In the experiments, different contact forces with different indenters are applied, and on two different GelSight designs: a large GelSight prototype and a small portable GelSight device which can be used on a robot finger or held by human hands. Then some examples of the dynamic displacement field during grasping and manipulation tasks are shown. The data in this thesis introduce a possible way to measure contact force with a GelSight sensor, and the study of the elastomer deformation under different contact condition is also illuminative for haptic study on the contact of an elastic body to a rigid surface.

1.2 Robotic tactile system

1.2.1 An Overview of Human and Robotic Tactile Systems

The human tactile system consists of multiple tissues. Just for the epidermis mechanoreceptors which respond to the mechanical stimulus on the skin, there are four kinds of cells: Pacinian Corpuscle, Ruffini Corpuscle, Merkel Cells, and Meissner's Corpuscle[8]. The cells are aligned at different depths in the skin, and are sensitive to different kinds of mechanical stimuli:

1. Pacinian Corpuscle: sensitive to high-frequency vibration with low spatial resolution

2. Ruffini Corpuscal: sensitive to static forces in different directions with low spatial resolution

3. Merkel Cells: sensitive to very low frequency forces and skin deformation with high spatial resolution

4. Meissner's Corpuscle: sensitive to low-frequency vibration with high spatial resolution

In varied tactile tasks, different mechanoreceptors perform as the major sensing receptor. But in general, the four different kinds of sensing results combine together to give an overall view of the mechanical environment of the contact surface. The sensing system is also intertwined with the kinesthetic system, where the motion and force of body parts are measured through some internal receptors. Other perceptions are included as well, like cutaneous sensing, temperature sensing, and pain sensing. As a whole, the *tactile sensing system* of humans is a system with a wide array of receptors, and what human feels as touch is a synthesis of different sensing information.

Additionally, the brain is an important part of the tactile system as it makes sense of the raw data coming in from the tactile sensors. Thus although the absolute precision of human receptors is inferior to many artificial electronic sensors, the sensing system works well in guiding human behavior in various environments, and interpreting the interactive environment in a special way for human understanding.

For robotic sensing systems, similar theories have been proposed. An example is the model brought up by Howe[11], as shown in Figure 1-4: in this model, the robotic sensing system consists of different electronic sensors, including the tactile array sensor on the fingertips to feel the pressure distribution on the contact surface, the dynamic tactile sensor on the fingertips to feel the vibration of the contact surface, the fingertip force-torque sensors to measure the static forces and torques of the finger's interaction, and the joint angle sensors to measure the exact angles of each joint to calculate the precise position, velocities, and accelerations of the body parts.

However, the theories have not been realized. The major research in artificial tactile sensors has been focusing on sensors or sensor arrays to measure local forces or pressures on a fingertip. Force-torque sensors and motion sensors have been developed, but they are mostly applied only for motion control, and are seldom involved

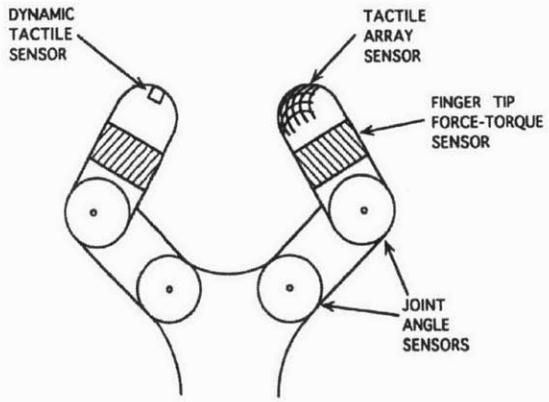

Figure 1-4: A schematic of robot gripper equipped with different types of sensors. [11]

in tactile sensing. Vibration sensors have also been far less popular.

Moreover, a giant problem of robotic tactile sensing systems is their incompetence in intelligently interpreting the information given by the sensors. In many cases, the existing sensors transfers enormous data, but the algorithms to extract useful information from this data are lacking. Software for integrating information from multiple sensors is also quite primitive. Developing perception models that can meaningfully interpret raw sensor data is a major current challenge in the development of artificial tactile systems.

1.2.2 Examples of Artificial Tactile Sensors

Artificial tactile sensors for robotic hands and other uses have been widely developed. Dhiya[8] and Yousef[32] give a thorough review of the recent tactile sensors. According to Dhiya[8], artificial tactile sensors can be categorized in the following major categories according to their transduction principle: resistive sensors, tunnel effect tactile sensors, capacitive sensors, optical sensors, ultrasonics-based sensors, magnetism-based sensors and piezoelectric sensors. Most of these sensors use material properties that change according to the external force or pressure, like resistance or capacity, to measure the contact normal force. Others use a physical medium which may deform according to the external force, and indirectly infer the contact

force from the deformation. The majority of the optical sensors work in this way.

For an artificial tactile sensor, higher resolution, more thorough measurements, smaller size and less power consumption, and a compliant surface are desired. The compliance of a sensor refers to its ability to conform to highly curved or irregular surfaces. A highly compliant sensor is useful for tactile tasks such as grasping, where greater contact with the surface gives a more stable grasp. So, on one hand, people have been exploring better electronics or better materials for tactile sensing; on the other hand, there have been many trials on embedding the sensors on some specially designed base to reinforce these abilities. Hwang, et al. [13] embedded a group of tilted micro cantilevers in a piece of elastomer material so that the cell was able to measure both the normal stress and shear stress. Wong, et al. [24] introduced a normal force sensor array based on conductive fluid, which uses liquid metal-filled microfluidic channels as the capacitive plates and conductive interconnects. The design has a spatial resolution of 0.5mm for the 5 onboard cells and is thin and compliant for a curved surface.

Optical tactile sensors have been popular in the past ten years, with the development of small cameras and image processing algorithms. Most optical based tactile sensors use a piece of elastic material, or other deformable structure, as the media of contact, and apply a camera to track the deformation of the media. An early work on optical tactile sensor is introduced by Schneither, et al. in [28], where a reflective elastomer was taken as the medium and optic fibers were applied for light emission and reception. The reflective light was measured by a CCD camera to infer the present thickness of the elastomer at each sampling point. A similar sensor which also uses light emitting and receiving cells through an elastomer is introduced in [26] and [25]. But this sensor uses LEDs as the electronic component to emit and receive light, thus greatly reducing the size of the sensor.

Some other optical sensors make some patterns on the elastomer, and track the pattern using a camera to infer the deformation of the elastomer. [23] and [27] introduced a tactile sensor called GelForce, in which a piece of transparent elastomer is taken as the media and two layers of color markers were embedded into the elas-

tomer. A camera takes photos of the markers, and by tracking the displacement of the markers the loading force on the elastomer is inferred. The sensor is compliant and sensitive, but the resolution and precision is not high, and different contact surface conditions for the elastomer were not considered. Similarly, Ito, et al. [14] introduced an optical tactile sensor that uses a camera and a marked elastomer medium in the shape of a hemisphere. In their work, normal force, shear force, slippage and the indicative friction of the contact surfaces were studied, but the contact condition is strictly restrained.

In general, optical tactile sensors have many advantages, such as high sensitivity, larger sensing area, and compliant surfaces. But the precisions of most of the optical sensors are not good enough, and the solid modeling for the elastomer media is usually neglected, which is much more complex than most people expected. Further, commercialization of optical tactile sensors, and indeed most tactile sensors, is still faraway.

One good example of a commercialized tactile sensor is the tactile pressure sensor array from Pressure Profile Systems Inc. [4], which is applied on commercial robots fingers such as PRII and the Barrett hand. This sensor is also applied on data gloves to measure the pressure of a human hand when doing different tasks. The spatial resolution of the sensor is around 6mm$\times$6mm, and on a robot finger there are about 20 elements. The sensor array has high dynamic range and good stability, but the information measured is restricted to local pressure, and the sensor surface is rigid.

Another commercial tactile sensor is the BioTac from SynTouchs Technology[3]. BioTac is a muti-dimensional sensor shaped as a robot fingertip, and it can sense distributed contact force[30], global vibration[10], and temperature[21]. The compliant surface and the combination of multiple sensing modalities make the sensor promising for exploring humanoid tactile behavior with an artificial sensor. However, the spatial resolution of the sensor is not high enough to detect the details of the contact structure.

Chapter 2

GelSight Sensor

2.1 Introduction of GelSight Sensor

As a tactile sensor, GelSight has the most distinct characteristic of being able to capture the fine geometry of the contact surface, and reconstruct it in 3D. The working principle of GelSight is much variant from the traditional tactile sensors, in that it makes the tactile sensing based on seeing the touching surface's geometry structure instead of feeling the touching force, which is the goal of most traditional tactile sensors. Computer vision methods, which are most competent at processing high resolution data, are introduced in analyzing the touching information for GelSight.

The touch medium of GelSight is a piece of transparent elastomer which is coated with a reflective layer on one side, and fixed on a transparent hard surface on the other side. When the elastomer contacts a surface with the coated side, it distorts according to the surface geometry. The deformation of the reflective layer is indicated by the light reflection change. The camera on the fixed side takes pictures of the layer, and its distortion is indicated, and the 3D structure is reconstructed. Figure 2-1 shows how the elastomer sensor indicates the surface of a cookie when it is pressed against it.

Figure 2-2 shows the schemetic of a GelSight sensor. The lighting condition is strictly controlled, so there is less uncertainty when referring the shading information to the surface normal. The outer lights are excluded by the sensor's shell, and the

Figure 2-1: An example of the coated elastomer displaying the surface pattern of a cookie, and the reconstructed cookie surface.[18]

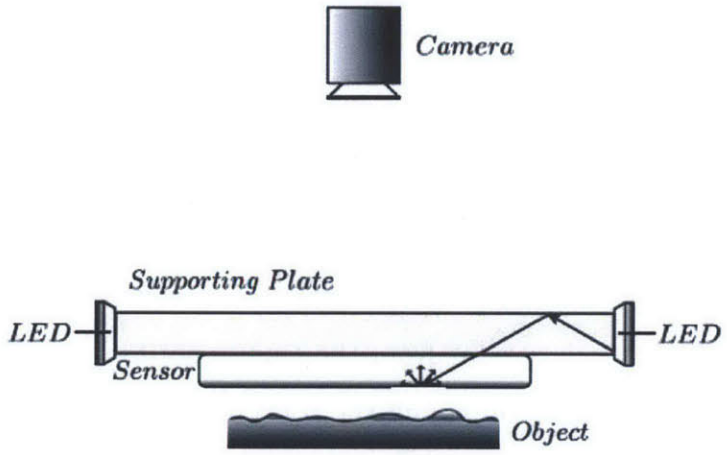

Figure 2-2: A schematic of GelSight sensor[15]

lighting on the elastomer is provided only by the fixed LEDs in the sensor. Since reflections with lights from different directions are needed in order to detect the surface normal in $\mathbb{R}^3$ space, multiple LEDs are required. There are two ways to get the differentiated illumination directions: switching the LEDs in turn and taking separate pictures on the same scene; Using multi-color LEDs for lighting and take a single picture of the hybrid lightened surface, and by taking the different channels of the color image, the reflection of different color LEDs is known. The light position and direction has an influence on the sensor's sensitivity to different kinds of touching situation.

Figure 2-3 shows different GelSight settings for different usages.

The photometry stereo algorithm[31] to reconstruct the contact surface from the

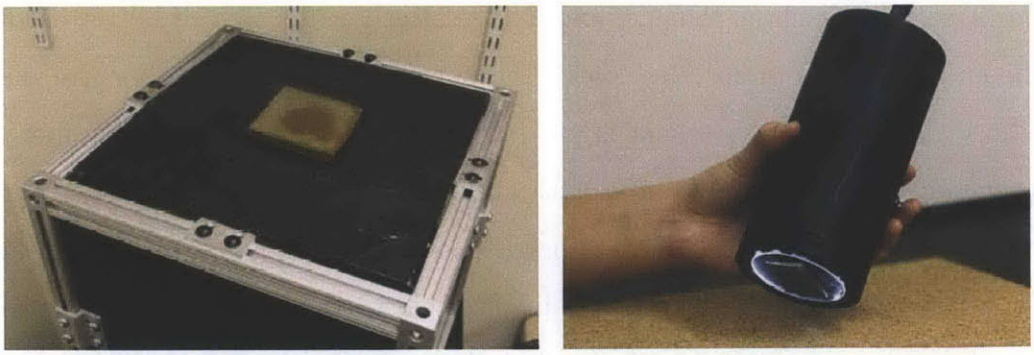

(a) Box setting of GelSight (b) Can setting of GelSight

Figure 2-3: Different designs of gel sight devices.[16]

pictures of the reflective elastomer surface layer is explained in [17]. The principal idea is to build a special look-up table for the particular illumination and reflection condition of a sensor during a calibration procedure, and construct the surface normal of each pixel during detection according to the table. By intergrating the surface normal, the 3D structure of the surface can be reconstructed.

2.2 Making the Elastomer

The elastomer's properties greatly affect the sensitive range of a sensor. An elastomer sensor is composed of two parts: the transparent elastomer base and the pigment coating layer. The elastomer base is desired to be of good good elasticity and weak viscosity, and the coatings desired to be thin, uniform and flexible with little dusts.

The important properties of an elastomer base include hardness and thickness. A sensor with soft elastomer base is easier to deform, thus is more sensitive during contacts. A hard sensor is more tolerant of heavy loads. Thicker sensor has larger absolute deformation so is easier to detect, but the thickness is restrained by the device size and illumination capability. For the newly designed portable GelSight sensor, the size of the whole device is very small, and the thickness of the elastomer sensor is generally 1mm to 2mm.

The common materials for the elastomer base are Thermoplastic Elastomer (TPE) and silicone. TPE is a kind of polymer that melts in high temperature or dissolves

in organic solvents such as toluene, and it is relatively softer and of better elasticity, but the endurance is inferior. Its coating layer get scratched easily. For the shaping procedure, the solid TPE gradient is put in the mold and melt in high temperature. The procedure takes about one hour with an oven. A major problem for the shaping is that the air bubble in the liquid is hard to eliminate, and they are vital flaws of the elastomer. Pouring the solved TPE in the mold is an alternative way, but in this case much longer curing time is required, and the thickness of the base is harder to control. So due to these limitation, TPE is not often adopted for making GelSight sensors.

The silicone is usually stored in two separate liquid parts. During molding, part A and part B are mixed together and poured into the molds, after the molds are painted with a layer of mold release agent. Disposable culture vessels made of Polystyrene prove great molds for making plate elastomer bases, but they can not be used for TPE molds because they are not heat-resistant and solvable in organic solvents. The liquid mixture is put into a vacuum pump to evacuate air bubbles. About six or seven hours later the silicone will cure and solidified.

The two silicons used in the projects are Solaris® from Smooth-on Company and XP-565 from Silicones Inc. Solaris® has a part A and part B mixing ratio of 1:1. To adjust the softness, some liquid additive is added to the materials before mixing. The additive used is Slacker® from Smooth-on Company, and it increases the softness of the silicone by volume(although the effect is not very distinct), but over-volume of Slacker® would decrease the silicone's elasticity and make it prone to fracture. A moderate proportion of slacker is 1:1:1 with part A and part B of the original silicone.

The XP-565 silicone is also stored in two liquid parts, but the typical mixing ratio is around 1:10 by weight. The mixing ratio may influence the softness of the silicone after curing, and the larger ratio the Part B is of, the softer the silicone is. In practice a desirable ratio is about 1:22 by weight in order to get a soft and endurable silicone. But as the ratio of Part B increases, the curing time also increases, and at the ratio of 1:22 it takes more than two days for the silicone to cure.

For the sensor's reflective layer, the reflective capability is the most important. However, the layer is required to be thin and opaque, and the pigment to be of small particle size. Opacity helps to exclude the external interfering lights, and thinness and the small particle size ensure the high resolution of the sensor. The commonly used pigments are metal-flack (generally bronze flake), silver or aluminum powder, and printing ink pigments.

The bronze flake is highly specular reflective, so the metal-flake layer is very sensitive to tiny deformation of the layer. Its drawbacks are the mass noises introduced by the sensitivity, and as the luminance band for surface normal changes is very narrow, the sensor is not accurate on measuring the surface normals. So this kind of sensor is more compatible for microscopic texture detection or pattern recognition, but not general shape detection. To the contrary, silver or aluminum powder layers are diffused reflective, so it is more accurate on measuring low-frequent surface information but not sensitive to high-frequent signals. The printing ink pigments have a medium reflection capability, and is of finer particles, so they are more commonly used for general-purpose sensors due to their desirable sensing range and low interference.

The printing ink pigments are made from a kind of printing ink, usually of golden or silver color. To exclude the glue ingredient in the ink, the ink is solved in D-limonene and rest for a few hours, until the pigment particles are deposited. The deposit is mixed with D-limonene again to separate the solvable glue further. The muddy sediment left is the desired pigment.

The coat layer is actually an elastomer layer dissolved with some pigment particles. For TPE elastomer, the crude material for coating is the same kind of TPE solved in organic solvents, such as toluene; for silicones, there are some special coating agent, such as Cirius® from ArtMolds Company. Cirius® is a kind of liquid silicone solved in Xylene. During using, the agent should be diluted by some other solvents such as toluene or D-limonene. In practice, metal-flake coating uses toluene as solvent as it evaporates quicker, and printing ink pigment uses D-limonene to ensure the color is lighter. Same ratio of methyl ethyl ketone(MEK) is also added to make the layer thinner and quicker to evaporate. When the silicone base is soft, some silicone

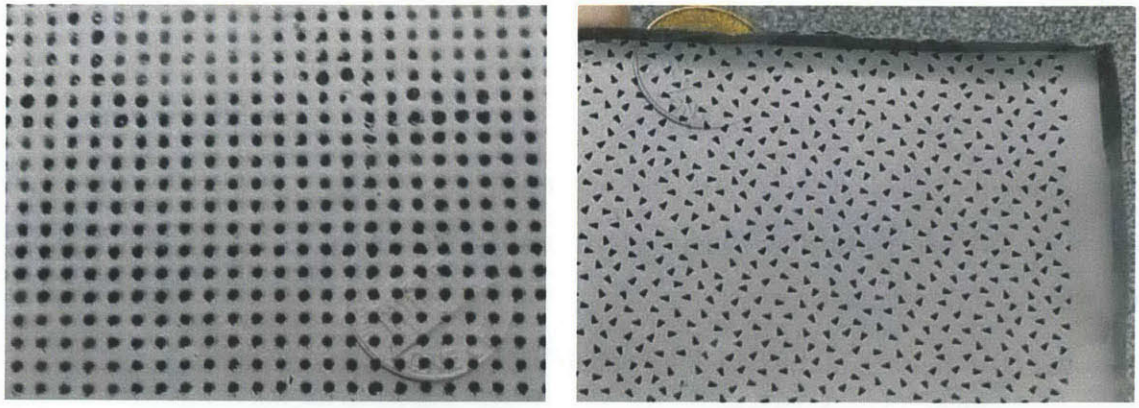

(a) (b)

Figure 2-4: Silicone pieces with different painted patterns

thinner (e.g., Slacker®) is added to the coating layer solution to make the layer softer. Otherwise, as the Cirius® silicone is hard, and there would be some wrinkles around the layer's deformed part.

There are multiple ways to make the coating layer, such as spraying the elastomer solution on the base, making the coat layer first and stick it to the base, brush the dry metal-flake directly on the elastomer base, pour the solution on the mold and then the unsolidified silicone base. It turned out that spaying is the best method, in that the pigment is very uniform. The common problem during spraying is the silicone particles may be oversize and some large impurity may be introduced. To reduce those, one should be very careful during spraying, and wait a period time after spraying one round, to enable the organic solvent to evaporate.

Other coating methods have multiple defects. For example, brushing the metal flakes directly on the silicone base is an efficient way to make the coating, but the flakes are easy to fall. One may spray a translucent coating layer after brush the flakes and the problem is solved, but in this case the flakes are so dense, and there would be some wrinkles when the layer deforms, and the surface quality is not very good. For the methods of pouring the coating layer, the problem is that as the pigment is not resolved in the mixture but dispersed as particles, when pouring the liquid the pigment is not evenly distributed and there are often some random patterns on the layer.

In this project, the specially designed elastomers have some black patterns on the coating layer, so that GelSight can measure the stretching of the elastomer surface in x-y plane by calculating the movement of the patterns. Some examples of the patterned gel sensor are shown in Figure 2-4. In the pictures, a one cent coin is press against the sensor for size comparison, and it shows that the un-patterned area of the sensor can still display the contact surface fluctuation of the object. The pattern should be of small but sparsely distributed markers, and lay between the elastomer base and the pigment layer.

The first method to make the markers is to paint them directly. As the silicone and coating against is oil soluble but not water soluble, the paint should also be oil soluble. Krylon® primer in black is chosen, and a stencil with a specific pattern of holes is placed on the elastomer base. When the paint is sprayed through this mask, the pattern is printed on the elastomer. Figure 2-4(a) shows an elastomer sensor made in this way that uses a circuit board as a stencil. A limitation of this method is that stencils of certain patterns are not easily made. Another method is using transfer paper. In this method, the patterns are drawn on a computer and printed on a special paper, which then transfers the pattern to the elastomer. Figure 2-4(b) shows a sensor made in this way. The advantage of this method is that it is much more convenient to design complicated patterns. The printing error rate is low, and the pattern quality is much better.

Chapter 3

Contact Forces Measurement with GelSight

3.1 Introduction

The sensing medium for GelSight sensor is a piece of elastomer, which will deform under external loads. The project calculated the contact forces according to the known deformation of the elastomer sensor. As one side of the elastomer sensor is fixed, the deformation of the whole elastomer is mostly indicated by the deformation of the coating layer. In the previous work, algorithms to calculate the perpendicular movement of the surface layer are developed and the 3D geometry of the contact surface is modeled, but the quantitive result is not accurate to the absolute domain; in this project, some patterns are painted on the coating layer, so that the deformation on the layer plane can be traced with good precision.

3.1.1 Elastomer Sensors to Detect Contact Forces

There have been several tactile sensors focusing on detecting contact forces, and take the deformation of the medium elastic body as the principal clues to detect the forces. Various mechanical models are used in those sensors. As the force-deformation relation of an elastic body is very complicated, in most cases, the mechanical model

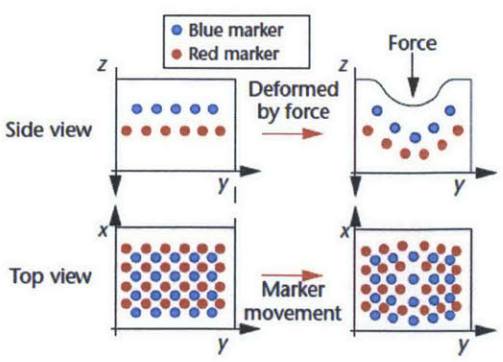

(a) Working principle of GelForce[19]

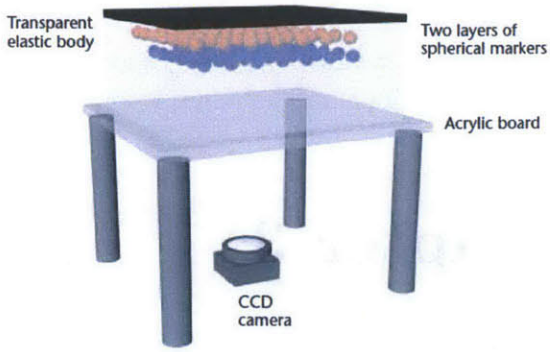

(b) Configuration diagram of plate design GelForce[19]

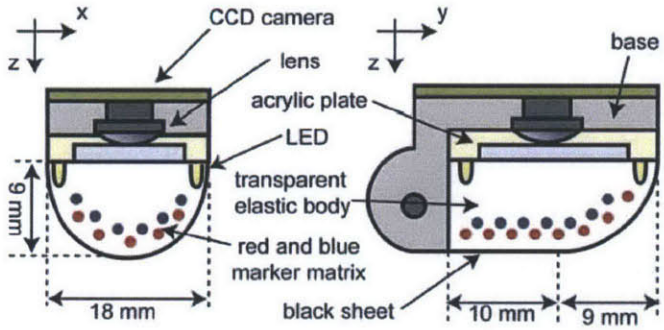

(c) Design of curved GelForce that used on robot fingers[27]

Figure 3-1: The GelForce sensor.

is specially designed for the particular model.

The GelForce sensor[19] is an example. It takes a clear elastomer with embedded makers as the force detection medium, and also uses a camera to track the markers' positions. There are two layers of regularly placed markers placed inside the elastomer, and colored blue and red respectively. The camera can catch the position of each marker in x-y plane, and the depth of the markers are recognized by color. Figure 3-1(a) shows how the markers are placed and how they move when an indentation force is applied; Figure 3-1(b) shows the structure of a plate GelForce setting.

For the mechanical modeling part, the GelForce group supposed that the elastomer reacting deformation is a linear mapping to the external forces, and they used the half-space linear elastic body with point load model. This coarse approximation introduced large deviation, but it is amended through the correlation of the two sep-

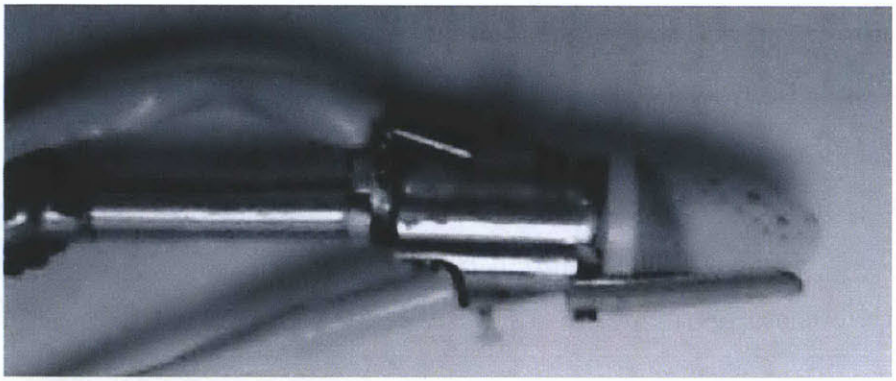

(a)

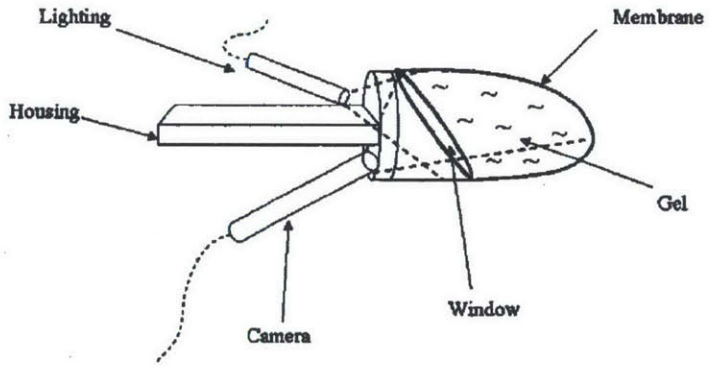

(b)

Figure 3-2: The robot fingertip tactile sensor showed in [12]

arate layers of the markers. Figure 3-1(c) shows a fingertip shaped GelForce sensor specially designed for robot fingers. The finger shaped sensor is much smaller with complicated shape, so the marker number is limited, and the boundary condition is more sophisticated. Researchers used experimental method to model the force reaction for this device, but it is limited to a particular indenter. In the whole, GelForce gave a successful practical example for measuring contact force with elastomer sensor, and cooperating with robots. But the measurement accuracy and contact resolution are not high enough.

Obinata[23] showed a similar elastomer tactile sensor, which only has one layer of aligned markers on the curved surface of a transparent elastomer sensor. They also use experimental calibration to record the force response of the patterns and use that as the base model to measure forces.

Ferrier[9] introduced another kind of tactile sensor that uses the energy method

of the membrane for mechanical modelling. They built a long hemispherical sensor filled with fluid or gel, and the encapsulating membrane is patterned with some dots. By picturing the dots' movement, they trace the deformation of the membrane, and they used the energy method to reconstruct the loading. This method, though solid mechanic background is required, is very good at handling the complex shape condition than the other models.

3.1.2 Contact Forces on GelSight Sensor

This project aims at measuring the contact force with the GelSight sensor. To simplify, a point load can be seen as a vector with 5 degrees of freedom: 2 degrees on the loading point, 1 degree on normal component force (the force component perpendicular to the contact surface), 1 degree on the shear component force (the force component parallel to the contact surface), and 1 degree on the shear force direction. The location information can be indicated from the deformation of the elastomer sensor and the deformation of the coating layer. By patterning the coating layer, the 2D motion of the layer can be traced. The major challenges are measuring the normal force and shear force respectively.

However, the contact load is usually not a point load, neither the force is uniformly distributed. The pressure distribution largely depends on the geometry property, and the loading of the surface may be deviating from the center. So the force distribution is also desired, at least the general loading area and distribution trend.

3.2 Force Response of a Elastomer Piece

3.2.1 Mechanical Property of the Elastomer

The mechanical property of the silicone or TPE elastomer is very complicated. Similar to mammal skin, they exhibit viscoelasticity. However, mammal skins are more complicated on mechanical performance in that skin comprises two main tissue layers– the dermis and the epidermis, in which the former is much thicker and contribute more

in the mechanical properties, but is highly dependent on its structure and density of the collagen fibers. Additionally, mammal skin is anisotropic in force response due to the orientation of its structural collagen, and artificial elastomers can usually be considered as isotropic.[29]

For a isotropic linear elastic material, the stress-strain relation can be expressed by

$$\sigma(t) = E\epsilon(t), \tag{3.1}$$

or

$$\epsilon(t) = J\sigma(t), \tag{3.2}$$

where E is the material's Young's modulus of elasticity, and J is the elastic compliance, and

$$J \triangleq 1/E \tag{3.3}$$

That means for linear elastic material, the strain is the single function of stress or the strain is the single function of stress, and they are both time-independent and rate-independent. In contrast, a viscous fluid has the constitutive equation as

$$\sigma(t) = \eta\dot{\epsilon}(t), \tag{3.4}$$

which means the stress is the linear function of strain rate. A viscoelastic solid material has both elastic and viscous-like characteristics, and the stress-strain relation depends on time.

Two common viscoelastic phenomena for solid materials are *stress relaxation* and *creep*, and they are the characters that are mostly looked at. Stress relaxation refers to the stress decrease with time when the strain is held constant, and creep refers to the strain increase with time when the stress is held constant. A typical response of a viscoelastic material's response of stress relaxation and creep is shown in Figure 3-3. So for a linear viscoelastic model, the strain-stress relation is

$$\epsilon(t) = J_c(t)\sigma(0) + \int_0^t J_c(t-\tau)\dot{\sigma}(t)d\tau, \tag{3.5}$$

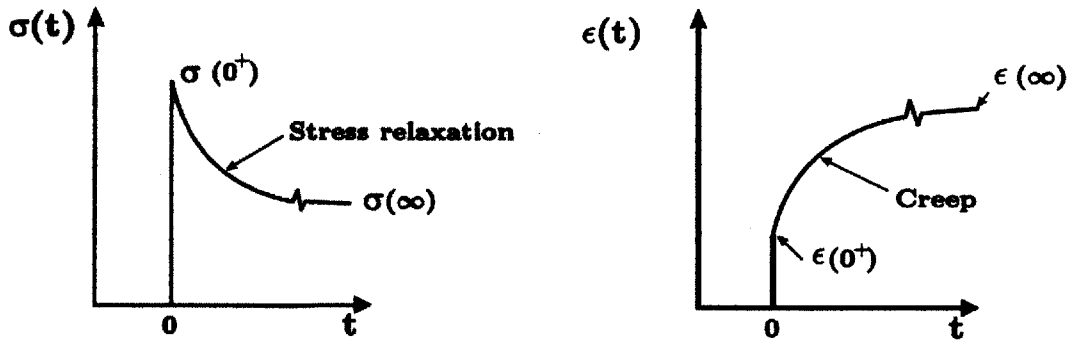

Figure 3-3: A diagram of viscoelastic material's (a) stress output in a stress-relaxation test and (b) strain output in a creep test.[5]

and the stress-strain relation is

$$\sigma(t) = E_r(t)\epsilon(0) + \int_0^t E_r(t-\tau)\dot{\epsilon}(t)d\tau, \tag{3.6}$$

in which $J_c(t)$ is the time-dependent creep compliance function, and $E_r(t)$ is stress-relaxation function.

Experimental results show that the GelSight elastomers have strong viscoelastic property. Figure 3-4 showed the axial force changes during a stress-relaxation indentation process on the elastomer material. The changing trend is very similar to that presented in Figure 3-3(a). Figure 3-5 showed the relation between experimental axial stress and stain during both loading and unloading process of a cylindrical elastomer sample. The sample has a diameter of 35.5mm, and a height of 15.10mm. In the loading experiment, the axial load displacement is controlled by a moving stage based on screw micrometer, and the axial loading force is measured by ATI Nano-17 force/torque sensor. The maximum engineering loading strain is 0.16, which is well in the range of large information. The loading step is about 0.008. After each step loading, the force has a sudden change and decreased slowly after that, and it takes long time until it reaches a general stationary state. During the loading, I waited for about 5 minutes after each step loading for the material to get a close stationary state. However, it still can be seen from the figure that the unloading stress

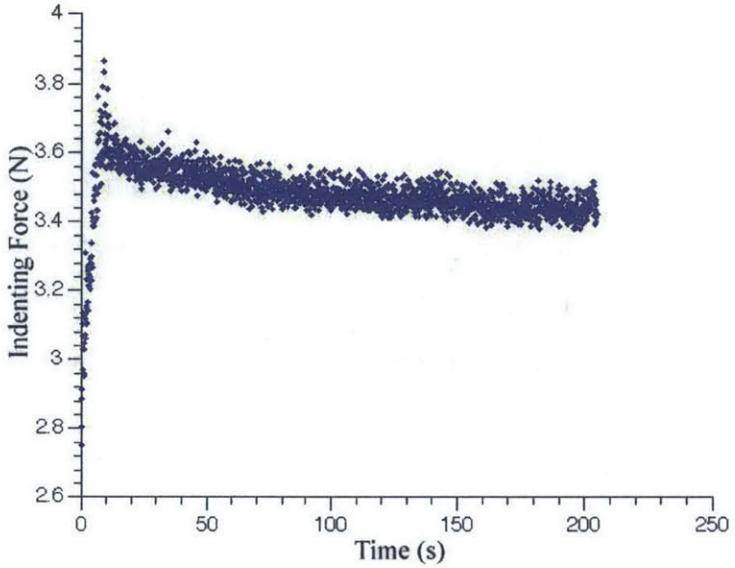

Figure 3-4: The changing of axial force during a stress-relaxation indentation process.

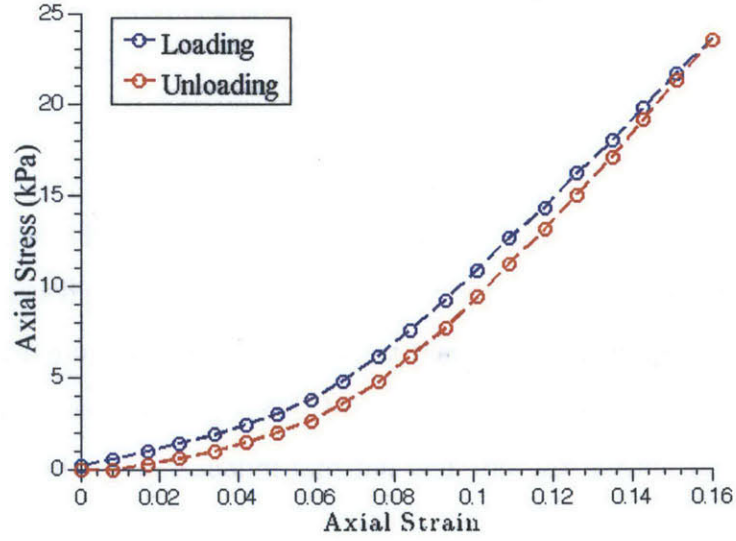

Figure 3-5: An axial loading curve of a cylindrical elastomer sample.

is distinguishably lower than the loading stress, which is a result of the material's viscoelasticity.

The figure also showed that, the elastomer is not a linear material, especially in the large deformation situation, which is very common with GelSight. In this case, it is assumed that in the quasistatic condition, the material is linear when the strain is smaller than 0.06, and after that it is also in linear relation but the ratio grows.

Due to the complex mechanical properties of the elastomer material, which is not the isotropic linear elasticity, the performance of the material largely depends on the real condition. However, the indentation experiments showed that under the fixed geometry condition, the quasistatic reaction of the material is very close to linear elastic, even for large deformation part. The conditions here include that the indenter is small compared to the elastomer. Additionally, simulation with finite-element software can help to understand the material's performance under large deformation.

3.2.2 Simulation Result of Elastomer Under Contact Forces

To learn the influences of the different geometry on the indentation results, I built finite-element models for the different indentation condition and compare the displacement field for different cases. ADINA software was used for finite-element simulation.

In the simulation, a simplest case is taken, that of a circular flat-end indenter indenting on a square faced cuboid elastomer with pure normal force. It is assumed the friction between the indenter and the elastomer is infinite. The geometry is easy because the indenter is in an axisymmetric shape, so that the 2D displacement field of the elastomer surface is mostly axisymmetric, and the 2D field can be simplified as a series of radial displacement against the distance from the indenting center.

The first comparison is on the influence of different thickness of the elastomer. The indenter chosen here is the circular flat-end indenter with the radius of 4mm, and is indented straightly on the center of the elastomer. The elastomer's surface is a square of 40mm$\times$40mm, and the thicknesses of the elastomers are 1mm, 2mm, 3mm, 4mm, and 5mm. The normal indenting force in each simulation is the same. The radial displacement series of the elastomer surface for different geometry condition is

shown in Figure 3-6(a). Each point in the plot represents a data on one mesh point in the simulation model.

It can be seen from the figure that the radial displacement curve is qualitatively similar for the different thickness cases: there is a rapid increase after the contact area and a slower decrease after that, and tend to decrease to 0 at last. A most distinct character of the data sequence is the peak. As the figure shows, the increasing rates and decreasing rates under different conditions are very similar, but when the elastomer gets thinner, the peak gets closer to the center and thus lower. Figure 3-6(b) shows the relation of the peak location and peak value according to the differences in the elastomer thicknesses. In the qualitative view, we can see that as the elastomer became thinner, the *responding area* of a certain indentation is smaller, and the responding magnitude is smaller. In other words, the elastomer is relatively more *sensitive* to the external force. Actually, the given data shows that the thinner the elastomer is, the higher the increasing and decreasing rate of sequence is higher.

In Figure 3-6(a), there are some wide "tails" in the plots of the thicker gels, which is resulted from the elastomer's border effect. The phenomenon will be discussed later in this section.

Figure 3-6(c) shows the indentation depth of the indenters for different elastomer thicknesses, to give the same normal indenting force. The red dash line in the figure is the linear fitting line of the given data that starts from $(0, 0)$. So as the figure shows that the indenting depth is generally to the linear relation of the elastomer's thickness, which means the axial indenting force is more to the relation of the pressing ratio. But as the figure shows the relation is not strictly linear, that the indentation is not a strict linear relation to the load displacement ratio and proper simulation or experiments should be done before applying the relation on a specific model.

The second comparison is on the influence of the indenter's size. In the simulation, the size of the elastomer is 40mm×40mm×5mm, and the indenters have the radius of 1mm, 2mm, 3mm, and 4mm. The indentation is only in normal direction, and the normal forces are the same for different cases.

Figure 3-7(a) shows the sequence of the radial displacement on the elastomer

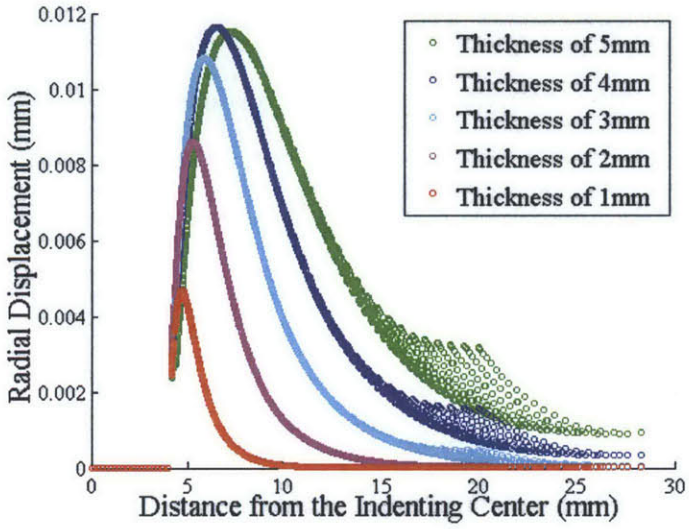

(a) Radial displacement of the surface against the distance from the indenting center.

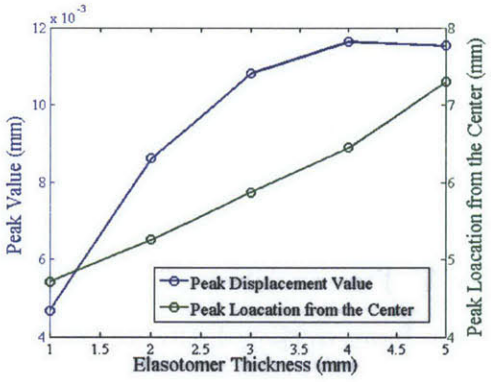

(b) Comparison of the displacement series peak value and location for different thickness of the elastomer.

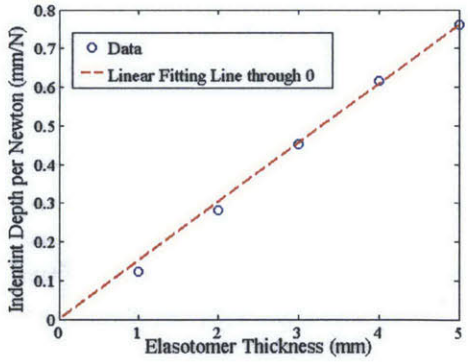

(c) Comparison of the indenting depth for different thickness of the elastomer.

Figure 3-6: The simulation result of the same indenter on elastomers of different thickness with the same normal force.

surface for different indentations, and Figure 3-7(b) shows the distance of the peak from the indenting border and the value of the peak. In the given range, the larger the radius of the indenter is, the nearer the peak of the sequence to the contact border and the lower the peak. But the relation is not linear. And Figure 3-7(a) shows that when the indenter is very small, there is an area that the surface moves inwards to the indenting center. As the indenter size grows, the trend becomes slighter , and nearly vanished when the indenter radius is larger than 2mm.

Figure 3-7(c) shows the indenting depth for different indenter sizes when exerting the same force. As the indenter size increases, the indenting depth decreases.

The third comparison is on the influence of the elastomer's area. The indenter's size(circular with a radius of 4mm), the indenting force, the thickness of the elastomer(5mm) remain. The sizes of the elastomer surface are 16mm×16mm, 24mm×24mm, 32mm×32mm, and 40mm×40mm.

Figure 3-8(a) shows the radial displacement sequence of the results. As shown, in the area that is far from the border of the elastomer, the displacement field is generally the same for different elastomer sizes; and in the area that approaches the elastomer's border, the displacement magnitude becomes larger than it supposed to be if the elastomer is large enough. There are also "tails" at the end part of each plot. That is because the indenter is circular while the elastomer surface is square, and the distance between the elastomer border and the indenting center differs on each direction. So on the same x-axis point the distance to the border differs, which make the data set divergent over there. Figure 3-8(b) shows the indenting depth, that as the size of the elastomer becomes larger, the indenting depth is lower, as well as the decreasing rate. However, the indenting depths are very similar for different elastomer sizes, as far as the elastomer size is not too small compared to the indenter.

Another simulation also compare the influence of the elastomer sizes, and the parameters here is the same as the previous experiment, except for the elastomer thickness is 2mm instead of 5mm. The result of the radial displacement is shown in Figure 3-9(a). Similarly, as the area approaches the elastomer border, the displacement becomes higher. But for the thinner elastomer, as analyzed earlier, the

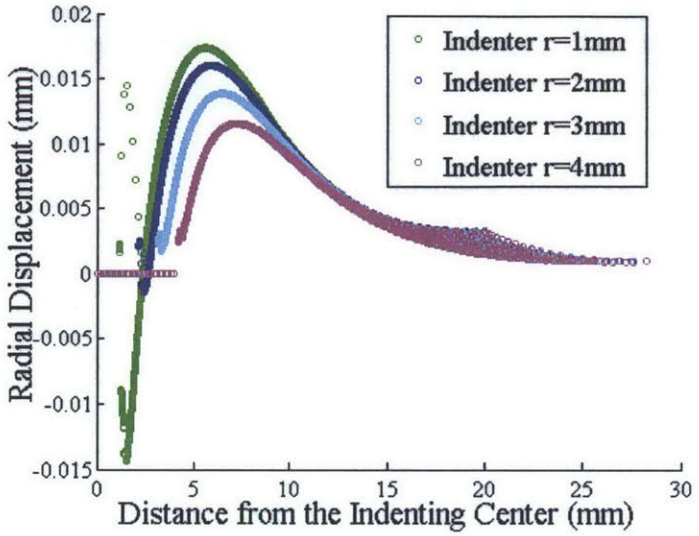

(a) Radial displacement of the surface against the distance from the indenting center.

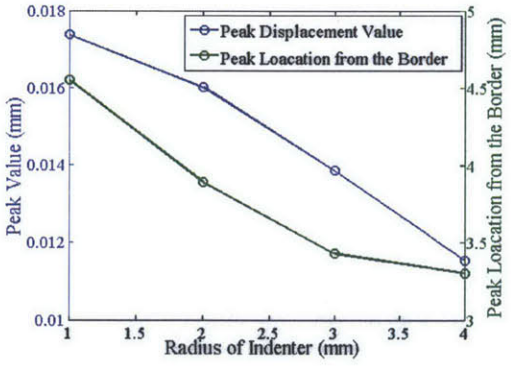

(b) Comparison of the displacement peak value and location for different thickness of the elastomer.

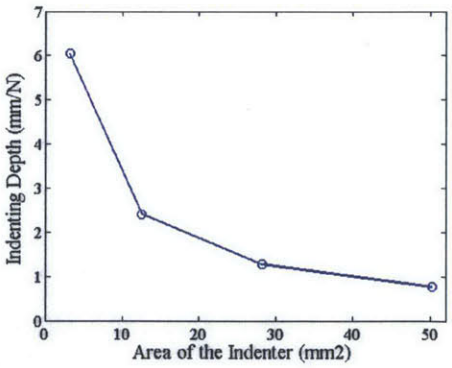

(c) Comparison of the indenting depth for different indenter sizes.

Figure 3-7: The simulation result of different indenter sizes on the same piece of elastomer.

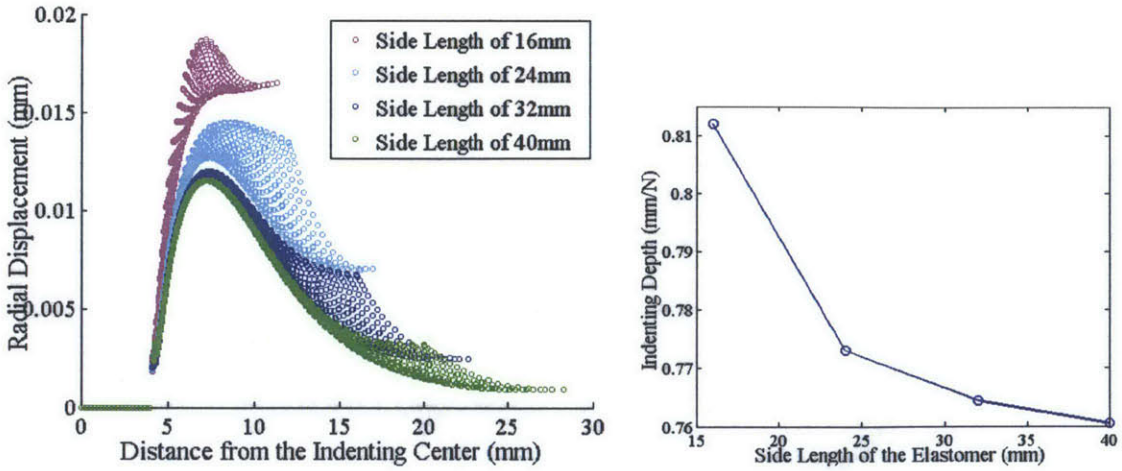

(a) Radial displacement of the surface against the distance from the indenting center.

(b) Comparison of the indenting depth for different elastomer sizes.

Figure 3-8: The simulation result of different elastomer surface sizes with thicker elastomers.

indenting influenced area is smaller, and the displacement sequence declines to near zero before it approaches the elastomer border. So the influence of the elastomer size is not so distinct in this case.

Similarly, as shown in Figure 3-9(b), when the elastomer size is smaller, the indenting depth is larger, but the difference is small.

3.3 Experimental Set-up

In the experiments, I wish to research into the elastomer's response to different indentation force. The load force has 3 degrees of freedom: one in the perpendicular direction to the elastomer surface, or called normal force; one in the tangential direction to the elastomer surface, or called shear force; and the last one is the direction of the shear force in the contact surface. As the elastomer is isotropic, the shear force direction is easy to know, and the shear force is independent to the force direction, so only two degrees of freedom: normal force and shear force magnitudes, are needed for the research, and an experimental setup which can provide controlled normal and shear load is required.

Figure 3-10 shows the experimental setup for the indentation experiments on the

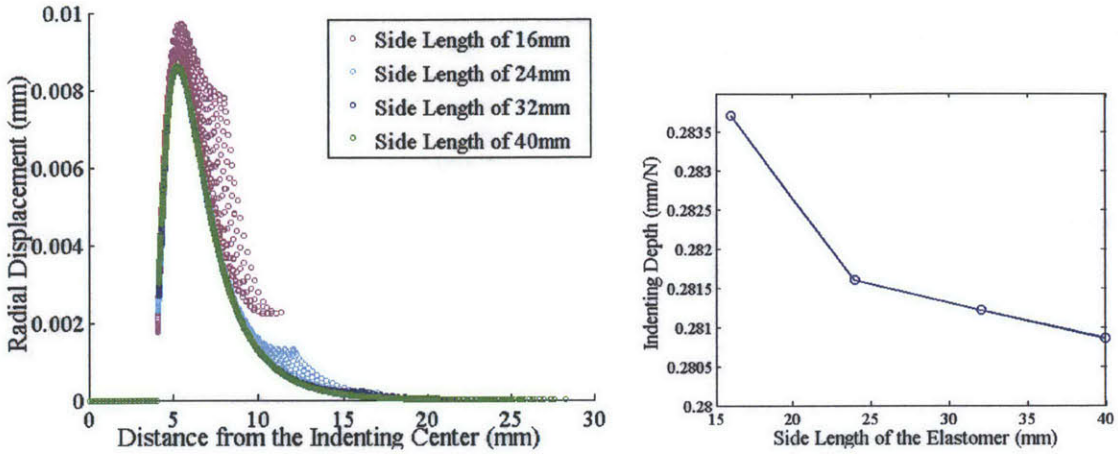

(a) Radial displacement of the surface against the distance from the indenting center.

(b) Comparison of the indenting depth for different elastomer sizes.

Figure 3-9: The simulation result of different elastomer surface sizes with thinner elastomers.

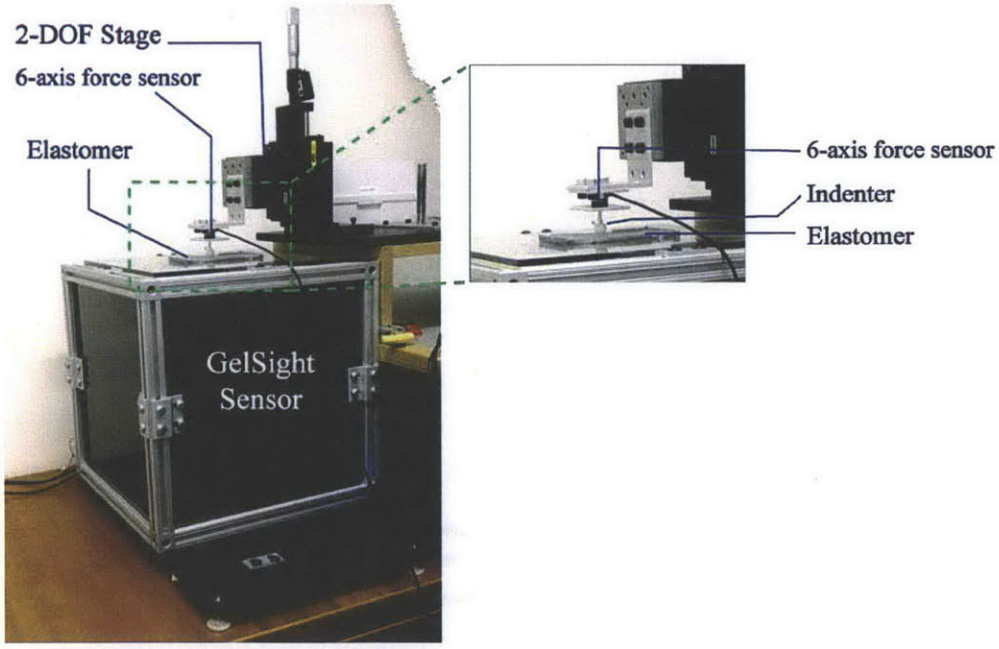

Figure 3-10: The overall set up for indentation experimental with the box-setting GelSight device.

Figure 3-11: Different indenters used in the experiments

box-setting GelSight. The system is made up by: a box setting GelSight device whose measuring surface is upward; a balancing stage in the bottom of the GelSight device to make sure the elastomer surface is vertical to the normal loading direction; a 2 DOF moving stage with screw micrometer that can move the conjoint indenter in vertical or horizontal direction independently, with the measurement precision of 0.002mm; a indenter; a 6-axis force torque sensor between the indenter and the supporting stage to measure the loading force.

Figure 2-3(a) shows the top view of the box setting GelSight sensor that is specially designed for research use. This design is stable for fixation, and has a high resolution machine vision camera, a well-controlled light system, and a large view area with larger size of elastomer sensor. All these factors made the device a good choice for a well-controlled experimental platform with possibly little experimental error.

Indenters with different sizes and shapes are made for the experiment, as shown in Figure 3-11. The indenters are made of acrylic, which can be considered as rigid compared with the elastomers. Indenter shapes include sphere, cylinder, and circle, ellipse, rectangle and triangle with flat ends. The flat-end indenters are made by laser cutting. All the indenters are glued to a standard steel pin, which is used to connect the head to the stage. The linear dimensions of the indenters are from 6mm to 12.7mm, which is small compared to the elastomer, but not too small to damage the elastomer.

The marker elastomer sensor used in the experiment is like the one shown in Figure 2-4(a), with circular dot marketed aligned in standard array. The diameter

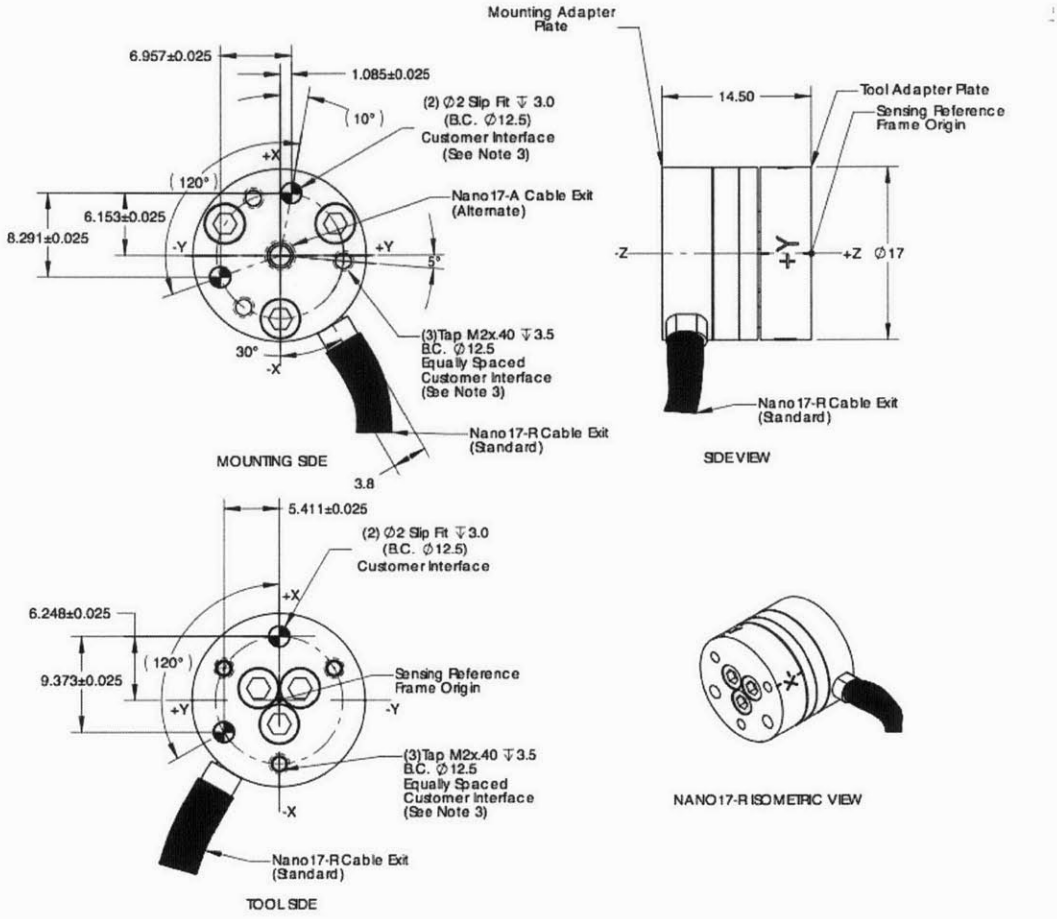

Figure 3-12: Drawing of the ATI Nano17 force torque sensor.[1]

of the marker is 1.4mm, and spacing between to adjacent markers is 2.52mm. In a camera view, there are $18 \times 16 = 288$ markers.

The force torque used in the experiment is ATI Nano 17 sensor (shown in Figure 3-12), which measures the 3-axis force and 3-axis torque. The sensing ranges of the sensor is 70N for axial force and 50N for tangential force, 500Nmm for the torques, and the resolution is 1/80N for forces, 1/16Nmm for the torques.[1] However, in experiments due to the noise of sampling system, the resolution is not that high. But it is considered high enough to calibrate the loading force for GelSight.

3.4 Algorithm for Tracking Pattern Deformation

To build the displacement field of the plane, the first method I used is the optical flow method based on Lucas-Kanade algorithm[22] for image registration. The image registration method works on aligning two images and find the shift vector between them. A detailed introduction into the algorithm and the application into optical flow method is introduced in [6].

In this project, the object information is the displacement field of the elastomer's surface, which is marked by the black patterns. The planner positions of the markers are captured by the GelSight camera in each frame, and the movement of the black markers represents the local movement of the elastomer surface. However, the difference changing in the elastomer background may be large interference to the marker tracking, and the change is mostly resulted in the geometry of the contact surface.

In this specific case, to track the patterns with better precision in optical flow method, the interference should be considered. As the artificial black markers have small brightness gradient, the image registration is mostly restrained by the contour shape. So firstly I segment the markers from the background. This is mainly based on the color: the markers are black or gray in all the frames; other interference area caused by geometry change, are mostly bright in one or two channels in the color image. This is resulted from the lighting design of the sensor. So after converting the color frame into a grayscale image, the artificial black markers can be segmented according to the brightness.

The basic relation of tracking the displacement vector $\boldsymbol{u}$ for a grayscale image patch $\boldsymbol{I}$ is

$$\boldsymbol{A}\boldsymbol{u} = \boldsymbol{b} \tag{3.7}$$

where

$$\boldsymbol{A} = \begin{bmatrix} \sum I_x^2 & \sum I_x I_y \\ \sum I_x I_y & \sum I_y^2 \end{bmatrix} \text{ and } \boldsymbol{b} = -\begin{bmatrix} \sum I_x I_t \\ \sum I_x I_t \end{bmatrix}, \; I_x = \frac{\partial \boldsymbol{I}}{\partial x}, I_y = \frac{\partial \boldsymbol{I}}{\partial y}, I_t = \frac{\partial \boldsymbol{I}}{\partial t}, \tag{3.8}$$

In the real case, as the existence of interference, some pixels are more *reliable* in calculating the overall displacement vector. The pixels near the marker border are considered more reliable, as in other places, the patch differential is largely caused by noise. So I applied a weight scalar $w(x, y)$ in the calculation, and the pixels on near the border area are given larger weights:

$$w(x, y) = I_x^2 + I_y^2 \tag{3.9}$$

The relation of $\boldsymbol{u}$ in weighted calculation is:

$$\tilde{\boldsymbol{A}}\boldsymbol{u} = \tilde{\boldsymbol{b}} \tag{3.10}$$

where

$$\tilde{\boldsymbol{A}} = \begin{bmatrix} \sum I_x^2 w(x,y) & \sum I_x I_y w(x,y) \\ \sum I_x I_y w(x,y) & \sum I_y^2 w(x,y) \end{bmatrix} \text{ and } \tilde{\boldsymbol{b}} = -\begin{bmatrix} \sum I_x I_t w(x,y) \\ \sum I_x I_t w(x,y) \end{bmatrix}, \tag{3.11}$$

Then $\boldsymbol{u}$ is calculated by the reverse method, and the displacement of the local marker area is known.

The problem with the optic flow method is that it is not effective when tracking large displacements. For example, when the displacement of a marker is larger than half its size in any dimension, the optic flow method makes a large error. This happens very often, especially with the portable device: when the elastomer is very thin, the marker displacement can be very large or evan larger than its own dimension. Additionally, on the boundary part of the contact surface, there is usually a large change in the brightness of the whole view, which is a large interference for the optic flow method. In this case, a new tracking method based on tracking the centroids of the markers are taken to reduce the errors.

The procedure of locating the centroids of the markers is shown in Figure 3-13: the raw RGB image is converted to grayscale and low-pass filtered to reduce noise. Then the markers are segmented from the background. Since the markers are in black,

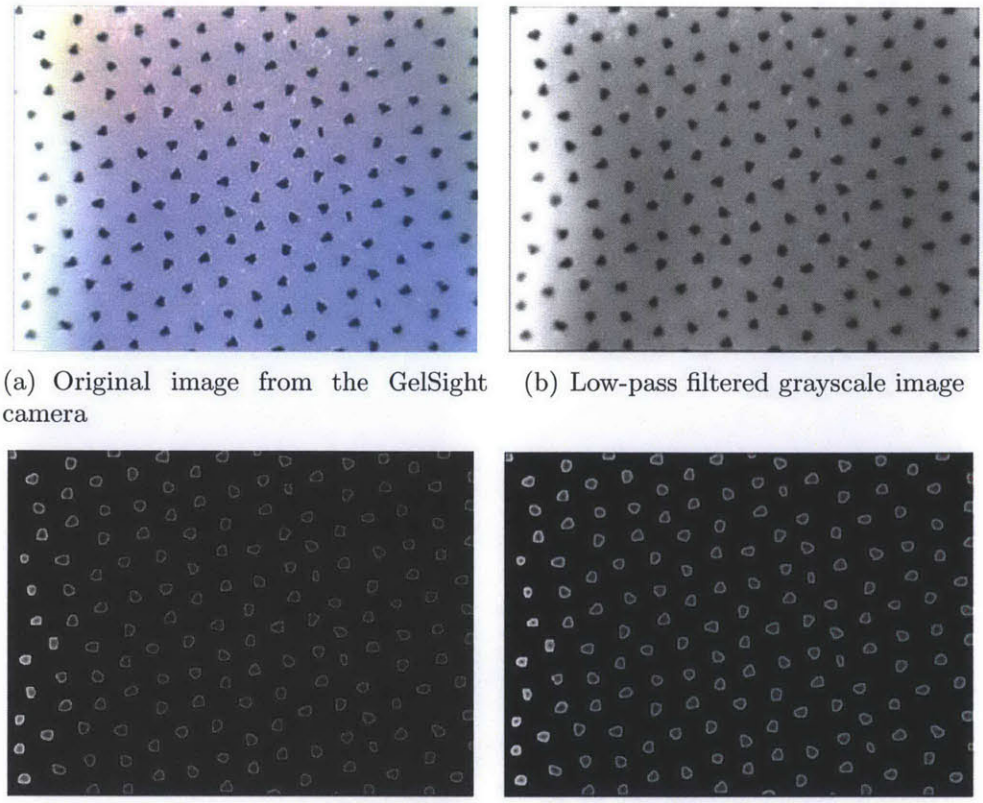

(a) Original image from the GelSight camera

(b) Low-pass filtered grayscale image

(c) Isolated markers from the grayscale image

(d) Centroids of the markers

Figure 3-13: Finding the centers of the markers from the original view of the GelSight camera

which is much darker than the surrounding area and has more uniform components in all the color channels, they can be identified by brightness in the grayscale image. So by making a threshold of local areas the markers can be segmented. Then the centers of the markers are considered as the centroids of the darkness in each marker area.

After the marker centers in each frame are found, the center positions in different frames are paired and compared, and the displacements are known. Similarly, by interpolating the displacement on the marker the 2D displacement field of the how elastomer surface within the camera view is known.

Experiments showed that when the marker displacement is small, the calculation results of displacement are very similar in the two ways; when the displacement is large, the method of tracking the marker centers is precise while the optical flow

method makes large errors. The center-tracking method also has much better tolerance in the background interference, although not fully avoiding it.

Chapter 4

Contact Forces Measurement with Circular Flat-ended Indenter

This chapter introduced one of the most basic contact force cases: the GelSight device is the large box setting prototype, and the indenter is circular flat-end in shape. In the cases that the elastomer medium is thick, and large enough compared to the indenter, and the camera view range is much larger than the contact area.

Both simulation and experiments on the normal load and load are conducted in the chapter.

4.1 Simulation

To get an insight of the elastomer's deformation during indentation, I used finite-element software to simulate the elastomer under the specific indentation situation. The software used here is ADINA. The model is of the exact size of the real elastomer used in the experiments and the indenters. As a simplification, it is supposed that the elastomer is an isotropic linear elastic material, which is not exactly the real case but very near to the elastomer's quasistatic response to the simple pressing and shear cases when the indenter is considered small to the elastomer. However, the simulated results should be compared with the experimental data to ensure that the approximation is acceptable.

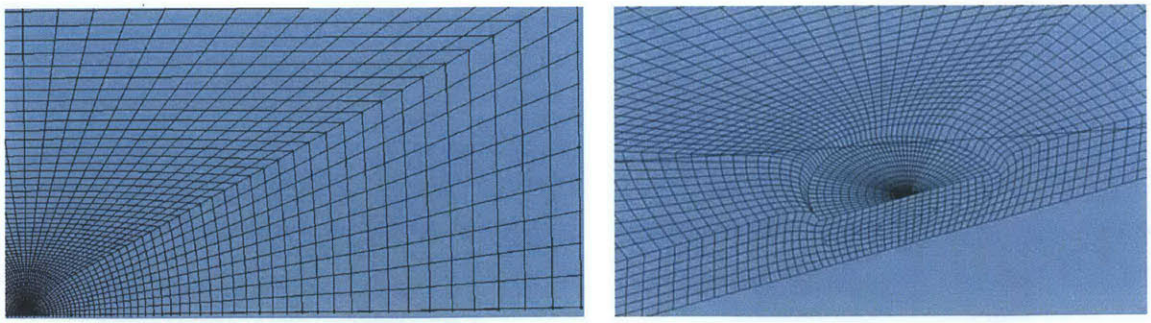

(a) Meshing of the elastomer (b) Deformed mesh under normal load

Figure 4-1: The meshing of the elastomer for circular flat-ended indenter.

The boundary conditions of this model are that the bottom surface of the elastomer is fixed, and the other surfaces are free; the contact surface of the indenter and the elastomer is a circular area with the same displacement, that is, this area has the same displacement as the indenter, which means there is infinite friction between the indenter and the elastomer. In reality, the friction depends on the contact material and some other properties of the surface, such as moisture and dust and other things, and the friction influences the elastomer's deformation. It is not considered in the simulation for the measurement difficulty, but its influence can be predicted according to the experimental results.

The meshing of the elastomer in one horizontal layer is shown in Figure 4-1(a). It is not evenly meshed, because for finite-element software, meshes of the shapes that are nearly square are more preferred. And in this indentation case, the deformation is the largest in the contact area, and near the contact boundary the deformation has the largest derivative, so in this area the mesh is denser, and the place far away from the indentation area, either the deformation or deformation derivative is small, so the mesh is sparse. The elastomer size is the same as the one used in experiment:125mm $\times$ 70mm $\times$ 4.2mm, the whole model contains 167 thousand nodes, and the spatial resolution near the contact boundary area is 0.2mm.

Figure 4-1(b) shows the deformation of the simulation model under a normal load.

The simulation result shows that the elastomer's deformation is in a good linear relation to the load within a wide range.

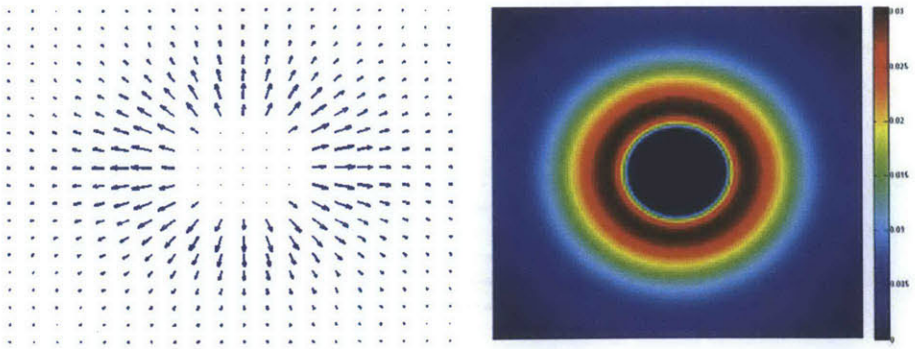

(a) The displacement field of the elastomer surface.

(b) The magnetite of the surface displacement in radical direction.

Figure 4-2: The simulation result of normal indentation for the elastomer

In the normal indentation case, the simulated elastomer's surface planner deformation is shown in Figure 4-2(a). It can be seen that during the pressing, the elastomer has a trend of expanding outwards in the 2D space. As the indenter is axisymmetric, the displacement field is also axisymmetric, and to the radical direction. The radical displacement magnetite in this case is shown in Figure 4-2(b). The simulation result shows that, the displacement magnetite of each meshing point is linear to the normal load.

For the pure shear load indentation, the deformation of the elastomer surface in the 2D plane is shown in Figure 4-3(a). The displacement of each point is also linear to the shear load. The decomposition of the shear displacement field in the shear direction and perpendicular to the shear direction is shown in Figure 4-3(b) and Figure 4-3(c) respectively. The data shows that the displacement is mainly in the shear direction. The displacement field in shear direction is symmetrical along both x axis and y axis (here x axis is supposed to be along the horizontal direction, which is the shear direction, and y axis is along the vertical direction), and along the shear direction the displacement component decreases slowest. The perpendicular direction displacement field is central symmetric along the origin point. In all. the displacement field of the pure shear load is similar to the fluid flow passing a narrow valve.

In the simulation, the displacement field of the elastomer surface also shows the

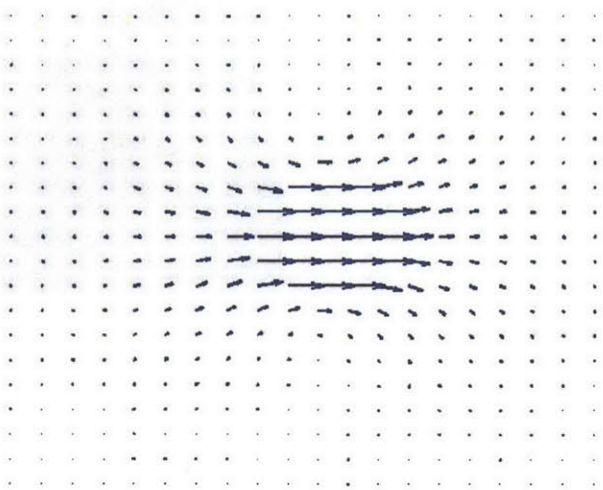

(a) Displacement field of the pure shear load

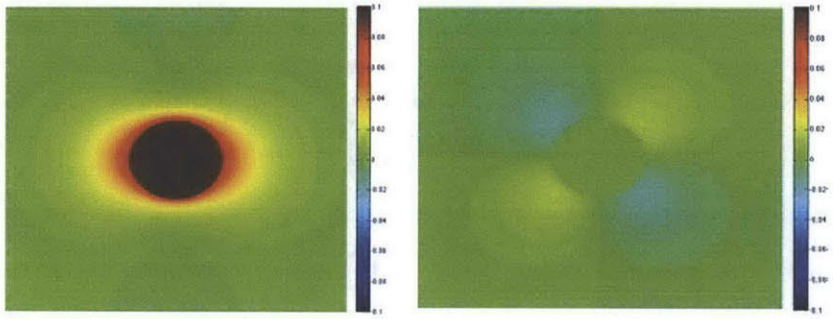

(b) Displacement magnitude in the shear direction

(c) Plane displacement magnitude perpendicular to the shear direction

Figure 4-3: Simulated displacement for the pure shear load.

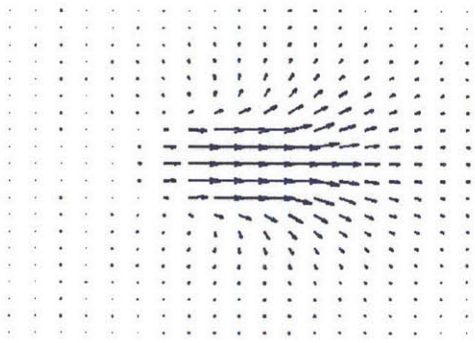

Figure 4-4: Simulated displacement field for the elastomer under both normal and shear load.

interposition property. For example, when applying a random external indentation load, the load can be considered as the superposition of a normal load and a shear load in the shear direction, and the responding displacement field also equals to the superimposition of the displacement fields to the two loads separately. An example of the displacement field to the resultant force is shown in Figure 4-4.

4.2 Indentation Experiments

In this part, I conducted the experiment of the circular flat-ended indenter indenting on GelSight with normal and shear load. The experimental setup is introduced in Section 3.3. The setup can apply a normal and shear load respectively, with the screw micrometer to measure the load displacement. The force/torque sensor connected to the indenter is able to measure the real time forces in the three directions about the load.

The indenters used here is in circular shape with diameters of 9.5mm and 12.68mm, and is indenting in approximately the center part of the elastomer. The elastomer size is 125mm $\times$ 70mm $\times$ 4.2mm.

Only the quasistatic responses of the elastomer is recorded in the experiments. That means, according to the viscoelastic property of the elastomer, it will take infinite time for the elastomer to reach an equilibrium state, but the stress relaxation is in an exponential decrease way, so after a period of time the stress will remain in a relatively stable state, or quasistatic state, which is very near to the equilibrium state. The quasistatic state can also be seen from the change in the load force and the displacement derivative. Practice showed that mostly 3 minutes is enough for the elastomer to reach a quasistatic state in an increasing load experiment.

The load displacement is controlled in the experiments. The maximum loading control for normal load is 20 percent of the elastomer's thickness, and the load step is 2 percent of the thickness; the maximum shear load is 1mm, which is 7.9 percent of the indenter's diameter, and the step shear load is 0.05mm.

The experimental results showed that similar to the simulation results, the dis-

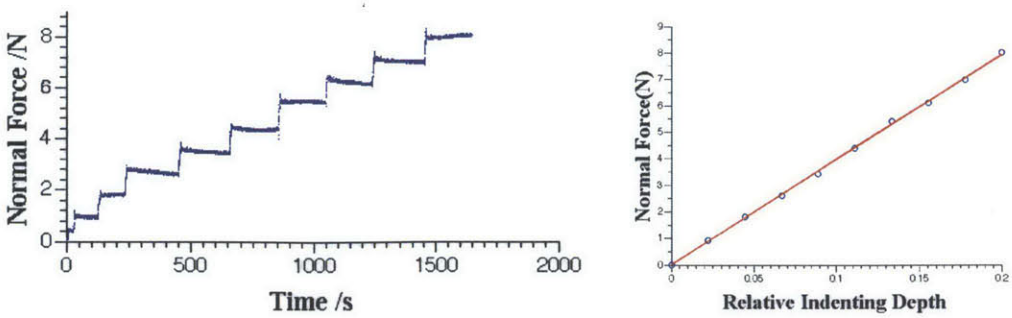

(a) The normal force changes during the indentation experiment

(b) the relation of normal force and normal load displacement

Figure 4-5: The normal force of indentation during the experiment.

placement of the elastomer's surface displacement is also in close linear relationship to the shear and normal load in the elastic range, and can also be considered as the superposition of the different load. So the response of normal load and shear load can be measured separately.

4.3 Experiments on Normal Indentation

The normal indentation experiment takes the flat-ended circular indenter with a diameter of 9.5mm, and increase the normal displacement load in even steps to test the elastomer's response. The relation between the normal force and time is shown in Figure 4-5(a). The steep steps in the plot are caused by the step increase of the normal displacement load. The plot showed the material's viscoelasticity in that after each load, that there is a distinct peak in the force, and then the force decreases slowly and finally reached the quasistatic state. The plot also showed that due to the hardware limitations, there is some fluctuation in the force/torque sensor's readings. I took the average value of a short period of the last part in each loading stage as the final loading normal force.

Figure 4-5(b) shows the relation between the normal load force and the load displacement, and the red line is the fitting line of the data. It can be seen that for the flat-ended circular indenter whose size is small, the relation between the normal load force and load displacement is in a good linear relation within a fairly large range

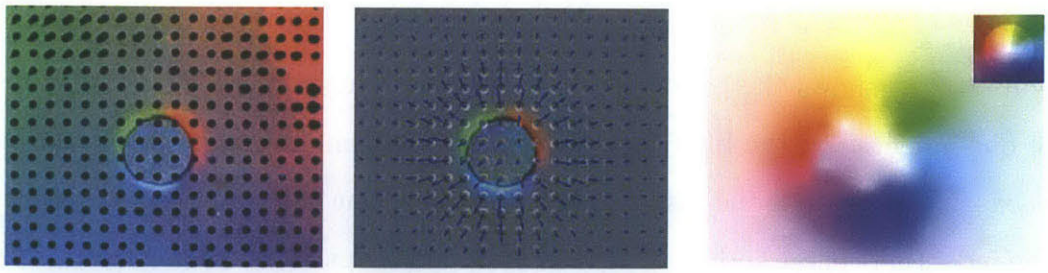

(a) The GelSight camera view during a normal indentation load

(b) The displacement field shown in vectors.

(c) The interpolated displacement field shown in color vectors.

Figure 4-6: The 2D displacement fields of the elastomer's surface based on tracking the markers.

(0.2 in this experiment).

Figure 4-6 shows the displacement of the markers in the normal indentation experiment. Figure 4-6(a) shows the image got by GelSight camera in the indentation experiment. The camera view clearly shows the clue of the circular indenter indenting on the elastomer, and the black markers. Figure 4-6(b) shows the overall displacement of each marker, and Figure 4-6(c) shows the interpolated displacement field of the whole elastomer surface according the the marker displacement. The display method in Figure 4-6(c) is the color vector display method: the hue of the color represents the vector direction, and the brightness of the color represents the magnitude. The reference of a standard vector field is shown in the top-right corner in the figure.

The major error in tracking the marker displacement results from the influence of the background changes because of the contact with the indenter. This happens in the boundary of the indenter, and the markers in this area have large displacement tracking error. Another error is caused by the setup, that there is a small angle between the indenting direction and the elastomer's surface normal. So slight torques occur, and the displacement field has a little deviation from the ideal displacement field.

Similar to the simulation result, it can be seen that the displacement field is also in radical direction from the indenting center. So the displacement of the normal field can be considered as a relation between the distance of the position from the indenting center, and the radial displacement of that point. In this case, the 2D field

can be represented by a 1D series.

Figure 4-7(a) shows the result of the experimental marker's radial displacement field of one indentation(the blue dots), as well as the simulation result(the red line). The x-axis in the figure is the distance from the indenting center. It can be seen that near the indenting center and on the indenter boundary parts, there is large deviation on the marker displacement, while in the area that is away from the contact area, the marker displacements are more concentric. The deviation in the contact part is caused by the small indenting angle deviation. The deviation on the indenting border part is caused by the calculation error due to the interference of the background change. The sparse of the sampling points is also an obstacle in measuring.

The experiments show that with the same indenter, different indentation load would produce a displacement field of similar shape, and the displacements of the markers are in a general linear relation to the load.

The red curve in Figure 4-7(a) shows the simulated displacement field of the same indentation case, with some arbitrary normal load. The plot is multiplied by a scale factor and added a small factor to make a best fit to the experimental data. The scaling factor can be considered as the scaling of the indentation load. As described in the Section 4.1, the simulated displacement field is in a linear scale relation to the loading force or loading displacement, so multiplying the displacement field by a factor makes the displacement field of another indentation, with the load to the same scale of the simulated field. The additive factor is caused by the friction between the indenter and the elastomer. In the simulation it is assumed the friction is infinite between the indenter and the elastomer, which is expressed as the flat part within the contact area in the figure. In reality, due to the surface expansion in the pressing, there is a trend of the elastomer surface to spread outwards, which is compensated by the additive factor. So in this case, the multiplication scale between one simulated field and the one that fit the experimental field indicates the indenting load.

To make a fit of the simulated curve and experimental data, different sampling points are given different weights, because some sampling points are considered as less "reliable" than the others due to the measure error. As the previous mention, the

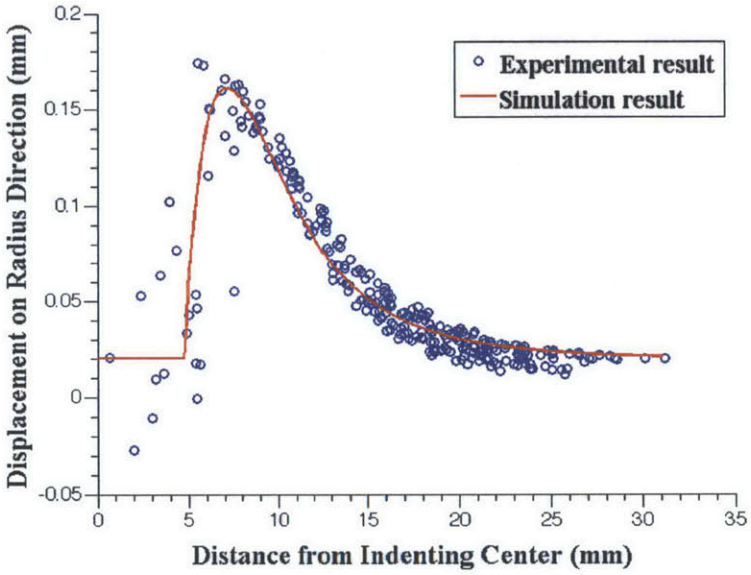

(a) The radical displacement of the markers and their distance from the indenting center

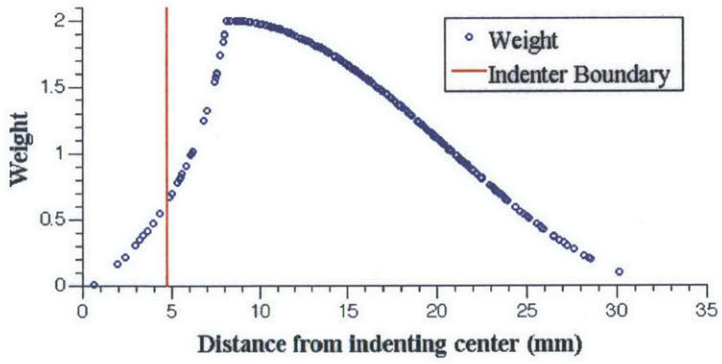

(b) The weigh for fitting the experimental result and the simulation result.

Figure 4-7: The displacement field sequence of the experimental result and the simulation result.

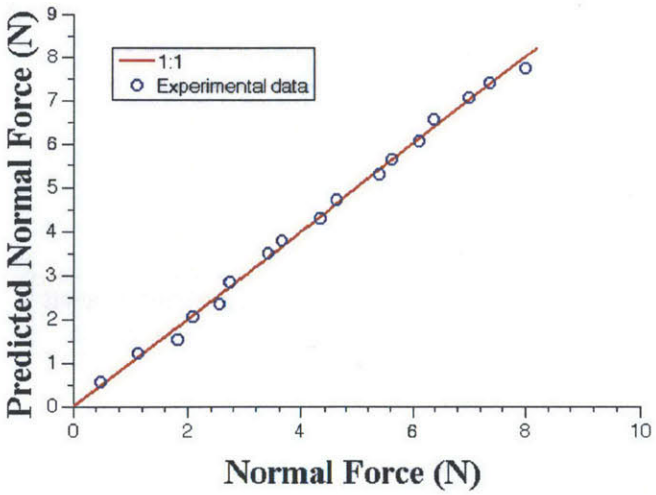

Figure 4-8: Comparison of the predicted normal force from the displacement field and the exerted force.

sampling points with in the contact surface and on the contact boundary have a small reliability. And in the remote area, the displacement is very small, so that the error rate is large. Markers in the area that is near the border, where the displacement is large and calculation is less influenced by the background effects, is considered as more reliable area. The function for fitting weight used in the experiment is plotted in Figure 4-7(b). The red line in the figure is the boundary of the indenter.

This means that if the experimental displacement field well fits the simulation result, the fitting scale shows the indentation force. Figure 4-8 displays the comparison between the indentation pressing force and the predicted force using this method. It proves that the predicted force is very close to the real normal force, thus this is a reliable way to measure normal force in this indentation condition.

4.4 Experiments on Shear indentation

The shear indentation experiment is also done with the experiment setup introduced in Section 3.3. The elastomer used here is the same as the one used in the normal indentation experiment:125mm $\times$70mm$\times$4.2mm, and the indenter is a circular flat-ended indenter with a diameter of 12.68mm. Since there cannot be shear force without

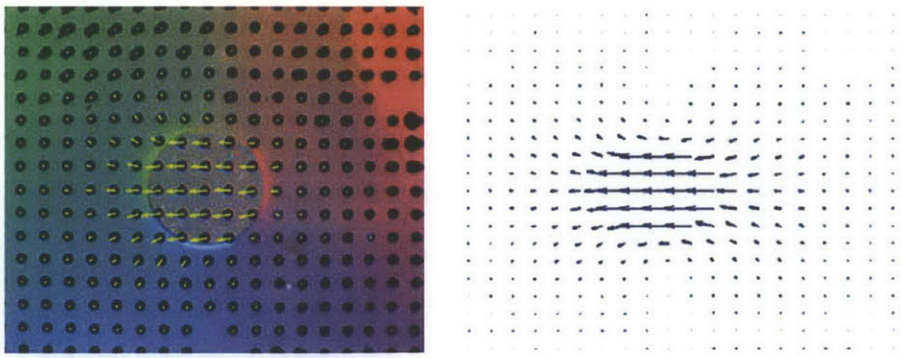

(a) The GelSight view of the markers in a shear indentation experiment, withe the displacement of the markers displayed.

(b) The simulation field of pure shear displacement field

Figure 4-9: The displacement of the markers in a shear indentation experiment.

normal force, in the indentation experiment a series of shear load with the same normal load are applied. A view from the GelSight camera of the shear load is shown in Figure 4-9(a) , and the displacement of the markers is also displayed on the scene. By subtracting the displacement field of the pure pressing from the displacement field, the displacement field of the pure shear is get. It is in a very similar shape as the simulated pure shear field shown in Figure 4-9(b). The shear field of the circular flat-ended indentation can also be get from the decomposition of the resultant field according to the geometry characters.

In the experiment, the shear load displacement of is controlled by the screw micrometer stage, and both the normal force and shear force on the indenter are measured through the force/torque sensor. Similar to the normal indentation experiments, during the shear experiment the elastomer also performed viscoelasticity, in that there is always a stress relaxation response after each load increase. I also waited around 3 minutes after each load change until the force is generally stable as time goes, which is considered as the quasistatic response of the elastomer.

As the shear load increases, firstly the friction force between the indenter and the elastomer is large enough that there is no relative movement between the indenter and the elastomer, and we call it shear; when the shear load is very large, and there is all-round relative displacement on the contact surface, we call it slip; and between them

there is a state called *incipient slip*, which means there is relative displacement on part of the contact area , and it is going to slip if the shear load increases. It is important to learn the state of shear, slip, and incipient slip for a tactile sensor for it has many practical use. A common example is for robot grasping: when detecting whether a robot successfully holds an object, the best indication is whether the object is slipping on the contact surface; and when the contact surface is in the state of incipient slip, it means that the grasp is "unsafe" and further procedures are required to guarantee the grasp to be safe, like increasing the grasping force.

In the simulation part, as it is assumed the friction on the surface is infinite, it is always in shear state. The experimental results show that during the shear period, the shear displacement load, the shear force load, and the elastomer's surface displacement field are all in linear relation.

Figure 4-10 shows the relation between the quasistatic shear force and the shear load displacement. The blue dots in the figure are the experimental data, and the red line is the linear fitting line of the first few experimental data. The first part of the experimental data is in the shear stage, that the load displacement and the shear force are in good linear relation; then it grows to incipient slip and slip state, and the shear force and displacement are not in linear relation any more. During the slip state, the shear displacement increases, but the shear force does not increase anymore.

The displacement field of the pure shear is not central symmetric as the pressing field, as the shear load is directional. Section 4.1 shows the simulated displacement field can be decomposed in two perpendicular directions, and the field component of each direction is asymmetric along two perpendicular axes. But the field on the shear direction has a much larger magnitude than the one on the vertical direction. So in the analysis, only the displacement on the shear direction is considered, thus this decomposed field is considered as more representative of the whole displacement field. The experimental result is very similar to the simulation field qualitatively. As shown in Figure 4-3(b), the decomposed field has the largest and uniform magnitude in the central part which is in contact of the indenter, and decrease at different derivatives

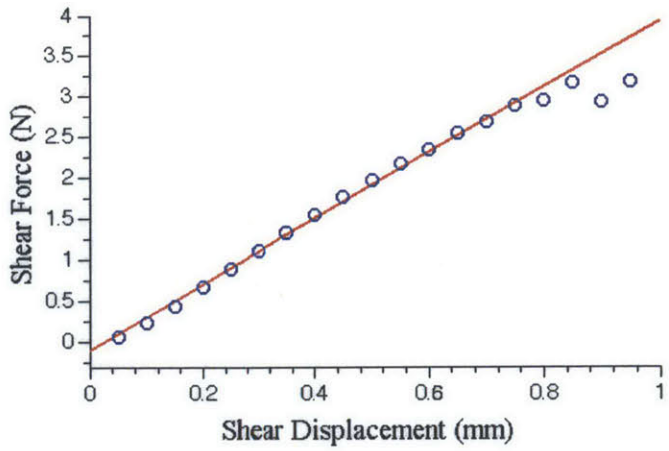

Figure 4-10: The relation between shear force load and load shear displacement in the experiments.

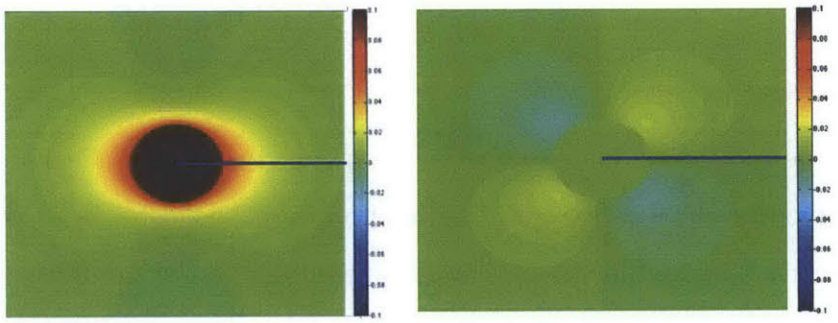

(a) (b)

Figure 4-11: The displacement magnitude field in x and y directions of the pure shear in the simulation, with the central line marked.

on different directions. On the shear direction, the slope is the smallest. Now a line is drawn from the indenting center along the shear direction is shown in Figure 4-11, on which the slope of the shear direction displacement field is the smallest, and the magnitude change on this line is considered as the most representative of this field. The line is called *central line* for short, which is also considered as an important representative of the shear displacement field.

In this case, to simplify the procedure of fitting the experimental shear displacement field to the simulation field, we can just fit the two representatives of the displacement field: the decomposed field magnitude on the shear direction, and the shear direction displacement on the central line. As the simulated displacement field is in

linear relation to the load, by multiplying a scale factor to the displacement field, it became the displacement field of another shear load which is to the same scale of the original load. And by multiplying a scale factor of a known displacement field of a load in the simulation, the field fits with a given experimental displacement field. Figure 4-12(a) and Figure 4-12(b) show an example of fitting the experimental data to the simulation field on the field magnitude and the central line magnitude separately. In Figure 4-12(a), the curved surface is the scaled simulated displacement field in the shear direction of the same indentation condition as the experiments, and the black dots in the figure are the displacement on shear direction in the experiments. In Figure 4-12(b), the blue line is the scaled simulated displacements on the central line, and the red line is the experimental displacements. The example shows that the experimental fields match well with the simulation results, and the two representatives of the displacement field work well.

However, the well-matching cases mostly happened when the shear load is small, that the relative movements between the indenter and the elastomer is very small or even none. This is very similar to the condition assumed in the simulation. But when the load is large, and there are partial slip between the indenter and the elastomer, the experimental data does not match well with the simulation. Figure 4-12(c) and Figure 4-12(d) show an example of bad match. In this case, partial slip happens, and from the displacement field it can be seen that under the contact area, the displacement field is not uniform. When comparing with the simulation result, this is shown by that the displacement of the periphery area matches well with the simulation data, but in the center part of the contact area the experimental data has a significant larger displacement that the simulated case. For the fitting purpose, it is supposed that the displacement of the periphery area is more reliable, so a larger weight is given to this area. The fitting weight is a function of the distance from the indenting center, and the area that is outside but near the contact area has the largest weight.

Figure 4-13 shows the displacement on the central line of different shear load in one experiment. The maximum displacement load in this experiment is 0.80mm, where the state is incipient slip. With the shear load increases, the displacement

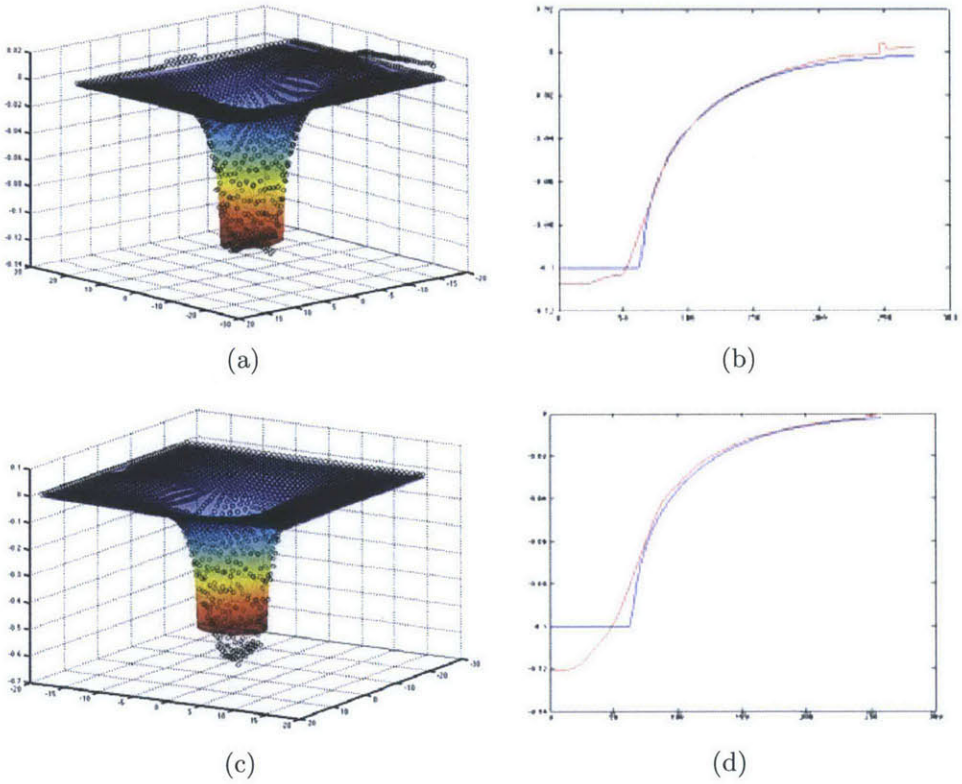

(a) (b)

(c) (d)

Figure 4-12: Two examples of fitting the experimental shear displacement field on the simulation field.

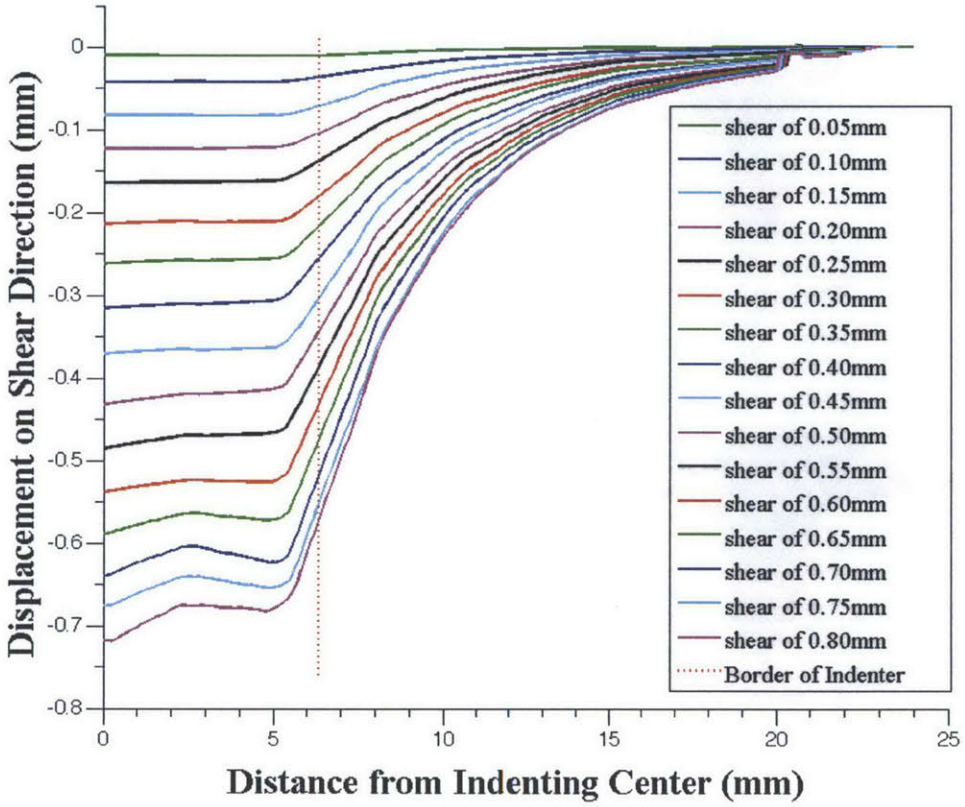

Figure 4-13: The experiment result of the shear-direction displacement on the central line of the elastomer under different load.

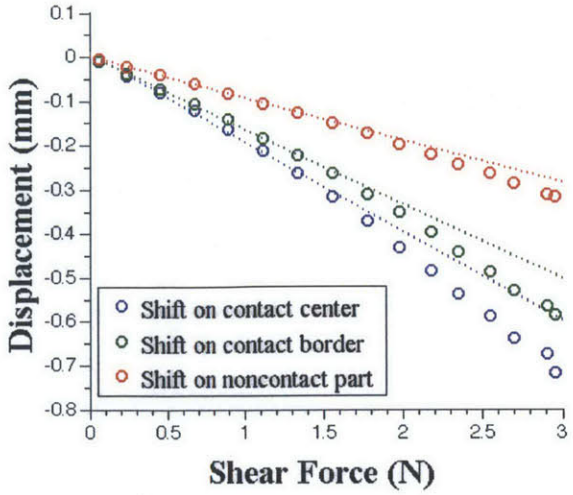

Figure 4-14: The displacement on three positions of the central line under different shear load.

also increases, but the shapes of the figures are very similar, and in a near linear relation. But it can also be seen that when the load is small, the plot within the contact area is very flat, which means the displacement in this area is uniform; when the load increases, the plots in this area are more and more tilted, and when the load is large enough, that the system has come to the incipient slip stage, there is a very obvious peak in the central part of the contact area than the outer parts. This is because during the incipient slip stage, there is partial slip between the indenter and the elastomer, especially in the outer area of contact region, while in the center part the indenter and the elastomer still stick. So for the displacement part the central part has a larger displacement than the outer part. The more likely the indenter is going to slip, the larger the difference is between the central part and the outer parts, which is indicated from the figure as a larger peak in the central area. This is the major indication of incipient slip.

It is more obvious to see the relation between the displacement on the same position for different loads. Figure 4-14 shows the displacements of three different positions on the central line under different shear force. The blue dots are the displacements of the indenting center; the green dots are the displacements of a point very near the contact boundary; and the red dots are the displacements of a point

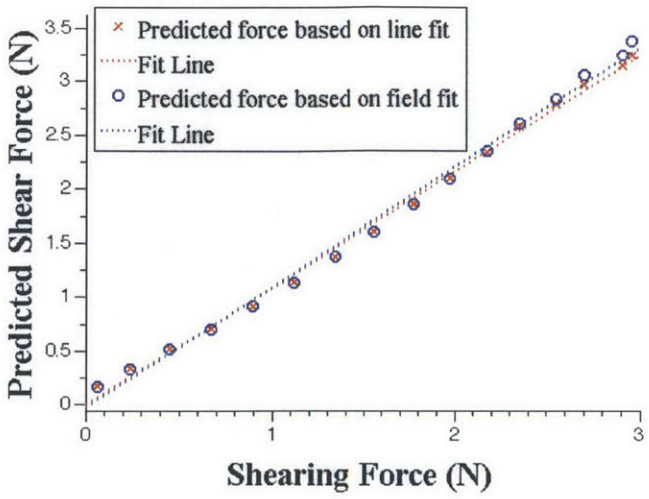

Figure 4-15: Comparison on the predicted force according to match the experimental displacement field to the simulation field and the real force.

on the non-contact area. The dash lines are the linear fitting lines of the data set for the beginning few data. It can be seen when the load is small, all the three data sets are in good linear relation to the load shear forces; with the increase of the load, the non contact area points are still in close linear relation to the shear force, but the two dots in the contact area are more and more deviated to the larger displacement area, and the displacement of the center point has a larger deviation than the outer area points. And this indicates the degree of incipient slip.

The fitting scale of the simulation displacement field to the experimental field can predict the shear force. Figure 4-15 shows the predicted the shear load according to the fitting of the decomposed displacement field and the displacement on the central line separately. From the figure, we can see that the prediction has good linearity, and the two set of predictions are close.

When the load is large, it came to the slip state, that there is some relative displacement between the indenter and the elastomer, and the shear force does not increase with the load displacement increase. Figure 4-16 shows an example of how the shear load force changes with time during slip period. In this experiment, the slip displacement load increased in steps at each time period where there is a distinct step in the shear force, and after a while it came to a quasistatic state. In the figure,

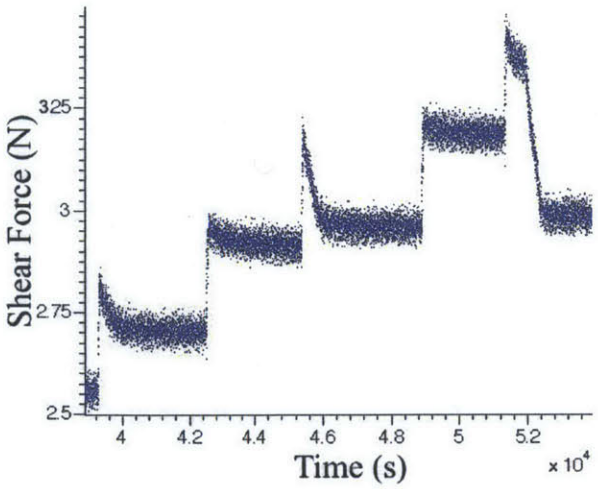

Figure 4-16: The shear force changes on time during slip period.

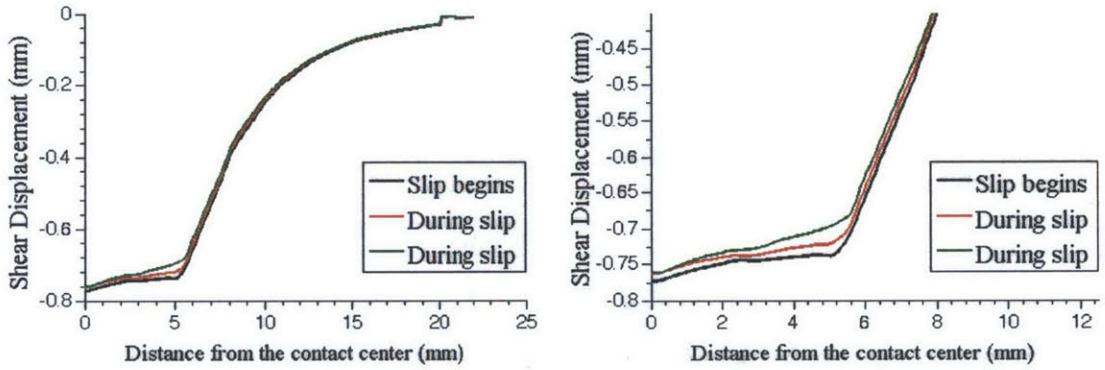

(a) (b)

Figure 4-17: Displacement on the central line during slip.

it can be seen that after the first and the third peak, the shear force decreased largely after the load increase, which is caused by slip.

Figure 4-17 shows the change on the elastomer surface displacement on the central line during slipping. It can be seen that the displacement of the points on the central line has an overall decrease during slip, especially within the contact area.

The experiment also shows that for a given normal load, the limit shear load that for slip beginning is not certain, but is dependent to many factors. Except for the roughness of the contact surface, the loading rate, the humidity and other factors may influence. Generally, it is hard to decide when the contact is going to slip for sure,

but there is a range that can be considered *dangerous* that the slip is most likely to happen. In practical works, like detecting grasp safety for a robot gripper, it is better to set a safe range for incipient slip state that when the state is reached, the grasp is considered as *unsafe* and further insurance procedures are required.

4.5 Conclusion

This chapter introduces both the simulation and experimental results of the indentation with a flat-ended circular indenter on a box-setting GelSight sensor. The indentation load includes the normal load and shear load.

Both the simulation and experiments show that, in a given indentation condition, when the normal load and the shear load are within an acceptable range, the planar displacement field, the load displacement, and the load forces are in linear relation, so that it is able to estimate the load force from the elastomer's surface planar displacement field.

To find the representative scalar of the experimental displacement field, the method of fitting the experimental displacement field with the simulation field is used, and the multiplication factor for the fitting is considered as the factor of the load force. To simplify the field fitting, representatives of the fields according to their geometry properties are selected: for the pressing field, the radical displacements of the sampling points against the distance from the indenting center is selected; for the shear field, two objects are chosen: one is the displacement field decomposition in the shear direction, the other is the displacement on the central line(a straight line starts from the indenting center and along the shear direction). All the representatives work effectively. These experiments showed that the normal and shear load on GelSight sensor can be measured in a given condition.

It also indicates that the linearity property of the displacement field with the load would work for flat-ended indenters with other shapes.

For the shear load, with the load increasing, the contact state changes from shear to incipient slip, and then slip. Shear means that there is no relative movement

between the indenter and the elastomer, slip means there is overall relative movement between the indenter and the elastomer, and incipient slip is the stage that slip is going to happen and there is partial slip between the indenter and the elastomer. Experiments show that partial slip begins from the outer area of the contact surface, and the difference between the displacement of the central area and the outer contact area indicates the degree of the partial slip, as well as the likeliness of slip going to happen.

During the slip period, when the shear indenting displacement increases, the shear force does not increase or even decreases. In the elastomer surface displacement field, it is shown as the relative displacement between the indenter and the surface displacement, and during the slip period the overall displacement of the surface would decrease. However, in practical, it is hard to predict the exactly point that the slip will happen, but only a range that the slip is likely to happen.

Chapter 5

Contact Force Measurement with Other Indenters

In this chapter, indentation experiments with other shapes of indenters on the box-setting GelSight are introduced. The indenter sizes are still small compared to the area of the elastomer, and the elastomer is thick.

5.1 Indentation experiments with sphere indenter

Indentation experiments on a sphere indenter for both normal and shear load are conducted. In the experiments, the setup is the same as introduced in Section 3.3. The elastomer sensor used in this part is the same as in Chapter 4, with the size of 125mm×70mm×4.2mm, and the sphere indenter used here has a diameter of 12.68mm.

In the normal load experiment, the indentation depth is controlled and the normal force is measured by the force/torque sensor attached to the indenter. The load displacement is added in steps, with the step of 0.10mm, and the maximum load is 2.00mm, which is 47.6% of the elastomer thickness. Figure 5-1(a) shows the change of the normal force during the indentation along time. It can be seen that the material also performs strong viscoelasticity, as there are peaks and a decrease after each step load. In the experiment, I still mostly concern the quasistatic state of the indentation.

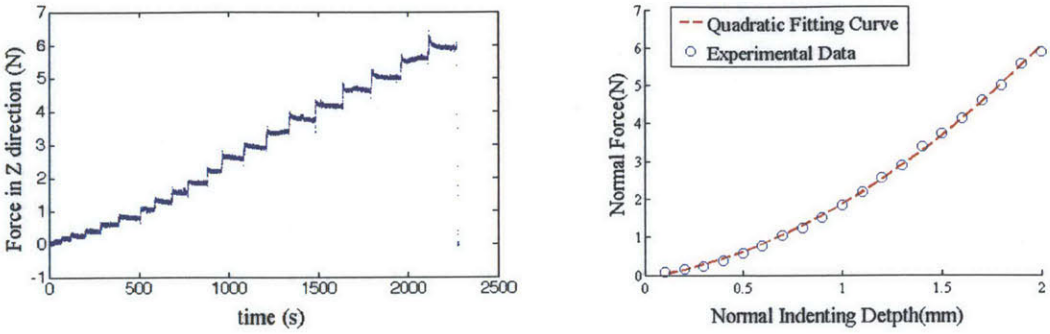

(a) The normal indentation force during the experiment.

(b) The relation of the quasistatic normal load force and the load displacement.

Figure 5-1: The normal force changes during the indentation experiment with the sphere indenter.

The relation of quasistatic normal force and the indentation depth is shown in Figure 5-1(b). Different from the previous experiments with the flat-ended circular indenter, the load and the indentation depth are not in linear relation for a circular indenter. The experimental data generally fits a quadratic curve, as presented in Figure 5-1(b). This is because as the load increases, the contact area also changes for a ball indenter. In this experiment, the contact area is near zero when the load is small, and is of around 43.6mm^2 in the final load.

For the circular flat-ended indenter, the pressure distribution during pressing is high on the border part of the contact and is much lower near the contact center; for the sphere indenter, the pressure is more concentrated on the center point because the pressing depth there is larger. However, the elastomer surface displacement trend to spread outwards too in the sphere indentation. Figure 5-2(a) shows the GelSight's camera view of the indentation and the movement of the markers, and Figure 5-2(b) shows the interpolated displacement field of the elastomer's surface with color vector display. The color vector display expresses the vector on each pixel with the color hue indicating the vector's direction, and the value of the color indicating the magnitude. An example of the standard comparison of the color vector field is shown in the upper-right window of the figure.

Similar to the circular flat-ended pressing results, the displacement field of the sphere normal indentation is also axisymmetric along the indenting center. So the

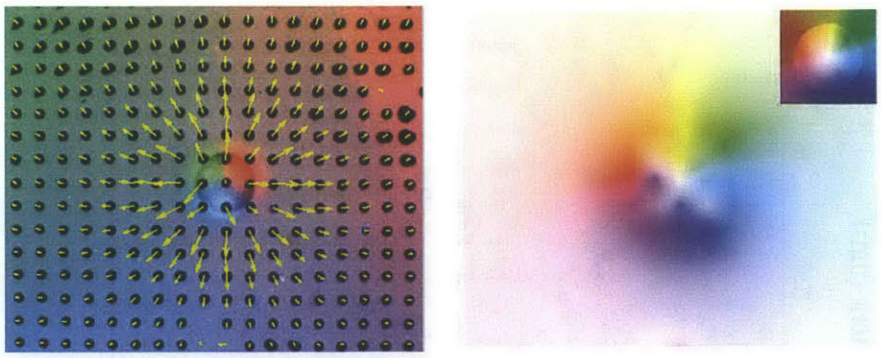

(a) GelSight camera view of the sphere indentation experiment and the movement of the markers on the surface.

(b) The elastomer's surface displacement field shown in color vector. the upper right window is the example of standard vector field.

Figure 5-2: Elastomer surface displacement field during the sphere normal indentation experiment.

displacement field can also be simplified to 1D series of the markers' radial displacements against its distance to the indenting center. Figure 5-3 shows the displacement fields of different normal load in this way. The plots for different load are similar but not strictly linear, as the contact area changes with the increase of the load, and the peak displacement of the plot also became further from the contact center.

In the shear indentation experiments with the ball indenter, the shear load displacement is controlled, and a normal load is applied in advance as there can not be pure shear indentation. During the process, the normal load remains and the shear displacement load increases in steps, until it began to slip. The shear load step is 0.100mm, and the maximum shear load is 1.500mm. The normal load displacement is 1.000mm, with the contact area in the experiment is a circular with the diameter of 5.60mm and the normal force around 2.1N.

The shear force change along the load displacement is shown in Figure 5-4. There are also three stages during the shear load: shear, incipient slip, and slip. When the shear load is small, there is no relative movement on the contact surface and it is in shear state, and the shear force is in a good linear relation to the shear load displacement; even in the incipient slip stage, they are in a close linear relation. When the shear load is too large and the slip begins, the shear force increases much slower.

It is easier to see the relation from the comparison of the indenter's shear displace-

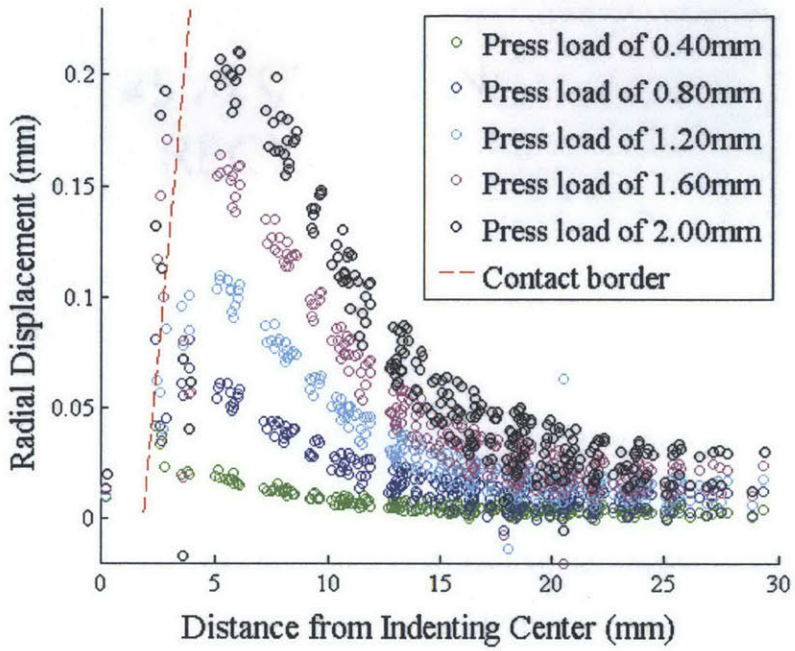

Figure 5-3: The radial displacement of the markers against its distance from the indenting center in the normal indentation experiment, under different normal load.

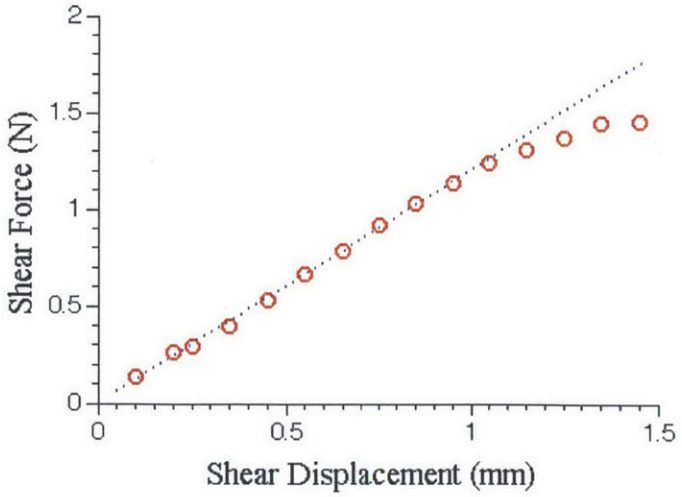

Figure 5-4: The quasistatice shear force and shear load displacement for a ball indentation experiment.

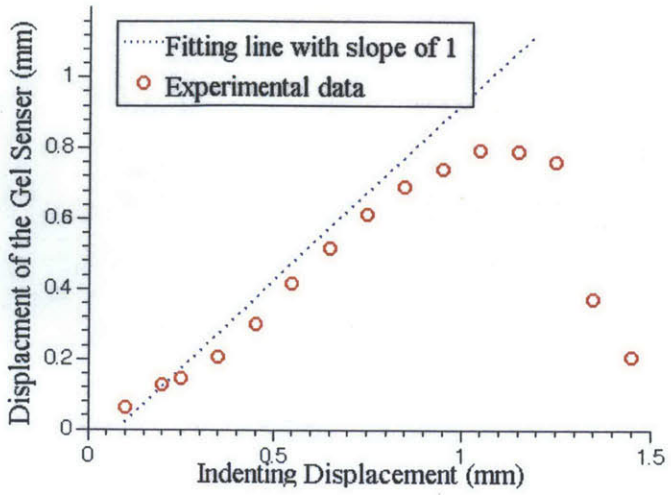

Figure 5-5: The relation between the loading shear displacement and the displacement of the contact center on the elastomer.

ment and the displacement of the contact center on the elastomer. Figure 5-5 shows this relation. The blue dash line in the figure matches the 1:1 relation of the two measure, or that the two equal. It can be seen that at first, the displacement on the contact center generally equals to the displacement of the indenter, and as the load increases the data gradually deviates from the equal relation, to that the elastomer displacement is smaller than the indenter displacement. At last, slip happened, and it is especially obvious on the last three data points that the center displacement on the elastomer drops in large degree.

The displacement field of the elastomer surface during the shear load is shown in Figure 5-6. Figure 5-6(a) shows the camera view from the GelSigh sensor during the indentation, and the motion of the markers on the elastomer surface. Similar to the displacement field of the flat-ended circular indenter, the displacement field of pure shear is mainly in the shear direction. Figure 5-6(b) shows the pure displacement magnitude in the shear direction. The shear direction displacement field is axisymmetric along x and y axis, and its shape is very similar to the one of the circular flat-ended indentations: within the contact area the displacement is the largest and uniform, and outside the contact area, the contour shape of the displacement magnitude is similar to a transverse 8 shape, with the smallest gradient on the shear

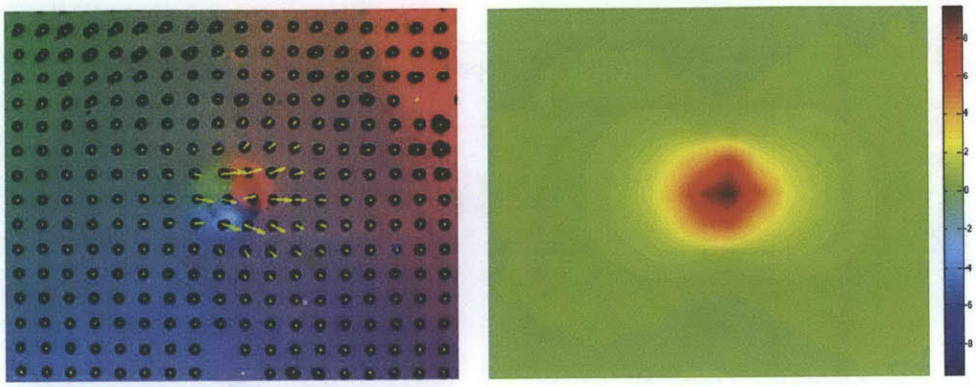

(a) The GelSight camera view for the ball indenter shear and the displacement of the markers

(b) The displacement field on the shear direction during the shear indentation experiment

Figure 5-6: Displacement field of shear indentation of a ball indenter.

direction. So we can also draw a central line from the contact center on the shear direction, and compares the displacement on the line.

Figure 5-7 shows the displacement on the central line under different shear load during the shear and incipient slip period. The figure shows that as the load increases, the overall displacement increases accordingly, and the difference between the central part displacement and the outer area displacement became larger and larger, as partial slip happens in the outer area of the contact. This is the indication of the incipient likeliness to slip. Figure 5-8 shows the comparison of three different position's displacement on the central line under different shear load force. Three dot sets represent the displacement on the contact center, the displacement on the border of the contact area, and the displacement of a point away from the contact area. The dash lines are the linear fitting lines of the load data. The figure shows that before slipping, the displacement without contact area is always in good linear relation with the shear load force, and so did the points within the contact area when the load is small. As the load increases, the displacement of the center point deviates to the larger half, and the deviation grows larger and larger.

For both the sphere indenter and the flat-ended indenter, the partial slip happens from the border part of the contact area. But for flat-end indenters, the contact pressure is concentrated on the border part, so it is relatively harder for slip to

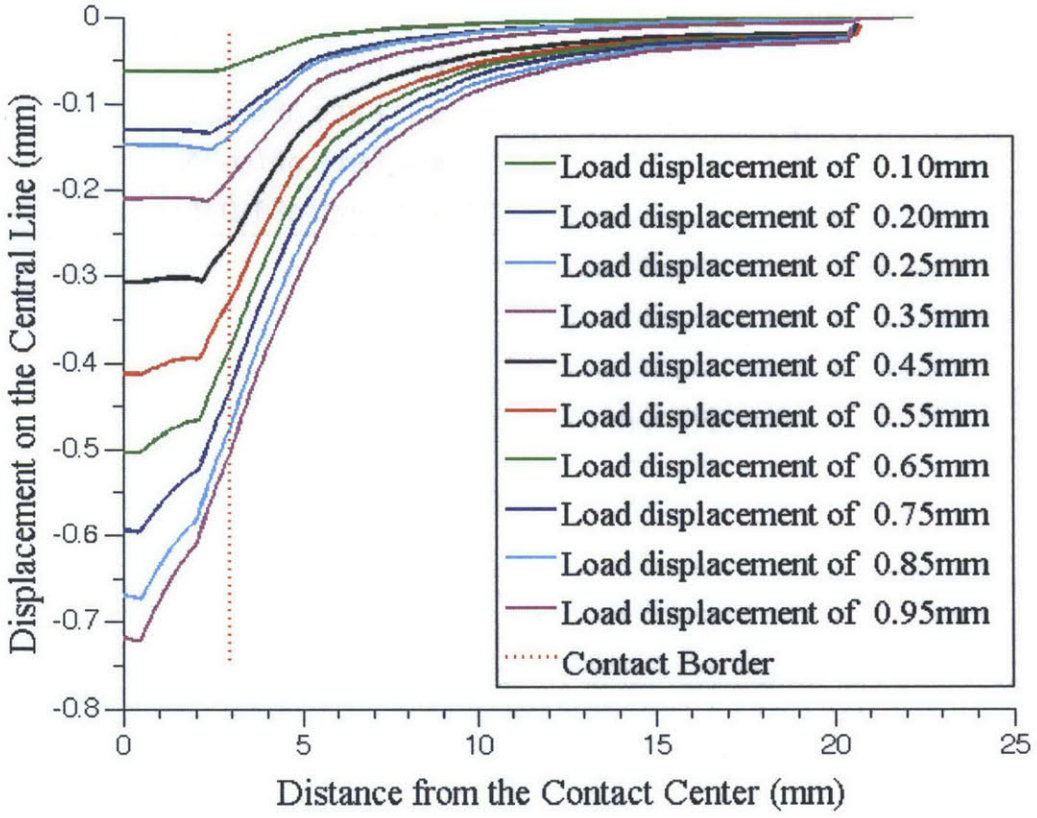

Figure 5-7: Displacement on the central line under different shear loads.

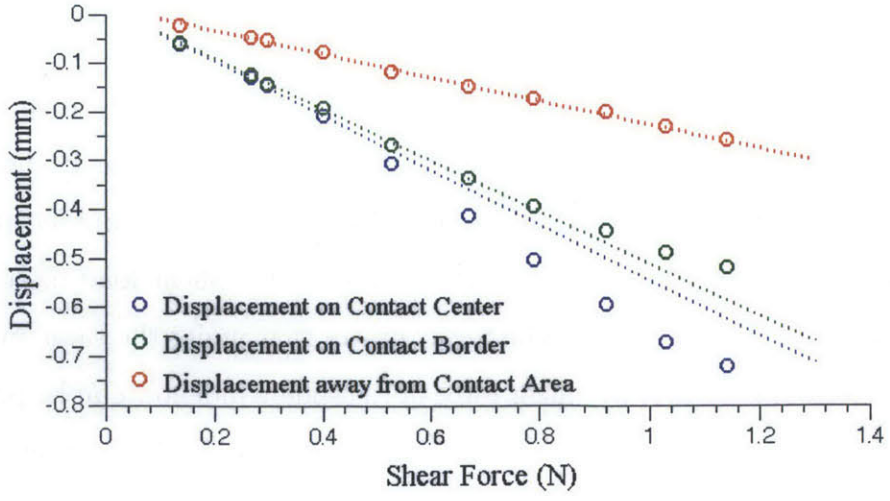

Figure 5-8: Comparison on the displacement under different shear load on different positions.

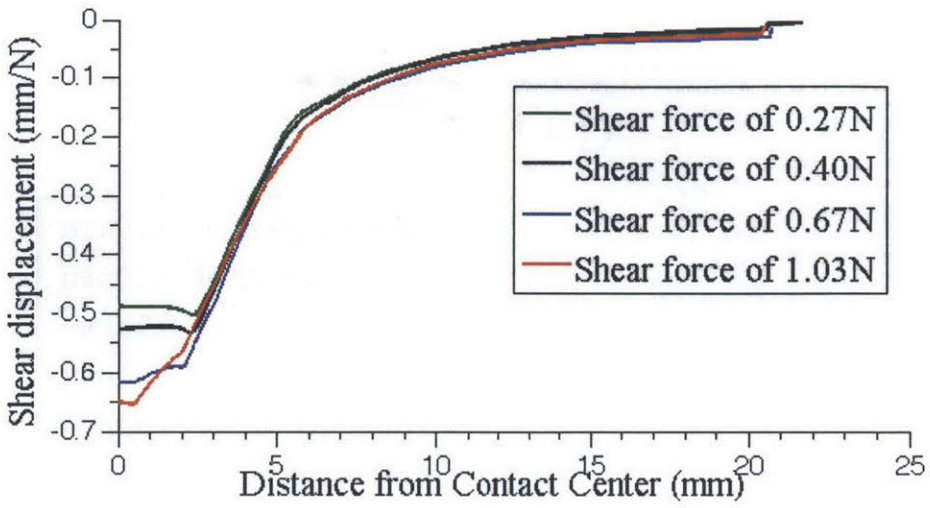

Figure 5-9: Scaling the displacement on the central line under different shear load.

happen on the border area; for sphere indenters, the pressure in the center area is high and very low in the border area, as the vertical displacement of the border area is very low, so it is very easy for partial slip to happen in the border area, but harder in the central area. In this case, compared to the flat-ended indenters, the contact with sphere indenter has a much larger tolerance in the difference of the central displacement and boundary displacement, and a larger range for detecting incipient slip.

However, if only considering the displacement outside the contact area, the curve of the displacement on the central line is of good linear relation to the shear load force. Figure 5-9 shows an example. In the figure, four central line displacement curve under different load force is drawn and scaled by the load force. It shows that outside the contact area, the scaled curves fit perfectly; within the contact area, the relative displacement on the shear direction increases as the shear load increases, as well as the displacement differences. The result proves that under the same indenting condition and normal pressure, the shear force of the sphere indenter can be predicted according to fitting the displacement on the central line outside the contact area.

Figure 5-10 shows the change in the central line displacement during the slip process. As is shown, the most distinct change is the sudden drop of the center displacement. So generally as the shear load increases, partial slip happens in the

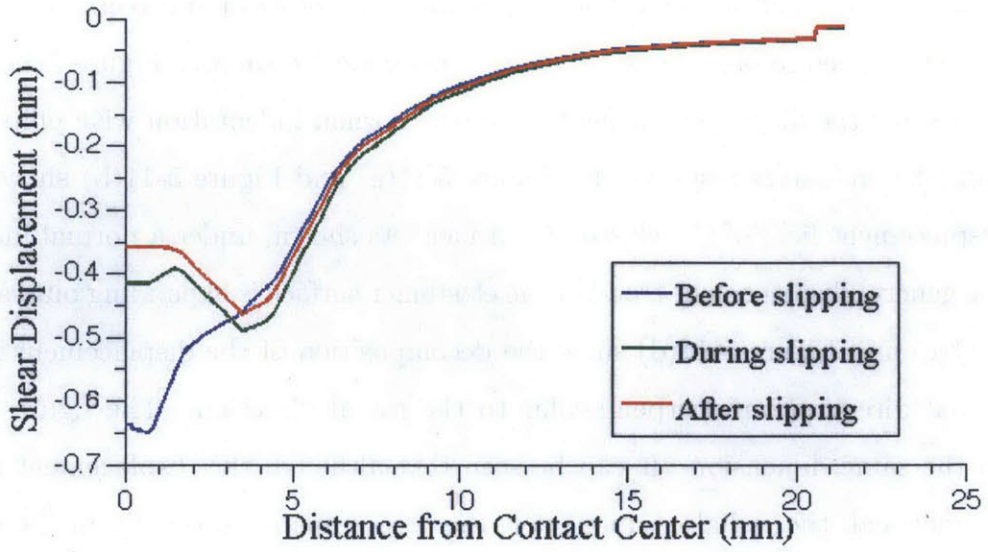

Figure 5-10: The change of the displacement on the central line during a slip process.

border area, and the elastomer in the contact area gradually stretches, until it finally reaches the point that the center part begins to slip, and the elastomer surface shrinks rapidly.

5.2 Indentation Experiments with Flat-ended Elliptical and Rectangular Indenters

Indentation experiments with elliptical and rectangular shaped flat-ended indenters are also conducted. The indenters' sizes are also small compared to the elastomer size, and the contact areas do not change during the indentation. The experimental results also show the linear relation between the force load and load displacement. However, as the transection of the indenter is not axisymmetric, the response displacement field is not symmetric as well.

The reasons for choosing elliptical and rectangular indenters are that the two shapes are both long on one dimension and short in the other dimension. Ellipse is an example of with smooth boundaries and different curvatures, and rectangular is an example of the indenters that have straight borders and sharp corners.

Simulation on the normal load indentation with the elliptical and rectangular indenters are conducted in order to get the elastomer's ideal response. Figure 5-11 and Figure 5-12 show the displacement field under the normal indentation with elliptical and rectangular indenters respectively. Figure 5-11(a) and Figure 5-11(b) show the overall displacement field of the elastomer surface. As shown, under a normal indentation, the general displacement trend of the elastomer surface is expanding outwards. Figure 5-11(c) and Figure 5-11(d) show the decomposition of the displacement field on the redial direction and perpendicular to the radial direction. The figures are drawn on the same dimension. It can be seen that although the displacement field is not symmetrical, the radial component is the predominant, especially in the area that is not very close to the contact part. When it is not close to the contact area, the displacement field tends to distribute in a symmetric way.

Figure 5-12(c) and Figure 5-12(d) show that this regulation also works for the rectangular indenter.

For the displacement magnitude, although the pressure is more concentrated on the pointed side, the flatter sides mostly have the higher peak in the magnitude off the contact area, and the peak there is further from the contact border.

The simulation also shows that, similar to the circular flat-ended indenter's case, the pressure distribution for the elliptical or rectangular indenters is higher on the border part of the contact area. But the pointer ends, which mean the small curve sides of the ellipse, and the shorter sides of the rectangular and the corners, have a larger pressure. This stress concentration also results in some deviation of the displacement field close to the contact border. Figure 5-13(a) and Figure 5-13(b) show the displacements near the pointed end of the indenters. It can be seen that the displacement field tends to *flow* to the pointed end side while expanding, but it tends to be along the radial direction further to the contact area.

Figure 5-14 shows the experimental data of the indentation of the elliptical indenter and the rectangular indenter. In the figure, the first column of the figures shows the vector field of the markers, and the background in the image is the difference between the GelSight camera image under the indentation and the one of not touch-

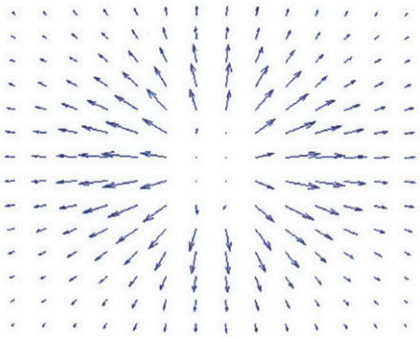

(a) The vector displacement field.

(b) The color vector display of the displacement field.

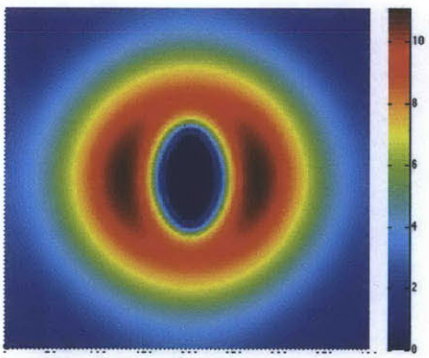

(c) The magnitude of the displacement on radial direction.

(d) The magnitude of the displacement perpendicular to radial direction.

Figure 5-11: Simulated displacement field for normal indentation of a elliptical flat-end indenter.

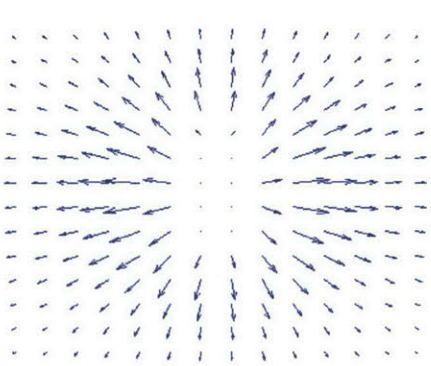

(a) The vector displacement field.

(b) The color vector display of the displacement field.

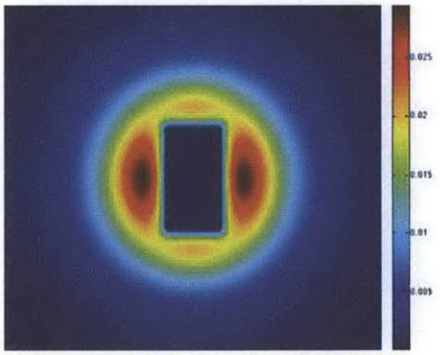

(c) The magnitude of the displacement on radial direction.

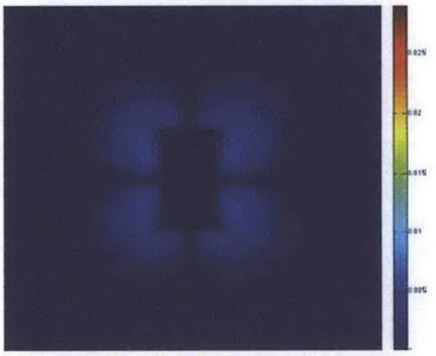

(d) The magnitude of the displacement perpendicular to radial direction.

Figure 5-12: Simulated displacement field for normal indentation of a rectangular flat-ended indenter.

(a) The displacement field near the elliptical indenter.

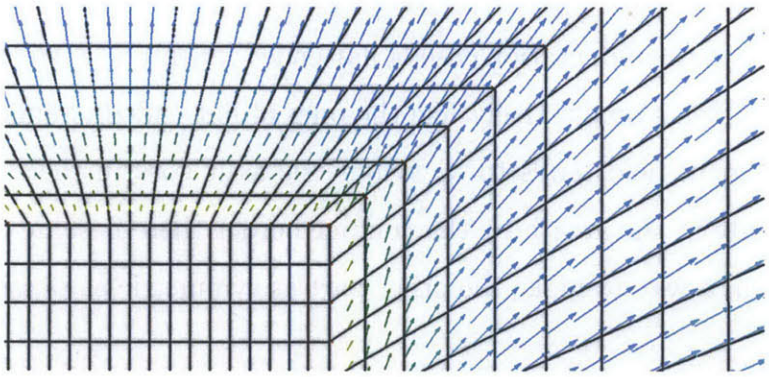

(b) The displacement field near the rectangular indenter.

Figure 5-13: The displacement field of the elastomer surface near the contact area.

ing anything; the second column show the interpolated displacement field of the how surface in color vector display method; the third column shows the contour map of the displacement magnitude. It can be seen that the experimental data is very similar to the simulation data, in that the displacement field is mostly in the direction that is outwards from the indenting center, and axisymmetric when not near the contact area.

Experiments of the shear indentation with the two indenters are also conducted, and example results are shown in Figure 5-15. The figure shows both the overall displacement field and decomposition of the pure shear field (with the field of normal indentation subtracted). The results show that, regardless of the indenter's size and shear direction, the pure shear field is very similar to the field of that on the circular flat-ended indenter, at least in the area not close to the contact part. In the decomposition, the displacement magnitude perpendicular to the shear direction is very small, and the magnitude component on the shear direction is predominant. In this part, the field is in the shape of a transverse "8".

In conclusion, in the indentation case of flat-ended indenters, both the normal and shear indentation fields qualitatively like the ones of flat-ended circular indentation, and the displacement field tends to be symmetric as it goes further away from the contact area. Only in the area near the contact border there is some deviation, and the deviation is in a way to make the other part as symmetric as possible.

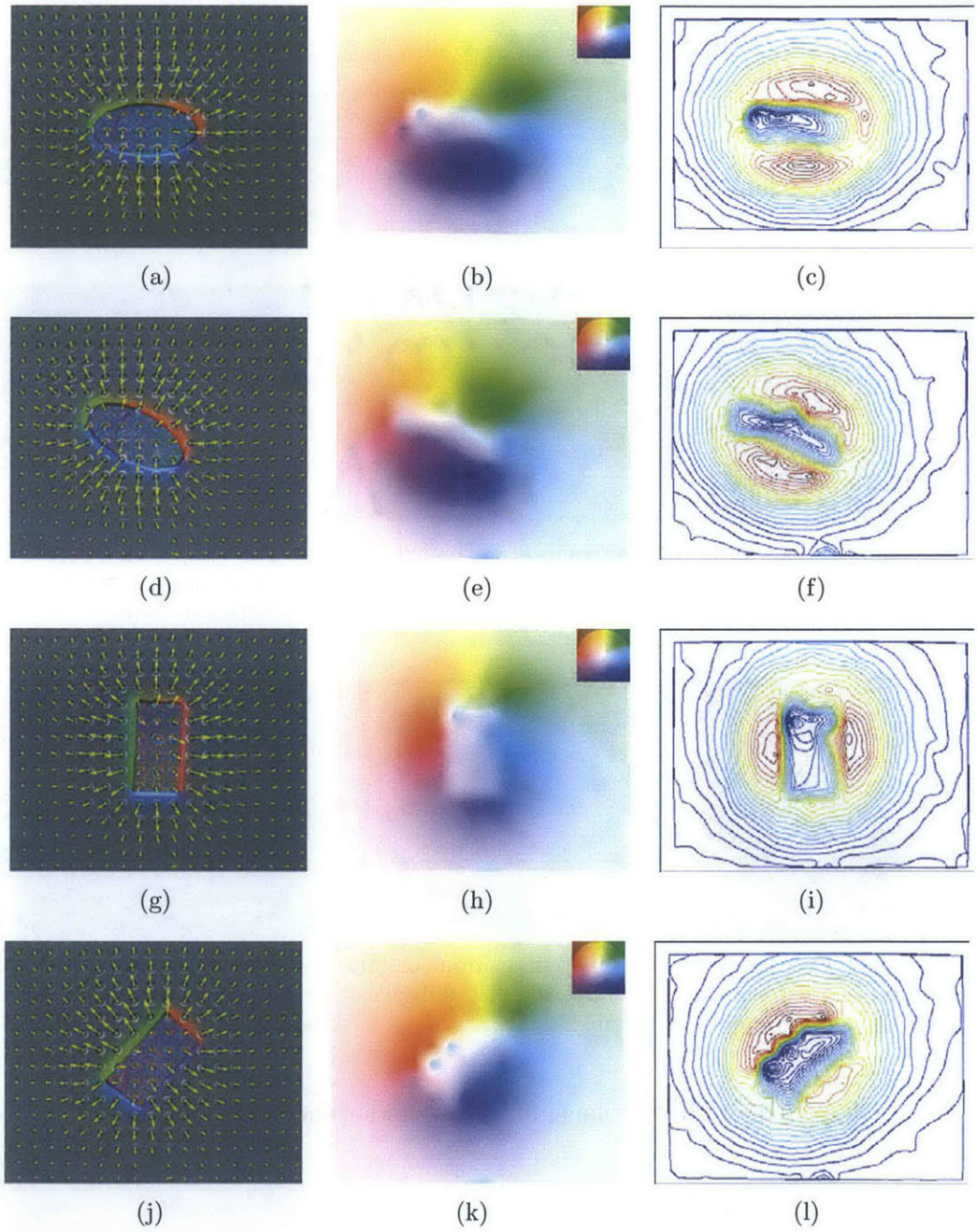

Figure 5-14: The experimental displacement fields for indentation of the elliptical indenter and the rectangular indenter. The first column shows the arrow field, the second column shows the vector field, and the third column shows the contour map of the displacement magnitude.

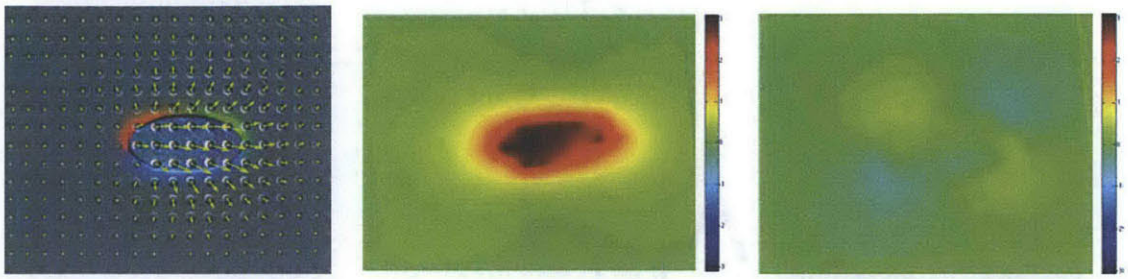

(a) The sum displacement field of the markers under shear load of the elliptical indenter.

(b) The composition on the shear direction of the displacement field.

(c) The composition perpendicular to the shear direction of the displacement field.

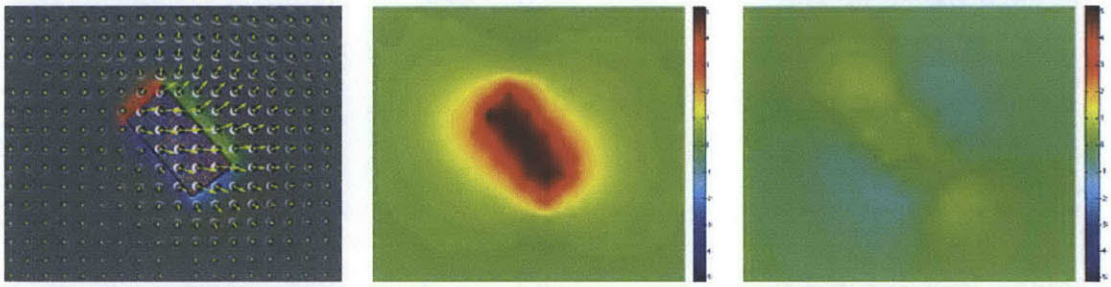

(d) The sum displacement field of the markers under shear load of the rectangular indenter.

(e) The composition on the shear direction of the displacement field.

(f) The composition perpendicular to the shear direction of the displacement field.

Figure 5-15: The displacement field under shear indentation.

Chapter 6

Force Measure with Portable GelSight Device

6.1 The Portable GelSight Device

In this section, some force measure experiments with the portable GelSight device are introduced. The portable GelSight device is the smallest GelSight design, and the structure is shown in Figure 6-1. The elastomer used on the sensor is of size 2.5mm×2.5mm, with the thickness thinner than 2mm. The sensor can be used on a robotic gripper to obtain the tactile information during manipulation, and can be mounted on human fingertips to see what human feel when doing some common jobs. The examples are shown in Figure 6-2. Further introduction on the sensor design is in [20].

In the experiments, a specially designed GelSight device with alignment holes to mount it on modular structures is applied.

For contact forces measurement, the challenge for the portable GelSight device is that the elastomer is much thinner and smaller than the previous case, and the contact area of the object is very large compared to the camera view. Additionally, the camera used for portable GelSight is a web camera, whose quality is much inferior. So the data got by the portable device has much larger measure error. Additionally, as the camera view is small, mostly we can only get partial contact information of

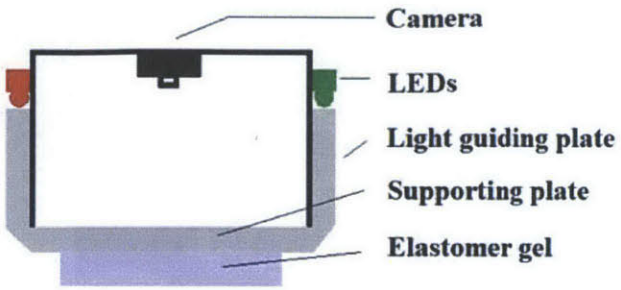

(a) The structure scheme of portable GelSight Design.[20]

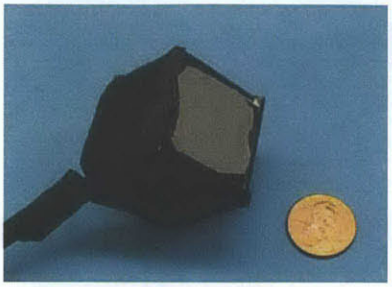

(b) A hand-hold prototype of portable GelSight.

Figure 6-1: The portable GelSight device

(a)

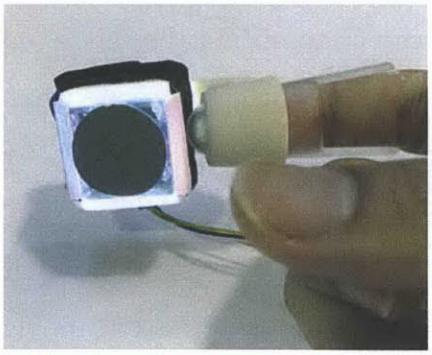

(b)

Figure 6-2: The portable GelSight device mounted on a robot gripper and on a human finger.

the contact area. So the theoretical analysis of the elastomer has more challenges for the portable device, and experiments are more important for real conditions.

6.2 Indentation Experiments with the Portable Device

In this section, experiments on circular flat-ended indentation on the portable GelSight device are conducted. The overall setup is shown in Figure 6-3: the indenter is mounted on a 2 DOF stage which can move in horizontal and vertical directions respectively, with a high-resolution screw micrometer to record the moving distance. So by moving the stage the indenter can load on either normal direction or shear direction. There is a 6-axis force/torque sensor connecting the indenter and the moving stage, which measures the loading forces and torques. This indenting part of setup is introduced in Section 3.3.

The GelSight sensor is shown in Figure 6-3, with yellow base, black wall, and the light top part. The sensor is mounted on a tripod below the indenter. The mounting head of the tripod is connected to the supporting legs through a ball joint, so that the planar direction of the GelSight sensor can be adjusted, and making the indenter perpendicular to the sensor surface. There is also a planar rotating joint with scale on the tripod, so that the GelSight device can rotate to certain angles along the normal axis, thus exert some torque in normal direction.

In this part, three indentation experiments are conducted, and the elastomer's response to normal indentation, shear indentation, and rotating indentation are studied respectively. The elastomer's size is 22.6mm×23.4mm×2.0mm (close to 1 inch square), and it has triangle markers spread on the surface in random ways. The average distance between two adjacent markers is around 2mm, and the linear length of one marker is about 0.7mm. The indenter is a flat-ended circular indenter, with the diameter of 12.5mm (close to 0.5 inch). The indenter is made of acrylic, which is considered rigid compared to the elastomer, and the contact surface is smooth with

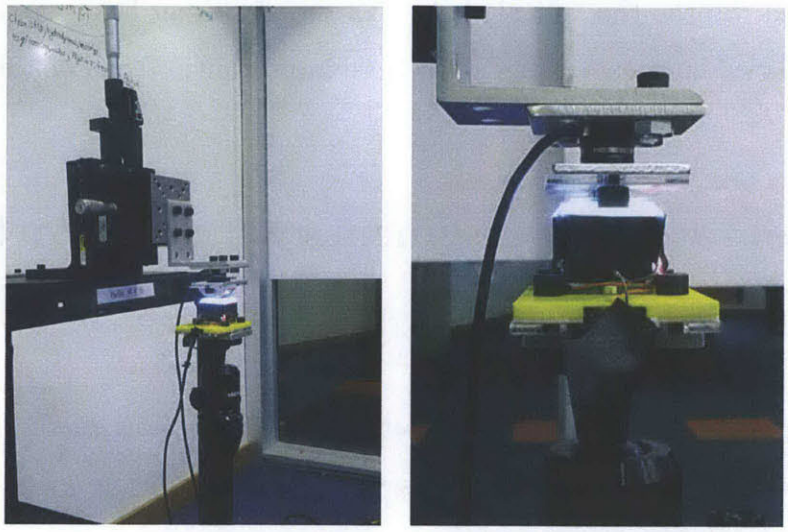

(a) (b)

Figure 6-3: The experimental setup for measuring indenting forces and torques for the portable GelSight device.

little partial fluctuation.

In the indentation experiments, we still mainly consider the elastomer's response in the quasistatic situation, which is usually achieved after 1 or 2 minutes in the increasing load condition.

6.2.1 Experimental results of normal indentation

In the normal indentation experiments, the flat-ended circular indenter is pressed perpendicular to the sensor elastomer's surface. The indentation depth is controlled by the stage, and the indenting force is measured by the force/torque sensor. The load is exerted in a step increasing mode, and the maximum load displacement is 0.600mm, which is 30% to the thickness of the elastomer. The step increase is 0.100mm. I also tested the unloading process during the experiment.

The normal force change during the experiment is shown in Figure 6-4(a). The figure shows the force change for both loading and unloading process of the indentation. The figure also shows that the elastomer performs severe viscoelasticity, as there is a sharp peak after each load increase, and slowly decreased to a stable state. Figure 6-4(b) shows the magnified view of the force change during one load.

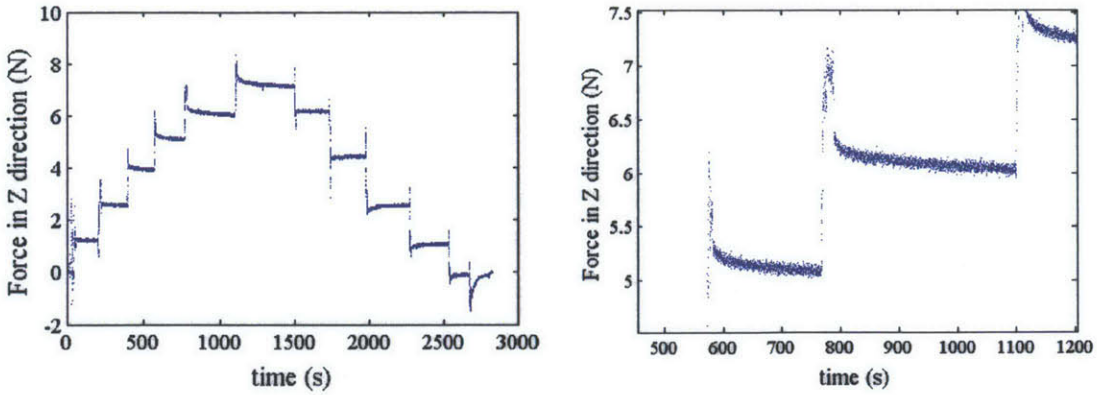

(a) (b)

Figure 6-4: The loading normal force changes in the experiments.

Figure 6-5 shows the relation between the indenting force and the loading depth. The blue plot is the force change during the loading, and the magenta plot is the force during the unloading. The dash lines are the fitting lines to the two data sets based on the first few samples. The figure shows that, in the unidirectional loading or unloading process, the normal load force and the normal load depth are in good linear relationship. For the loading process, when the load is large, the data trend to deviate from the linear relation. But the unloading forces are much smaller than the loading forces as shown in the figure. That is because for the thin elastomer, the residue force has large influence on the later loading, and it takes long time to recover from the deformation.

Figure 6-6 shows the displacement field of the elastomer surface under different normal load. The displacement magnitude is in positive correlation to the load force. The displacement field is in a radiating pattern from a certain center in the contact area, but the radiating center is not necessarily the indenting center. Because of the tiny imbalance during the indenting, the radiating center of the displacement field is not the indenting center. Along an arbitrary direction from the radiating center, the displacement magnitude firstly increases and then decrease, and the max displacement area is within the contact area. The displacement magnitude of un-contact area is smaller than the contact area, but the difference is not distinct.

Figure 6-7 shows the colormap of the displacement magnitude corresponds to

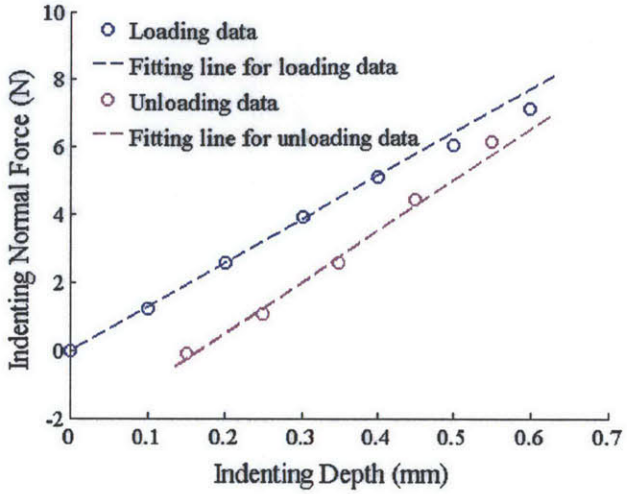

Figure 6-5: The relation between the load normal force and load displacement in both loading and unloading cases.

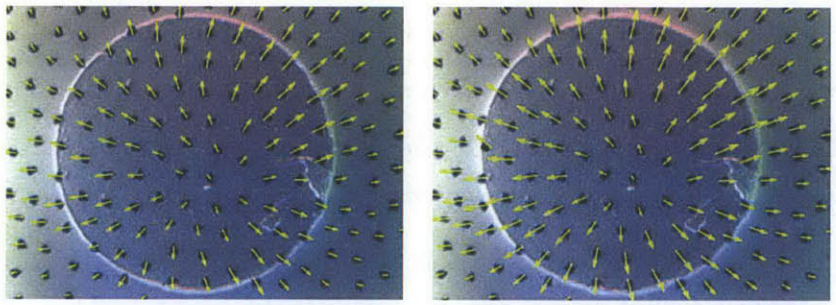

(a) Load normal displacement of 0.250mm

(b) Load normal displacement of 0.350mm

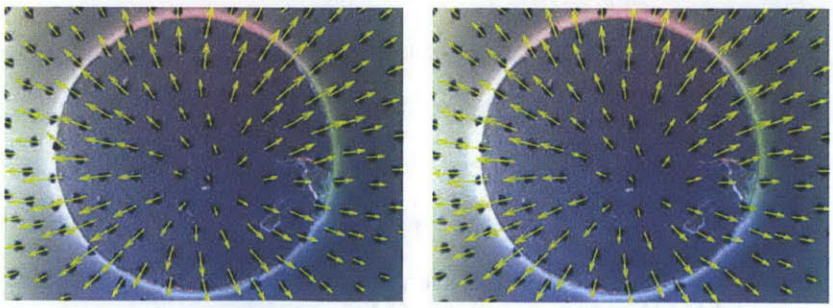

(c) Load normal displacement of 0.450mm

(d) Load normal displacement of 0.550mm

Figure 6-6: The camera view of GelSight sensor and the motion vectors of the markers under different normal load.

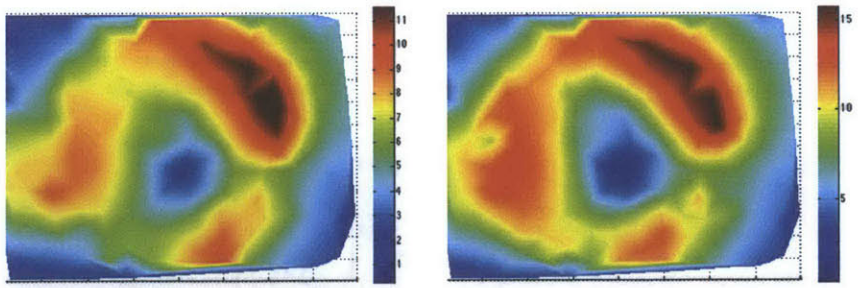

(a) Load normal displacement of 0.250mm

(b) Load normal displacement of 0.350mm

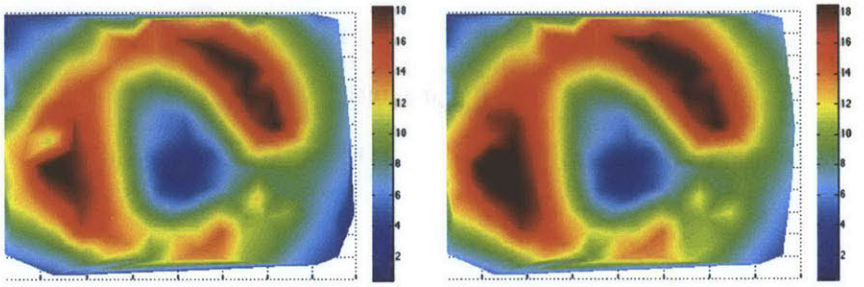

(c) Load normal displacement of 0.450mm

(d) Load normal displacement of 0.550mm

Figure 6-7: The displacement magnitude map under different normal load.

the four cases presented in Figure 6-6. The figure also shows that the displacement magnitude is in a general radiating pattern, but not ideally, which may be caused by some experimental errors. And there is no obvious difference in the displacement magnitude field between the contact area and the un-contact area.

Figure 6-8 shows the displacement magnitude change during both the loading and unloading process. Figure 6-8(a) shows the relation of the displacement to the load depth, and Figure 6-8(b) shows the relation of the displacement with the normal force. Both figures show the average displacement of all the markers (shown in blue color) and the max magnitude of all the markers (shown in red color). The dash line represents the loading order, in the counterclockwise order. The lower half is the loading curve, and the upper half is the unload curve. It can be seen that for the normal load, the elastomer's surface displacement has severe hysteresis effects.

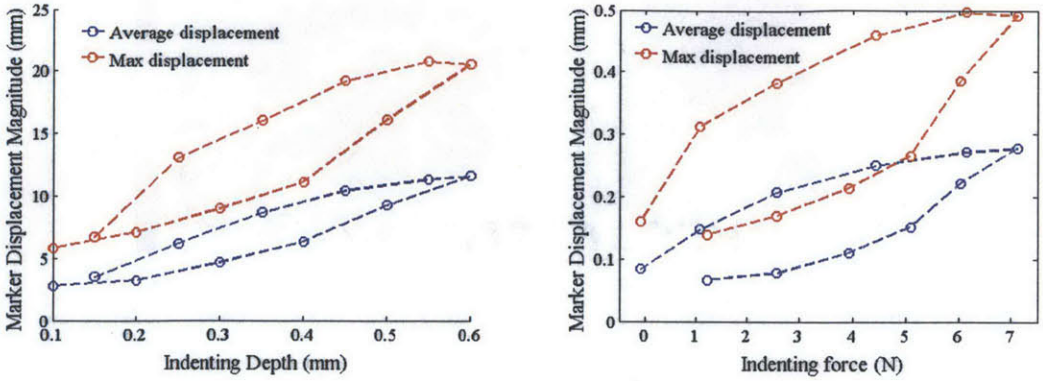

(a) The relation of the marker displacement magnitude and the indentation depth

(b) The relation of the marker displacement magnitude and the normal force

Figure 6-8: The marker displacement magnitude changes in normal indentation experiments.

6.2.2 Experimental results of shear indentation

In the shear indentation experiment, the shear displacement is controlled by the stage with screw micrometer, and the shear force is measured by the force/torque sensor mounted on the indenter. The motion precision of the horizontal stage is 0.02mm. The maximum shear displacement load in the experiment is 0.600mm, and the load increases in steps. Similarly it is only the quasistatic state of the elastomer's response is considered in the experiment, thus after each load increase I waited around 3 minutes until the elastomer reaches a general steady state.

Figure 6-9(a) shows the change of shear force along time during the experiment, and Figure 6-9(b) shows the relation of the quasistatic shear force and the load shear displacement. As shown in Figure 6-9(a), the shear force is not stable after the 2nd load increase, that there is always a jump in the resultant shear force from the very beginning. That means the indenting is not stable and partial slip happens even when the load is small. However, as shown in Figure 6-9(b), the quasistatic relation between the load shear force and the load displacement of the indenter is quite linear.

Figure 6-10 shows the vector field of the GelSight elastomer surface and the camera view of the sensor under different shear load. The lengths of the arrows are correlated with the displacement magnitude of the elastomer. The figure shows that,

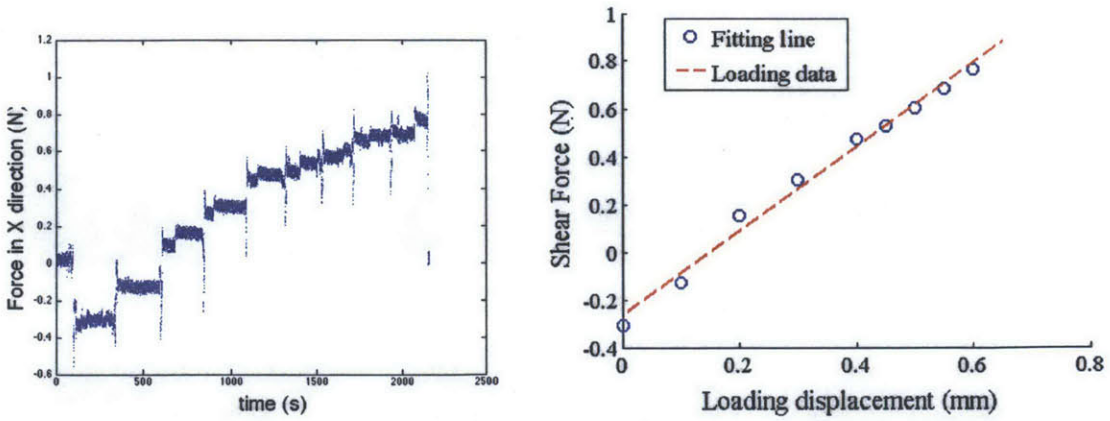

(a) The measured shear force as time changes. (b) The relation of shear force and shear displacement in quasistatic cases.

Figure 6-9: The loading shear force changes in the experiments.

the displacement in the contact area is much larger than the one in the non contact area, and is generally all aligned to the shear direction. In the non contact area, the displacement field is very similar in shape to the ones described in Section 4.4.

However, scrutinization into the displacement fields shows that, when the shear load is small, the displacement in the contact area is uniform and all along the shear direction; as the load increases, the displacement differences within the contact area grow, that in the bottom half part in the image the displacement is larger than the upper half part, and there is a trend to deviate to the spreading direction for the displacement field.

A more explicit way to display the difference is to compare the displacement magnitude of the whole field. Figure 6-11 shows the colormap of the displacement magnitude. From this figure, it can be seen that the displacement of the contact area is the major displacement, and as the shear load increases, the area difference grows more obvious. This indicates that partial slip happened in the less displaced area.

It can be also summarized that the largest displaced area, or the place that the partial slip is least likely to happen, is on the part of the area that to the shear direction. In other words, the shear direction in this experiment is to the bottom side of the camera view, and so does the major displacement direction shown in Figure 6-10. As a result, in the bottom part of the contact area, the displacement is always

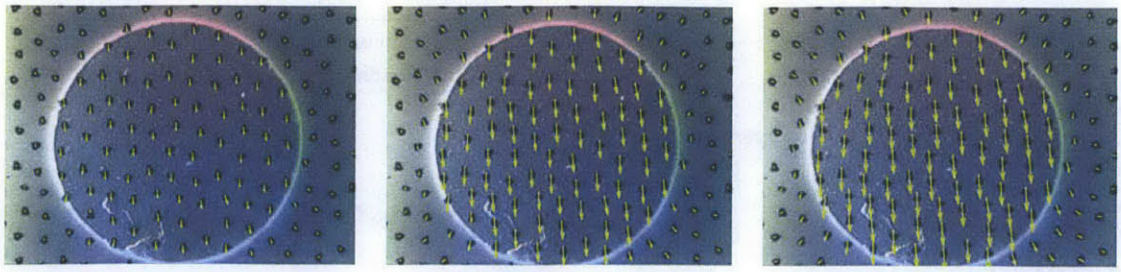

(a) Load shear displacement of 0.100mm (b) Load shear displacement of 0.300mm (c) Load shear displacement of 0.400mm

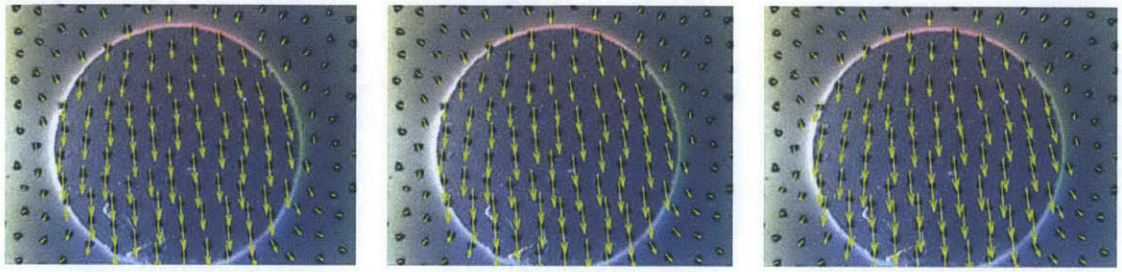

(d) Load shear displacement of 0.500mm (e) Load shear displacement of 0.550mm (f) Load shear displacement of 0.600mm

Figure 6-10: The camera view of GelSight sensor and the motion vectors of the markers under different rotating load.

the largest.

Figure 6-12 shows the relation between the displacement of a marker within the max displacement area, and the load displacement. Theoretically, if there is no slip in that area, the two should be equal and the blue dots in the figure match the red line, where x=y. But the experimental data shows that although the marker's displacement is of good linearity with the increase of the load, the data is lower than the theoretical value. That may be caused by the experimental errors, or there is always some overall slip between the indenter and the elastomer. The most likely explanation is that the slip contributes the majorly.

Figure 6-13 shows the relation of displacement of different markers in the experiment. Three samplings are chosen: the one marker within the max displacement area(shown in dark blue color), one marker in the partial slip area(shown in cyan color), and the average displacement magnitude of the whole camera view(shown in red). The x-axes are on the load shear displacement and shear force respectively, but as the two are of linear relationship, the two figures are very similar in shape. The

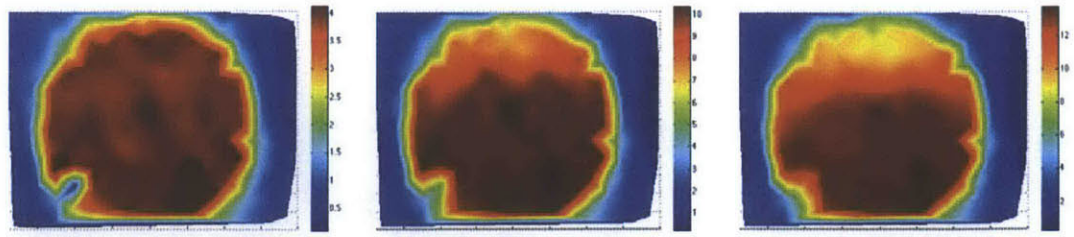

(a) Load shear displacement of 0.100mm (b) Load shear displacement of 0.300mm (c) Load shear displacement of 0.400mm

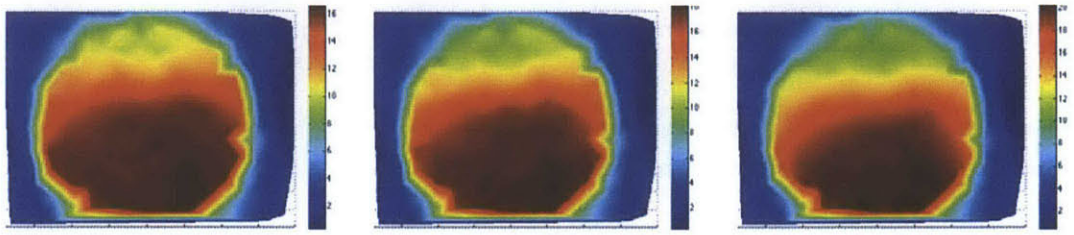

(d) Load shear displacement of 0.500mm (e) Load shear displacement of 0.550mm (f) Load shear displacement of 0.600mm

Figure 6-11: The displacement magnitude map under different shear load.

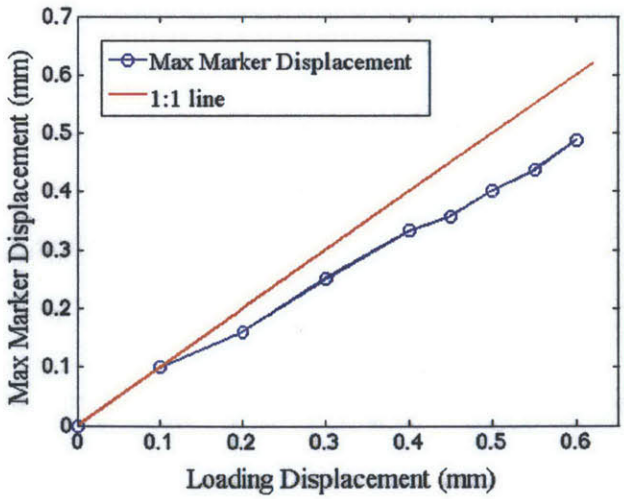

Figure 6-12: Relation between the displacement of the max displaced marker and the load shear displacement.

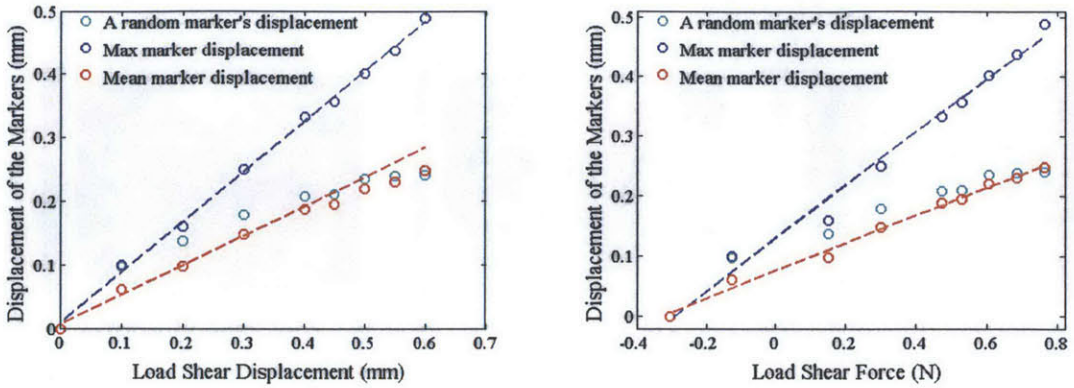

(a) Comparison of the marker displacements under different loading displacement.

(b) Comparison of the marker displacements under different loading shear force.

Figure 6-13: Comparison of the max marker displacements, average marker displacement, and the displacement of a marker in the partial slip area.

max marker displacement and the average displacement is of good linear relation to the x-axes, so fitting line is also drawn for the two sets of data.

Similar to what is shown in Figure 6-11, the plots here indicate that when the load is small, the displacement magnitude of the markers in the likely-to-slip area is very close to that of the marker in the unlikely-to-slip area, while the latter one is in good linear relationship to either the load displacement or the shear force. But as the load increases, the difference between the two grows larger, which indicates the partial slip in the contact condition is more and more severe. And similar to the experiments in Section 4.4, the difference between the displacement of two areas within the contact part indicates how likely the slip is going to happen.

The average displacement here, is smaller than even the one of the likely-to-slip marker at the beginning, because the influence of the markers outside the contact area is also concluded here, which is much smaller than the displacement within the contact area. The difference between the average displacement and the max displacement marker also trends to be larger and larger according to the increase in the shear load.

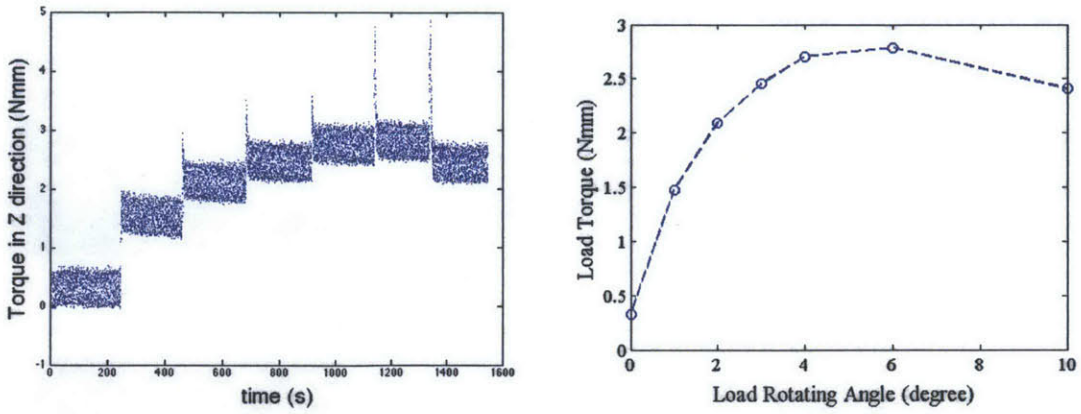

(a) The measured torque as time changes.

(b) The relation of loading torque and load angle in quasistatic cases.

Figure 6-14: The loading torque changes in the experiments.

6.2.3 Experimental results of indentation with rotation

In the rotation indentation experiment, the loading angle is controlled by the tripod joint, and the loading torque is measured by the force/torque sensor on the indenter. Firstly, a normal indenting load is applied, and then the GelSight sensor rotates to different angles. However, the angle scale on the tripod is of low resolution, while the elastomer's response to rotating load is very sensitive, that when the loading angle grows to 3 degrees, obvious slip begins to happen between the indenter and the elastomer. The angle loading precision is about 1 degree. The loading torque's change with time during the experiment is shown in Figure 6-14(a), and the quasistatic relation between the loading angle and loading torque is shown in Figure 6-14(b).

It should be noticed that the small decrease in the loading torque as the load angle increases in the end parts is mostly resulted from experimental error. The experimental setup itself is not precise, and the camera's optical axis is not aligned with the sensor's central axis, so the rotating center is not to the sensor center. The small eccentricity in the setup enlarges the error during the rotation. Actually, as the load angle increases in the experiments, the normal load force decrease and the shear force increases. So the quantity deviation of the experiment is large.

The displacement field of the elastomer surface under different rotating load is shown in Figure 6-15. The vector field of normal pressing is subtracted, and the

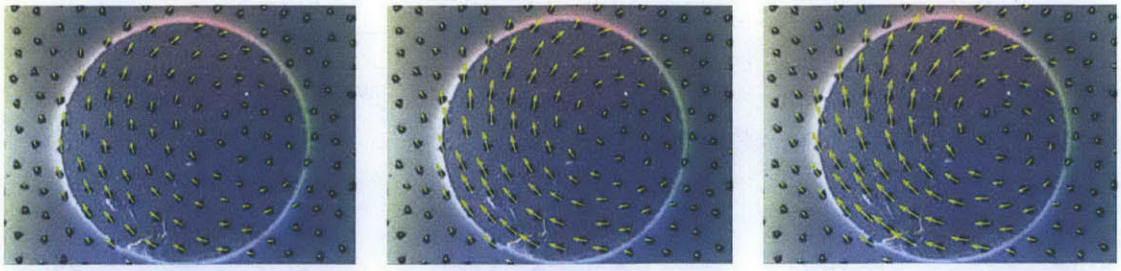

(a) Load rotation angle of 1 degree (b) Load rotation angle of 2 degree (c) Load rotation angle of 3 degree

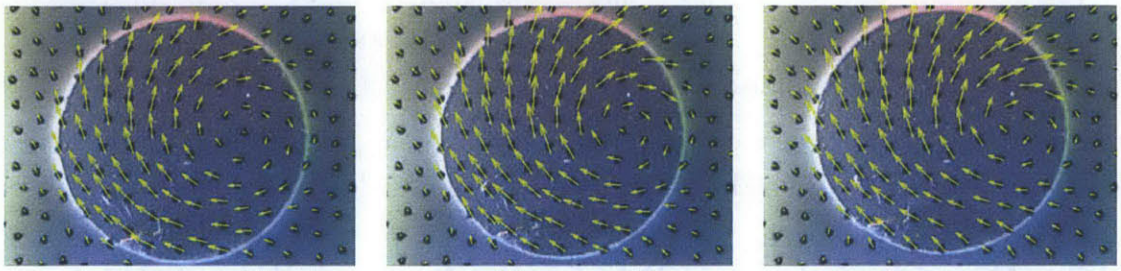

(d) Load rotation angle of 4 degree (e) Load rotation angle of 6 degree (f) Load rotation angle of 10 degree

Figure 6-15: The camera view of GelSight sensor and the motion vectors of the markers under different rotating load.

vector fields only show the influence of the rotating load. The arrows are scaled according to the displacement magnitude.

From the figure, we can see that the displacement field is in a pattern of spinning around a rotating center. The spinning displacement within the contact area is much larger than that off the contact area. That is because the friction between the indenter and the elastomer make it tend to move with the indenter. And as the rotation load increases, at the beginning the overall magnitude of the elastomer displacement increases, and the displacement direction remains; then as the load is saturated the displacement field does not change much.

The magnitude distribution of the displacement field is shown in Figure 6-16. Figure 6-16(a) shows the case when the load is small, that the magnitude field is in circular distribution, and increases along the radius within the contact area; as the load increases, the magnitude distribution begins to deviate, and more concentrated to the area on the rotating direction. Or in other words, the differences between displacement magnitude in the concentrated area and in the non-concentrated area

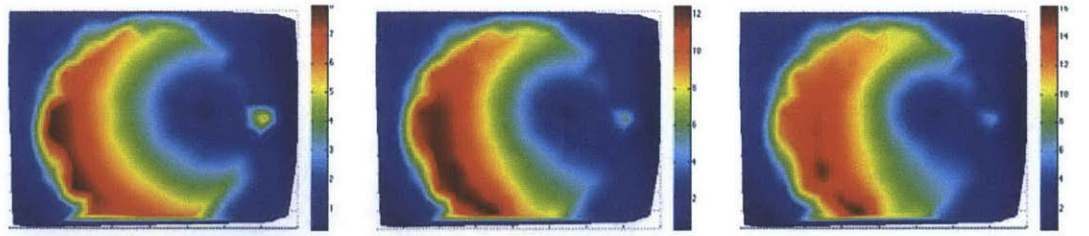

(a) Load rotation angle of 1 degree (b) Load rotation angle of 2 degree (c) Load rotation angle of 3 degree

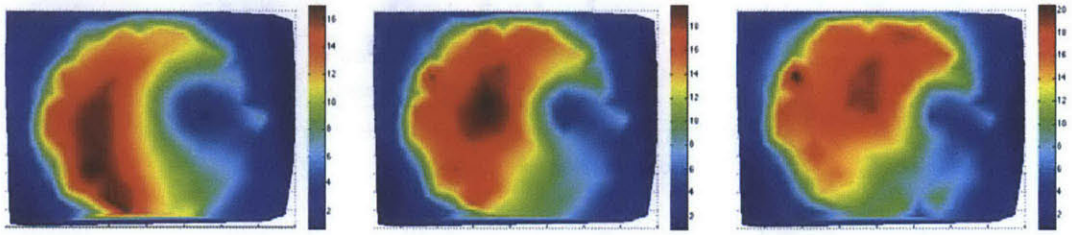

(d) Load rotation angle of 4 degree (e) Load rotation angle of 6 degree (f) Load rotation angle of 10 degree

Figure 6-16: The displacement magnitude map under different rotating load.

became larger and larger. Actually, this is an indication of the likeliness to slip.

From another point of view, the global torque of the contact surface can be considered as the reaction torque of the distributed shear force within the whole contact area, and the torque along the normal axis is resulted from the distribution of the shear force in a circular way. In this case, the shear and slip of the contact can be seen for the local areas separately. For this particular loading mode, when the load is large, partial slip happens in the contact area and is mostly in the part adverse to the rotation direction.

The relation between the marker displacement magnitude and the load rotation angle is shown in Figure 6-17. Two displacement changing trends are shown: the sum displacement of the whole camera view (that the displacement in the contact area makes the major contribution), and the displacement of the exact one marker that moves the most in all cases. The figure shows that for the marker that is within the displacement concentrated area, the displacement is to a linear relationship to the load angle except for the last case, where the slip is severe; but for the sum displacement, the linear relation ended very early and the deviation from the linear line is larger and larger as the load increases.

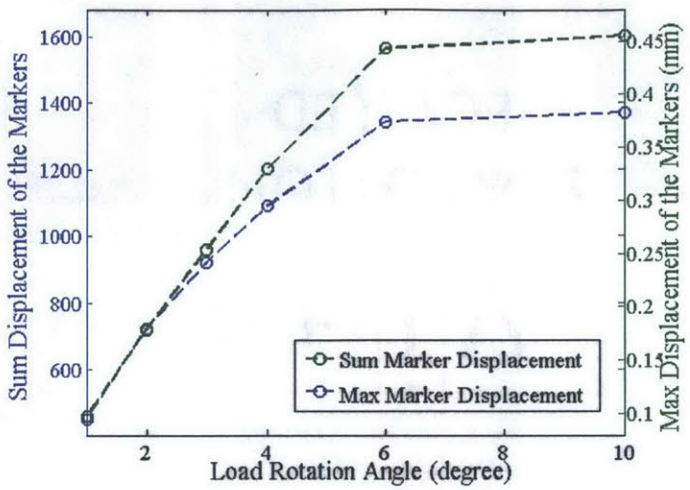

Figure 6-17: The sum marker displacement and maximum displacement under different loading angle.

6.3 Dynamic Grasping Experiments with the Portable GelSight

In this section, I use the portable GelSight device for some common manipulation job, and observe the response of the markers on the elastomer to the different manipulation procedure. The procedure being studied here is grasping and holding an object, which is a most common job for both human hand and robot hand. To make the procedure easy to control, I designed and built a mechanical jig that can adjust manually to achieve the grasping job.

6.3.1 Experimental Setup

The experimental setup used for this section is shown in Figure 6-18. The structure consists of a fixed bracing frame and movable crossbeam. The crossbeam can move in vertical direction along a graded rail that is fixed on the bracing frame, and there is a knob enabling the manipulator to move the crossbeam manually. There are two frames on the crossbeam to grasp and hold the object: on one side, the portable GelSight sensor is fixed on one of the frames, and the ATI nano17 force/torque sensor is fixed on the other side. A sponge is placed between the force/torque sensor side

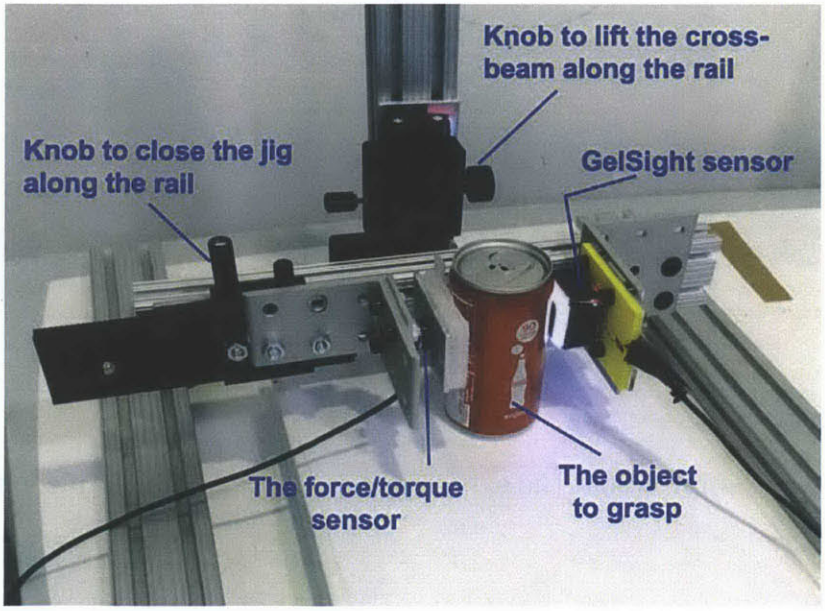

Figure 6-18: An overview of the experimental jig that can grasp and lift an object with both GelSight sensor and a ATI Nano17 force/torque sensor.

and the object to make a soft touch. The frame of the force/torque sensor side can move along a horizontal rail on the crossbeam, and there is also a knob on the rail that enabling controlling the movement on the rail manually.

So the two frames on the cross frame serve as a gripper to grasp an item. The GelSight sensor can feel about the contact surface and the onboard elastomer's deformation, and the force/torque sensor records the force and torque about the contact. As the object is only in contact with the two frames in the air, the normal force on the GelSight is the same to that of the force/torque sensor, and the shear forces of the two sides are equal. So the contact force and torque of the GelSight can be deducted from the force/torque sensor.

The adjustable rail on the crossbeam controls the distance between the two frames, in order to grasp the object tightly. The rail on the fixed bracing frame control the vertical movement of the crossbeam, including the grasped object. Figure 6-19 shows an example of the jig gripping and lifting a coke can, and some external force is going to be exerted on the can by the screwdriver.

In the experiment, an object, like a can, a tube, or a screw driver is grasped and lifted by the jig, and some external forces are applied. The data from GelSight

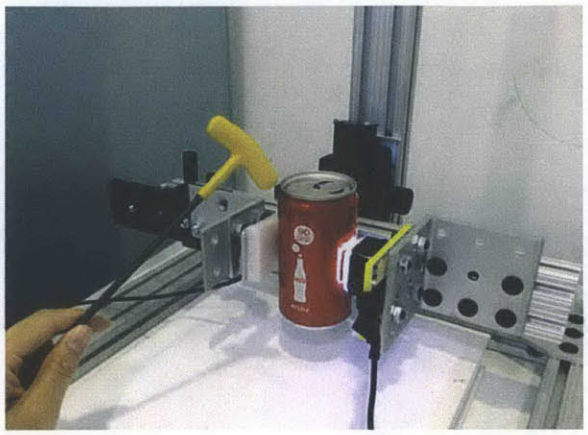

Figure 6-19: An example about the experiment jig holding a can while external forces being exerted.

sensor, the force/torque sensor, and the images from an external camera about the experiment scene are recorded.

6.3.2 An Experiment for Lifting a Can

In this part, an experiment of lifting a coke can with the jig is conducted, and the GelSight sensor's response to some normal grasping processes is studied. The processes include: grasping the can on the table, lifting the can, when the can is disturbed by some external forces during holding, and then the can slipped from the jig.

The object in this experiment is a 222mL coke can in cylinder shape, with the diameter of 57.2mm. The can is half filled, and the total weight is 100g. Different from the previous experiments, where the quasistatic response is studied, and I waited a period of time before recording the results, in this experiment the operation is in natural speed, and the contact condition changes very fast according to the real case. So the response is not quasistatic. The average frame rate of the GelSight camera is around 25Hz, and the average sampling rate of the force/torque sensor is 20Hz.

The first experiment process is holding the can from a free state, then lifting it from the table slowly, stopping for a while and putting it down on the table, then lifting it again. The process is repeated, and finally the can slipped down from the jig as the grasping frames loose in the air. Figure 6-20(b) shows the force change

during the process. Force Z is in the normal direction of both GelSight sensor plane and the force/torque sensor plane, and it corresponds to the squeezing force during the gripping. Force Y is the tangential force in the vertical direction, which balances the gravity and other vertical acceleration of the object.

Figure 6-20(b) shows the whole process: at the beginning, the object is on the table and free from the jig, so both Force Z and Force Y are zero; then the jig gripped the can, so Force Z quickly went to a high value and remained until the end of the process, when the jig loose and the can slipped down. Force Y is 0 at the beginning and in the end, and there are three periods that Force Y stayed in a positive value and remained for a while, those are when the can is lifted or held in the air. Because the lifting is very slow so the acceleration of the can is neglected, except for the moment when it left the table or when it declined to the table from the air, so most of the time in the air, the Force Y balances only the gravity and thus remains steady. And there is some large fluctuation between the stable periods, which corresponds to the large acceleration of the can when its motion state suddenly changed.

Figure 6-20 shows the response of GelSight at the moment when the can is steadily held on the table. Figure 6-20(a) shows the scene of the external camera, and Figure 6-20(b) shows the record of the force/torque sensor, where the plot is the change of the squeezing force and vertical force in the whole process, and the red parts represent the past time. The contact force plot shows the jig has just grasped the object and the squeezing force increased to a steady point; and there is some fluctuation on the vertical force, but not in the steady positive periods, so that means the can is not lifted and there are small vertical forces.

Figure 6-20(c) shows the image got by GelSight camera. The image can be used to track the displacements of the markers, and reconstruct the 3D surface of the elastomer according to the change of the local brightness. The border line of the contact area could be seen, but as the curvature of the can is too large, and the surface is very smooth, little details about the contact surface's geometry information can be seen. Figure 6-20(d) shows the displacement field of the current state. The background of the figure is the difference of the current GelSight image from the

(a) Scene from the external camera

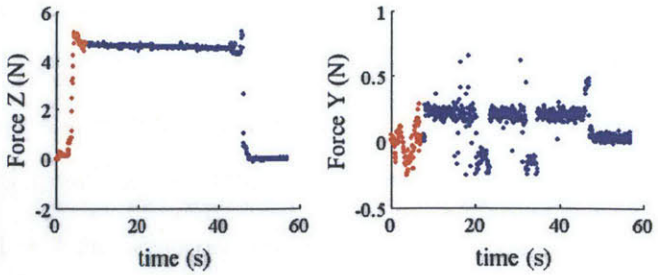

(b) Record of the force/torque sensor: the red data is the past time

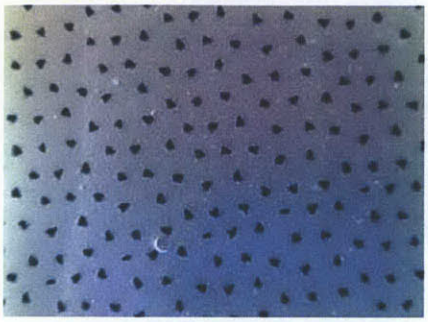

(c) View from GelSight camera

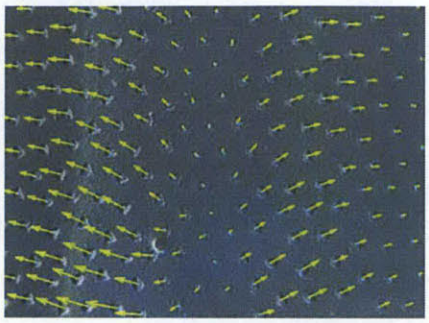

(d) Displacement field of the elastomer on the difference image

Figure 6-20: Experimental result in static gripping

original image when it touched nothing. The yellow vectors are the displacement of the markers from the original image, or the overall displacement of the elastomer; the cyan vector is the displacement of the markers from the last image frame, which can be considered as the displacement differential. The time between two frames is about 0.04s. The two vector fields are drawn in different scales just for a better display sake.

As shown in Figure 6-20, at the time of a steady grip the overall displacement of the elastomer surface is a trend of spreading out from the cylinder's height direction, which is resulted from the squeezing force about the jig. The displacement field's shape is very similar to the one of the indentation experiment with a cylinder indenter. However, the field is not ideally symmetric, that there is a trend that the displacement in the left half is larger than that in the right half, and the displacement is moving upwards in whole. This is resulted from the shear force during the contact. Actually for most of the contact cases, there is some unexpected shear load during the contact surface when we think we are "simply pressing". This is the case for both human

(a) Scene from the external camera

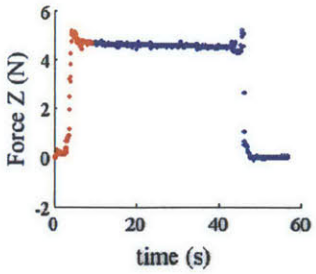

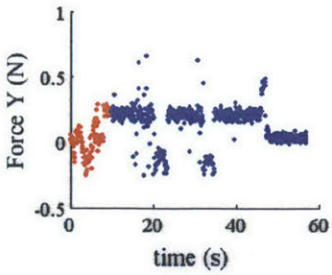

(b) Record of the force/torque sensor: the red data is the past time

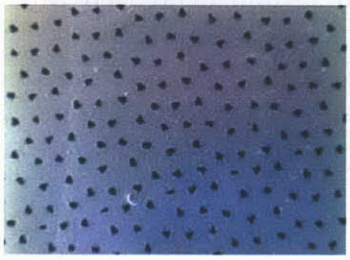

(c) View from GelSight camera

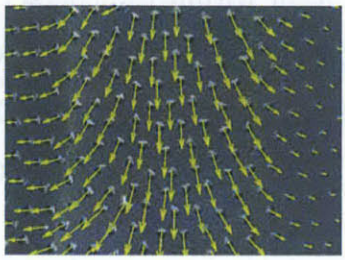

(d) Displacement field of the elastomer on the difference image

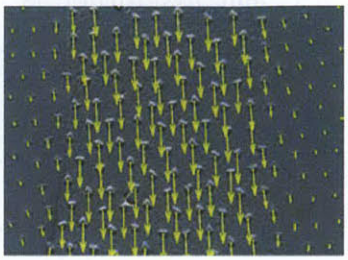

(e) Displacement field of the elastomer from simply grasping

Figure 6-21: Experimental result in static lifting

finger and GelSight sensor when it contacts a surface, as they are both soft tissues and perfect perpendicular contact is very hard to achieve. Figure 6-20(b) also shows some shear influence before the lifting. However the squeezing force in this case is always the predominant load, and influence the most for the displacement field.

Figure 6-20(d) also shows that the differential displacement field is very small in this moment, which means the currently the elastomer is very steady.

Figure 6-21 shows the case when the jig lifts the can slowly. The velocity is low, so the object's acceleration can be neglected. Figure 6-21(b) shows the force state: Force Z is in the steady state, that the squeezing force on the object remains, and Force Y is also in the steady area. Similar to the previous figure, Figure 6-21(c) shows the image get from the GelSight camera, and Figure 6-21(d) shows the displacement field of the current elastomer surface, with yellow arrows represent the sum displacement of the markers, and cyan arrows represent the difference in displacement of the markers. Figure 6-21(e) shows the displacement field of the current elastomer (as shown in Figure 6-21(c)) and the elastomer state when there is only pressing but small shear,

as shown in Figure 6-20(c).

The vector fields show that, the overall displacement field can be considered as the superposition of a pressing displacement field, which corresponds to the jig grasping the can without lifting, and a shear displacement field. Figure 6-21(e) shows the shear displacement field, that the marker motions are mostly in the shear direction (in this case is the vertical direction, to balance the gravity of the can), and the displacement magnitude is uniform within the contact area, and decreased rapidly out of the contact area. According to the theory introduced in Section 6.2.2, this indicates that the grasp is very safe and little partial slip happened between the contact surface. Figure 6-21(d) also shows that the differential of the displacement field is very small, and the field remained quite steady during the entire period when the can is in the air, as far as there is no external disturbance.

Figure 6-22 shows the moment when the can is lifted from the table. The moment is very short but large difference in the elastomer's surface was made, and the acceleration is large. Figure 6-22(c) to Figure 6-22(h) show the displacement filed of six consecutive frame got by the GelSight camera, and the time between the adjacent frames is about 0.04s. The vector fields clearly showed the change in the displacement in this 0.2s period of time. The displacement differential is very large in this moment, and the general direction is downward, aligned with the final shear direction. But the fields show that the change happened gradually, although in very short time, and is not uniform along the whole contact area.

From Figure 6-22(e) and Figure 6-22(g), we can see that the bottom half part in the image started to shear first and ended earlier, and the upper half part of the contact area started later and ended later. The reason for this is that the contact pressure is not evenly distributed over the whole contact area, and the bottom part has a little larger normal pressure. This is indicated from the field shown in Figure 6-22(c), when the lift has not begun. We can see from the figure that although the overall displacement field is in a trend of spreading from the cylinder, the displacement in the bottom part is a little larger than that of the upper part.

Figure 6-23 shows the moment when the can slipped down form the jig. I con-

(a) Scene from the external camera

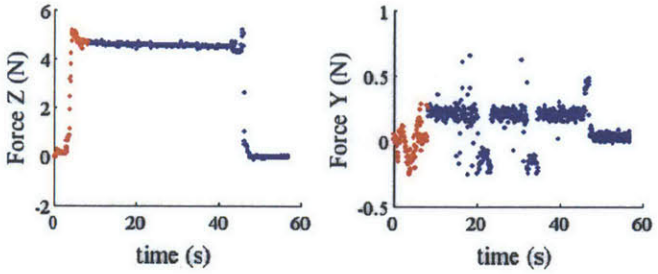

(b) Record of the force/torque sensor: the red data is the past time

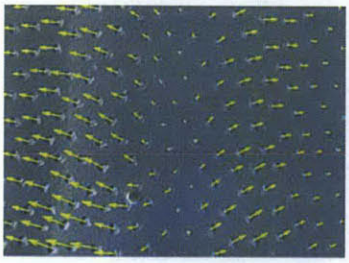

(c) Displacement on frame 1

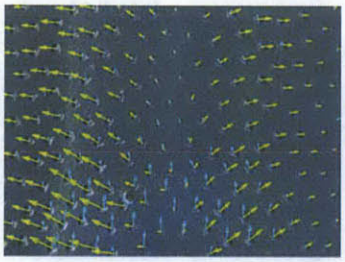

(d) Displacement on frame 2

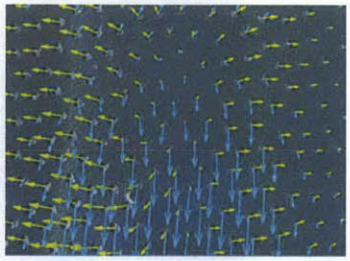

(e) Displacement on frame 3

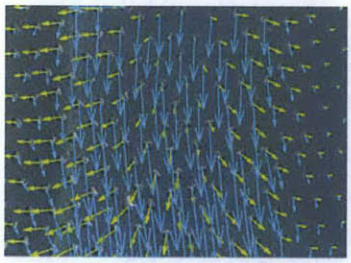

(f) Displacement on frame 4

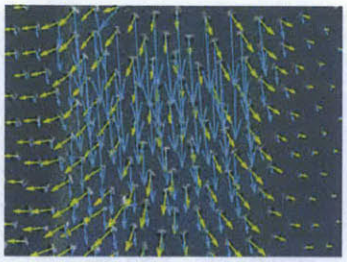

(g) Displacement on frame 5

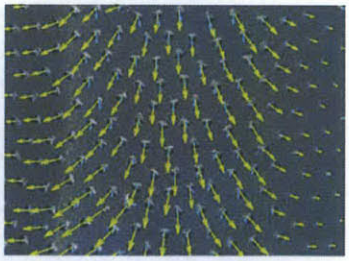

(h) Displacement on frame 6

Figure 6-22: Experimental result during the lifting moment

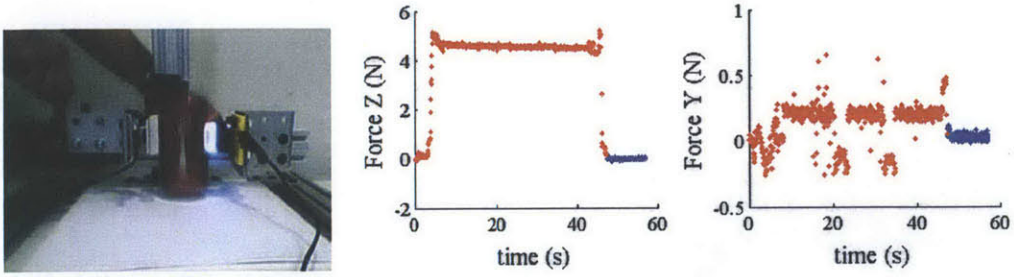

(a) Scene from the external camera

(b) Record of the force/torque sensor: the red data is the past time

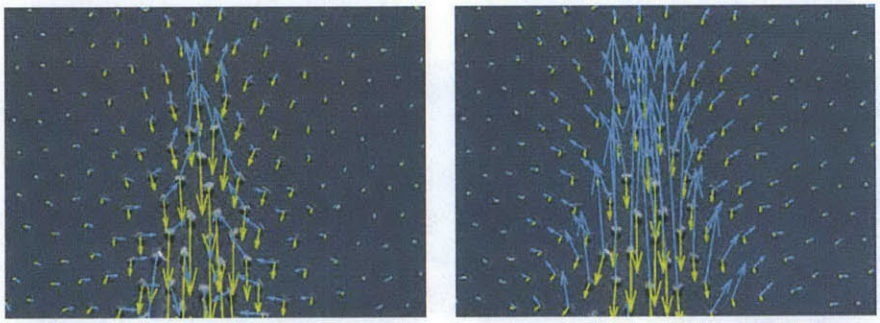

(c) Displacement field on frame 1

(d) Displacement field on frame 2

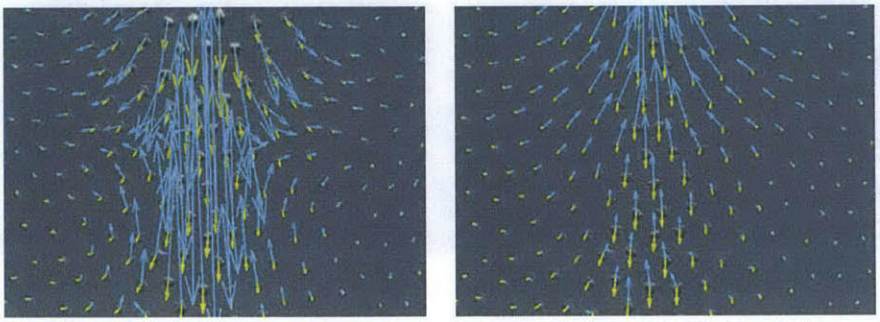

(e) Displacement field on frame 3

(f) Displacement field on frame 4

Figure 6-23: Experimental result during slipping

trolled the horizontal rail to release the frame holding the can slowly, and as the distance between the two frames increases, the squeezing force decreased rapidly, and the shear force limit also decreased until it could not balance the gravity. Then slip happened. Figure 6-23(c) to Figure 6-23(f) show the displacement fields of four consecutive frames of GelSight. The displacement field changes rapidly during the period, and the contact area decreased rapidly. This can be inferred from the area where the marker displacement is large enough.

In another experiment about lifting the can, I tested GelSight's response to external force and torque. Figure 6-24 shows the result. After the can was lifted steadily by the jig, I swang the can back and forth on the top part, as shown in Figure 6-24(a), to exert a torque in Z direction. Then I also exerted other disturbances like swinging the can up and down. Figure 6-24(b) and Figure 6-24(d) show the force record along the whole experiment period.

In this part, the process of the external torque along Z axis is studied. Figure 6-24(e) to Figure 6-24(j) show the displacement field of the different time periods during the disturbance. The overall displacement is large, and changed rapidly. To make the display more explicit, I scaled down the length of the arrows into about half of the that shown in the previous part of this section. The figures show that the elastomer is very sensitive to the external disturbance, and the response delay little. During the swinging, the elastomer displacement is generally in a rotating pattern around a rotation center.

6.4 Conclusion

In this chapter, two different experiments with the portable GelSight device are introduced. The portable GelSight is in small size, and has a potential for wide use. But the instrumental error of the device is larger, and the contact area mostly covers a large portion of the camera view, so the elastomer surface displacement mainly reflects the contact area.

One experiment is the indentation experiment in strictly controlled condition, and

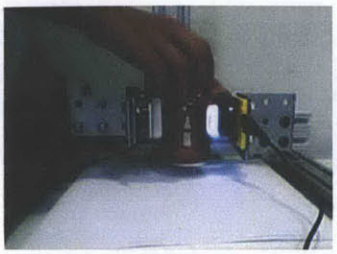

(a) Scene from the external camera

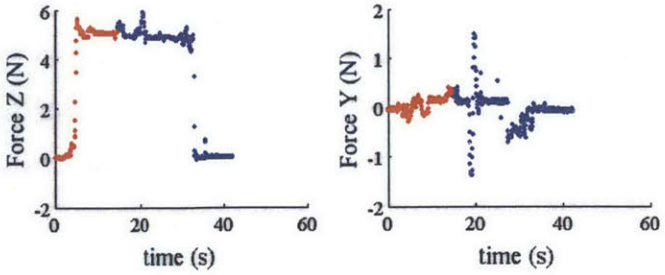

(b) Record of the force/torque sensor: the red data is the past time

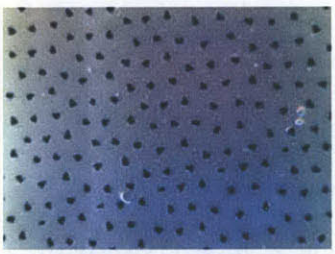

(c) Sight of the GelSight camera

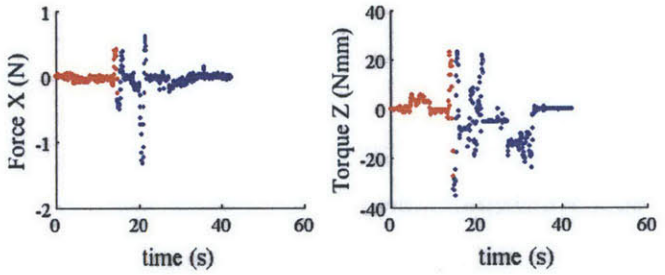

(d) Record of the force/torque sensor: the red data is the past time

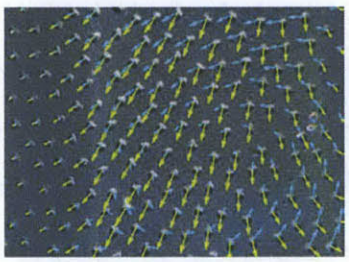

(e) Displacement field at the beginning of the disturb

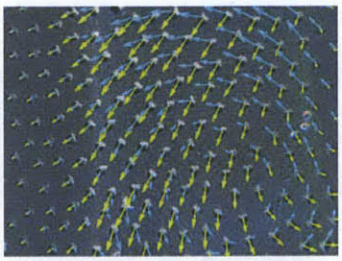

(f) Displacement field on 0.08s

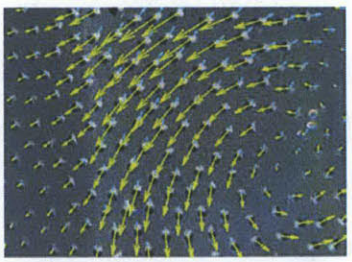

(g) Displacement field on 0.36s

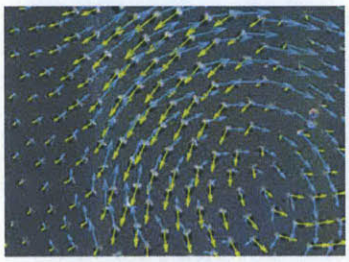

(h) Displacement field on 0.76s

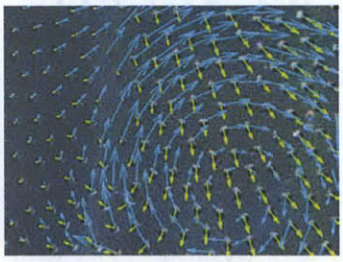

(i) Displacement field on 0.92s

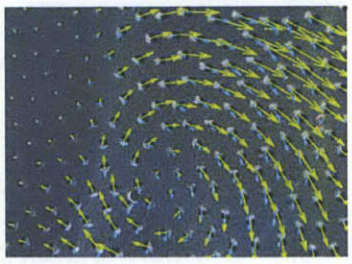

(j) Displacement field on 1.12s

Figure 6-24: Experimental result during the external disturbance

three different indenting situations are studied: normal indentation, shear indentation, and rotation indentation along the vertical axis. The indentation experiment works on the quasistatic response of the elastomer. The section described the elastomer's surface displacement field in response to different indenting modes, and proved that the linearity also exists between the force and the displacement in a large range, but the instrumental error is larger. The section also described the elastomer's response to larger local shear and incipient slip situation. However, further study about more general cases and building the quantitive explanation is still in need.

Another experiment is using the GelSight on a jig and doing a simple grasping job with a cylinder can. The experiment simulated the natural grasp process for either human hand or a robot gripper. The dynamic displacement field for different manipulation processes are recorded and described, and the displacement fields for some special moments are studied as the example. The section described the displacement field and its qualitative characters, and showed GelSight is very sensitive in detecting the interacting condition with the object. But further quantized study about the case is still needed.

Chapter 7

Conclusion and Future Work

The GelSight sensor is a new kind of tactile sensor that makes it possible to detect the high-resolution geometry of a contact surface. In this thesis, I proposed a method to measure the contact force with the GelSight sensor according to the mechanical properties of the elastomer. The method involves adding markers on the elastomer's surface and tracking the movement of the markers, to infer the planar deformation of the elastomer, and the deformation field is related to the distribution of the contact force. This thesis aims to find the relation between the deformation field and the contact load. Here are the accomplishments covered in the thesis:

1. Proposed a method to measure the contact force with GelSight. Designed and fabricated the elastomer needed for the prototype.

2. Described and tested the material properties of the elastomer.

3. Built the elastomer's finite-element model in ADINA, described the ideal displacement field under different load conditions, and analyzed the influence of the elastomer's geometry on the displacement field.

4. Designed and built the experimental setup for normal, shear, and rotating load on the GelSight prototypes, with the load displacement controlled and load force and torques measured.

5. Conducted the experiments of normal and shear load on the box setting GelSight. Different indenters were applied. The quasistatic responses of the elastomer's surface displacement fields were recorded and analyzed. Built the numerical relation between the displacement field and the indentation load based on the comparison of the experimental field and the simulated field. Described the characteristics for slip and incipient slip.

6. Conducted the indentation experiments with a circular flat-end indenter on the portable GelSight prototype. Described the elastomer's quasistatic response for the normal, shear, and rotation load.

The current results show that tracking the surface displacement of the elastomer is a very effective way to learn about the contact condition of the sensor and the contact surface, and can provide a great deal of information about manipulation. Though difficult, GelSight shows its potential to measure contact forces, especially the temporal change of the force. However, more work is required to improve its performance. Listed below are the next steps necessary to enhance the theory and boost GelSights ability to measure contact force:

1. Conducting indentation experiment and simulation of more general conditions, such as more indenter shapes and unbalanced loading.

2. Building a universal model for the relation of indenting load and the GelSight displacement field, for more general loading conditions.

3. Analyzing in detail the displacement field for a grasping job.

4. Conducting more experiments using GelSight in some common grasping and manipulation jobs, and considering different operating situations. Generalizing the relation of the displacement fields and the object manipulation.

Bibliography

[1] Ati nano17 profiles. http://www.ati-ia.com/products/ft/ft_models.aspx?id=Nano17.

[2] On line demo of robotouch. http://www.pressureprofile.com/products-robotouch.

[3] Product introduction of biotac sensor. http://www.syntouchllc.com/Products/BioTac/.

[4] Tactile pressure sensor products of pressure profile systems inc. http://www.pressureprofile.com/products.php.

[5] Lallit Anand. Mechanics of solid materials. University Lecture Notes, 2013.

[6] Simon Baker and Iain Matthews. Lucas-kanade 20 years on: A unifying framework. *International journal of computer vision*, 56(3):221–255, 2004.

[7] Antonio Bicchi and Vijay Kumar. Robotic grasping and contact: A review. In *ICRA*, pages 348–353. Citeseer, 2000.

[8] Ravinder S Dahiya, Giorgio Metta, Maurizio Valle, and Giulio Sandini. Tactile sensingfrom humans to humanoids. *Robotics, IEEE Transactions on*, 26(1):1–20, 2010.

[9] N. J. Ferrier. Reconstructing the shape of a deformable membrane from image data. *The International Journal of Robotics Research*, 19(9):795–816, September 2000.

[10] Jeremy A Fishel, Veronica J Santos, and Gerald E Loeb. A robust micro-vibration sensor for biomimetic fingertips. In *Biomedical Robotics and Biomechatronics, 2008. BioRob 2008. 2nd IEEE RAS & EMBS International Conference on*, pages 659–663. IEEE, 2008.

[11] Robert D Howe. Tactile sensing and control of robotic manipulation. *Advanced Robotics*, 8(3):245–261, 1993.

[12] D. Hristu, N. Ferrier, and R.W. Brockett. The performance of a deformable-membrane tactile sensor: basic results on geometrically-defined tasks. volume 1, pages 508–513. IEEE, 2010.

[13] Eun-Soo Hwang, Jung-hoon Seo, and Yong-Jun Kim. A polymer-based flexible tactile sensor for both normal and shear load detections and its application for robotics. *Microelectromechanical Systems, Journal of*, 16(3):556–563, 2007.

[14] Yuji Ito, Youngwoo Kim, and Goro Obinata. Robust slippage degree estimation based on reference update of vision-based tactile sensor. *Sensors Journal, IEEE*, 11(9):2037–2047, 2011.

[15] Xiaodan Jia, Rui Li, M. A. Srinivasan, and E. H. Adelson. Lump detection with a gelsight sensor. pages 175–179. IEEE, April 2013.

[16] Xiaodan (Stella) Jia. *Tactile sensing using elastomeric sensors.* Thesis (S.M.), Massachusetts Institute of Technology, 2012.

[17] Micah K. Johnson, Forrester Cole, Alvin Raj, and Edward H. Adelson. Microgeometry capture using an elastomeric sensor. page 1. ACM Press, 2011.

[18] M.K. Johnson and E.H. Adelson. Retrographic sensing for the measurement of surface texture and shape. pages 1070–1077. IEEE, June 2009.

[19] K. Kamiyama, K. Vlack, T. Mizota, H. Kajimoto, K. Kawakami, and S. Tachi. Vision-based sensor for real-time measuring of surface traction fields. *IEEE Computer Graphics and Applications*, 25(1):68–75, January 2005.

[20] Rui Li, Robert Platt Jr, Wenzhen Yuan, Andreas ten Pas, Nathan Roscup, Mandayam A Srinivasan, and Edward H Adelson. Localization and manipulation of small parts using gelsight tactile sensing. 2014.

[21] Chia Hsien Lin, Todd W Erickson, Jeremy A Fishel, Nicholas Wettels, and Gerald E Loeb. Signal processing and fabrication of a biomimetic tactile sensor array with thermal, force and microvibration modalities. In *Robotics and Biomimetics (ROBIO), 2009 IEEE International Conference on*, pages 129–134. IEEE, 2009.

[22] Bruce D Lucas, Takeo Kanade, et al. An iterative image registration technique with an application to stereo vision. In *IJCAI*, volume 81, pages 674–679, 1981.

[23] Goro Obinata, T Kurashima, and N Moriyama. Vision-based tactile sensor using transparent elastic fingertip for dexterous handling. In *INTERNATIONAL SYMPOSIUM ON ROBOTICS*, volume 36, page 32. unknown, 2005.

[24] Ruben D Ponce Wong, Jonathan D Posner, and Veronica J Santos. Flexible microfluidic normal force sensor skin for tactile feedback. *Sensors and Actuators A: Physical*, 179:62–69, 2012.

[25] Jonathan Rossiter and T Mukai. An led-based tactile sensor for multi-sensing over large areas. In *Sensors, 2006. 5th IEEE Conference on*, pages 835–838. IEEE, 2006.

[26] Jonathan Rossiter and Toshiharu Mukai. A novel tactile sensor using a matrix of leds operating in both photoemitter and photodetector modes. In *Sensors, 2005 IEEE*, pages 4–pp. IEEE, 2005.

[27] K. Sato, K. Kamiyama, N. Kawakami, and S. Tachi. Finger-shaped GelForce: sensor for measuring surface traction fields for robotic hand. *IEEE Transactions on Haptics*, 3(1):37–47, January 2010.

[28] John L Schneiter and Thomas B Sheridan. An optical tactile sensor for manipulators. *Robotics and computer-integrated manufacturing*, 1(1):65–71, 1984.

[29] Oliver A. Shergold, Norman A. Fleck, and Darren Radford. The uniaxial stress versus strain response of pig skin and silicone rubber at low and high strain rates. *International Journal of Impact Engineering*, 32(9):1384–1402, September 2006.

[30] Nicholas Wettels and Gerald E Loeb. Haptic feature extraction from a biomimetic tactile sensor: force, contact location and curvature. In *Robotics and Biomimetics (ROBIO), 2011 IEEE International Conference on*, pages 2471–2478. IEEE, 2011.

[31] Robert J. Woodham. Photometric method for determining surface orientation from multiple images. *Optical Engineering*, 19(1):191139, February 1980.

[32] Hanna Yousef, Mehdi Boukallel, and Kaspar Althoefer. Tactile sensing for dexterous in-hand manipulation in roboticsa review. *Sensors and Actuators A: physical*, 167(2):171–187, 2011.